EUROPEAN ORGANISATION FOR NUCLEAR RESEARCH (CERN)

arXiv:1406.7844v1 [hep-ex] 30 Jun 2014

Comprehensive measurements of *t*-channel single top-quark production cross sections at $\sqrt{s} = 7$ TeV with the ATLAS detector

The ATLAS Collaboration

Abstract

This article presents measurements of the t-channel single top-quark (t) and top-antiquark ($\bar{t}$) total production cross sections $\sigma(tq)$ and $\sigma(\bar{t}q)$, their ratio $R_t = \sigma(tq)/\sigma(\bar{t}q)$, and a measurement of the inclusive production cross section $\sigma(tq + \bar{t}q)$ in proton–proton collisions at $\sqrt{s} = 7$ TeV at the LHC. Differential cross sections for the tq and $\bar{t}q$ processes are measured as a function of the transverse momentum and the absolute value of the rapidity of t and $\bar{t}$, respectively. The analyzed data set was recorded with the ATLAS detector and corresponds to an integrated luminosity of 4.59 fb^{-1}. Selected events contain one charged lepton, large missing transverse momentum, and two or three jets. The cross sections are measured by performing a binned maximum-likelihood fit to the output distributions of neural networks. The resulting measurements are $\sigma(tq) = 46 \pm 6$ pb, $\sigma(\bar{t}q) = 23 \pm 4$ pb, $R_t = 2.04 \pm 0.18$, and $\sigma(tq + \bar{t}q) = 68 \pm 8$ pb, consistent with the Standard Model expectation. The uncertainty on the measured cross sections is dominated by systematic uncertainties, while the uncertainty on R_t is mainly statistical. Using the ratio of $\sigma(tq + \bar{t}q)$ to its theoretical prediction, and assuming that the top-quark-related CKM matrix elements obey the relation $|V_{tb}| \gg |V_{ts}|, |V_{td}|$, we determine $|V_{tb}| = 1.02 \pm 0.07$.

Comprehensive measurements of t-channel single top-quark production cross sections at $\sqrt{s} = 7$ TeV with the ATLAS detector

The ATLAS collaboration

(Dated: July 1, 2014)

This article presents measurements of the t-channel single top-quark (t) and top-antiquark ($\bar{t}$) total production cross sections $\sigma(tq)$ and $\sigma(\bar{t}q)$, their ratio $R_t = \sigma(tq)/\sigma(\bar{t}q)$, and a measurement of the inclusive production cross section $\sigma(tq + \bar{t}q)$ in proton–proton collisions at $\sqrt{s} = 7$ TeV at the LHC. Differential cross sections for the tq and $\bar{t}q$ processes are measured as a function of the transverse momentum and the absolute value of the rapidity of t and $\bar{t}$, respectively. The analyzed data set was recorded with the ATLAS detector and corresponds to an integrated luminosity of 4.59 fb^{-1}. Selected events contain one charged lepton, large missing transverse momentum, and two or three jets. The cross sections are measured by performing a binned maximum-likelihood fit to the output distributions of neural networks. The resulting measurements are $\sigma(tq) = 46 \pm 6$ pb, $\sigma(\bar{t}q) = 23 \pm 4$ pb, $R_t = 2.04 \pm 0.18$, and $\sigma(tq + \bar{t}q) = 68 \pm 8$ pb, consistent with the Standard Model expectation. The uncertainty on the measured cross sections is dominated by systematic uncertainties, while the uncertainty on R_t is mainly statistical. Using the ratio of $\sigma(tq + \bar{t}q)$ to its theoretical prediction, and assuming that the top-quark-related CKM matrix elements obey the relation $|V_{tb}| \gg |V_{ts}|, |V_{td}|$, we determine $|V_{tb}| = 1.02 \pm 0.07$.

I. INTRODUCTION

In proton–proton (pp) collisions at the LHC, top quarks are produced at unprecedented rates, allowing studies that were intractable before. The production of single top quarks via weak charged-current interactions is among the top-quark phenomena becoming accessible to precise investigations. In leading-order (LO) perturbation theory, single top-quark production is described by three subprocesses that are distinguished by the virtuality of the exchanged W boson. The dominant process is the t-channel exchange depicted in Fig. 1, which is the focus of the measurements presented in this article. A light quark from one of the colliding protons interacts with a b-quark from another proton by exchanging a virtual W boson (W^*). Since the u-quark density of the proton is about twice as high as the d-quark density, the production cross section of single top quarks $\sigma(tq)$, shown in Fig. 1(a), is expected to be about twice as high as the cross section of top-antiquark production $\sigma(\bar{t}q)$, shown in Fig. 1(b). At LO, subleading sin-
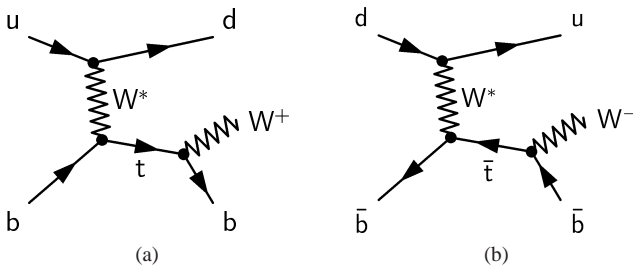

FIG. 1. Representative leading-order Feynman diagrams of (a) single top-quark production and (b) single top-antiquark production via the t-channel exchange of a virtual W^* boson.

gle top-quark processes are the associated production of a W boson and a top quark (Wt) and the s-channel production of $t\bar{b}$, analogous to the Drell–Yan process.

In general, measurements of single top-quark production

provide insights into the properties of the Wtb vertex. The cross sections are proportional to the square of the coupling at the production vertex. In the Standard Model (SM), the coupling is given by the Cabibbo–Kobayashi–Maskawa (CKM) matrix element V_{tb} [1, 2] multiplied by the universal electroweak coupling constant. Angular distributions of top-quark decay products give access to the Lorentz structure of the Wtb vertex, which has a vector–axial vector structure in the SM. As illustrated in Fig. 1, the t-channel process features a b-quark in the initial state if described in LO Quantum Chromodynamics (QCD), and therefore the cross section depends strongly on the b-quark parton distribution function (PDF), which is derived from the gluon PDF by means of the DGLAP evolution [3–5]. A measurement of the combined top-quark and top-antiquark cross section $\sigma(tq + \bar{t}q) = \sigma(tq) + \sigma(\bar{t}q)$ is well suited to constrain V_{tb} or the b-quark PDF. In addition, the measurement of $\sigma(tq + \bar{t}q)$ is sensitive to various models of new physics phenomena [6], such as extra heavy quarks, gauge bosons, or scalar bosons.

Separate measurements of $\sigma(tq)$ and $\sigma(\bar{t}q)$ extend the sensitivity to the PDFs of the u-quark and the d-quark, exploiting the different initial states of the two processes, shown in Fig. 1. At a center-of-mass energy of $\sqrt{s} = 7$ TeV, the typical momentum fraction x of the initial-state light quarks is in the range of $0.02 \lesssim x \lesssim 0.5$, with a median of 0.17 for u-quarks and a median of 0.13 for d-quarks. The additional measurement of the cross-section ratio $R_t \equiv \sigma(tq)/\sigma(\bar{t}q)$ is sensitive to the ratio of the two PDFs in the x-range specified above and features smaller systematic uncertainties because of partial cancelations of common uncertainties. The measurements of $\sigma(tq)$, $\sigma(\bar{t}q)$, and R_t provide complementary inputs in constraining PDFs to data currently used in QCD fits. Investigating R_t also provides a way of searching for new-physics contributions in single top-quark (top-antiquark) production [7] and of elucidating the nature of physics beyond the SM if it were to be observed [8].

In this article we present measurements of $\sigma(tq + \bar{t}q)$, $\sigma(tq)$, $\sigma(\bar{t}q)$, and the cross-section ratio R_t at a center-of-mass

energy of $\sqrt{s} = 7$ TeV, using the full data set corresponding to an integrated luminosity of 4.59 fb^{-1}. Final calibrations for the 7 TeV data set are used, resulting in reduced systematic uncertainties. The measurement of $\sigma(tq + \bar{t}q)$ is used to determine the value of the CKM matrix element $|V_{tb}|$. Additionally, for the first time, differential cross sections are measured as a function of the transverse momentum of the top quark, $p_T(t)$, and the top antiquark, $p_T(\bar{t})$, and as a function of the absolute value of the rapidities $|y(t)|$ and $|y(\bar{t})|$, respectively.

In pp collisions at $\sqrt{s} = 7$ TeV, the total inclusive cross sections of top-quark and top-antiquark production in the t-channel are predicted to be

$$\sigma(tq) = 41.9^{+1.8}_{-0.9} \text{ pb},$$
$$\sigma(\bar{t}q) = 22.7^{+0.9}_{-1.0} \text{ pb, and}$$
$$\sigma(tq + \bar{t}q) = 64.6^{+2.7}_{-2.0} \text{ pb},$$

with approximate next-to-next-to-leading-order (NNLO) precision [9], assuming a top-quark mass of $m_t = 172.5$ GeV and using the MSTW2008 NNLO [10] PDF set. The quoted uncertainty contains the scale uncertainty and the correlated PDF–α_s uncertainty. The contributions due to the resummation of soft-gluon bremsstrahlung included in the approximate NNLO result are relatively small and the cross-section predictions are therefore very close to the plain next-to-leading-order (NLO) calculation [11]. All predictions used in this article are based on the "five-flavor scheme", involving a b-quark in the initial state (see Fig. 1). An alternative approach is to consider the Born process $qg \rightarrow tqb$, where the b-quark does not enter in the QCD evolution of the PDFs and the strong coupling constant, referred to as "four-flavor scheme". Recently, computations of differential cross sections have become available at approximate NNLO precision [12], complementing the predictions at NLO [11]. Measurements of these differential quantities will allow more stringent tests of the calculations. In addition, a thorough study of differential cross sections can give hints about the potential presence of flavor-changing neutral currents or four-fermion operators in the single top-quark production process [13].

Single top-quark production in the t-channel was first established in $p\bar{p}$ collisions at $\sqrt{s} = 1.96$ TeV at the Tevatron [14]. Measurements of t-channel single top-quark and Wt production at the LHC at $\sqrt{s} = 7$ TeV were performed by the ATLAS collaboration [15, 16] and the CMS collaboration [17, 18]. The ATLAS measurements used only a fraction of the recorded data, corresponding to 1.04 fb^{-1} in the t-channel analysis. At $\sqrt{s} = 8$ TeV the CMS collaboration measured the t-channel cross sections and the cross-section ratio R_t [19].

The measurements presented in this article are based on events in the lepton+jets channel, in which the lepton can be either an electron or a muon originating from a W-boson decay. The analysis has acceptance for signal events involving $W \rightarrow \tau \nu$ decays if the τ lepton decays subsequently to either $e\nu_e\nu_\tau$ or $\mu\nu_\mu\nu_\tau$. The experimental signature of candidate events is thus given by one charged lepton (electron or muon), large values of the magnitude of the missing transverse momentum E_T^{miss}, and two or three hadronic jets with high transverse momentum. The acceptance for t-channel events is dominated by the 2-jet signature, where one jet is a b-quark jet, while the second jet is a light-quark jet. A significant fraction of single top-quark events are also present in the 3-jet channel, whereas the $t\bar{t}$ background is dominant in the 4-jet channel. For this reason, the analysis is restricted to events with two or three jets.

Several other processes feature the same signature as single top-quark events, the main backgrounds being W+jets production and top-quark-antiquark ($t\bar{t}$) pair production. Since a typical signature-based event selection yields only a relatively low signal purity, a dedicated analysis strategy is developed to separate signal and background events. In both the 2-jet and 3-jet channels, several observables discriminating between signal and background events are combined by a neural network (NN) to one discriminant (NN output). The cross-section measurements are based on a simultaneous fit to these multivariate discriminants. In the 2-jet channel, a cut on the NN discriminant is applied to obtain a sample of events enriched in t-channel single top-quark events, facilitating the measurement of differential cross sections.

II. DATA SAMPLES AND SAMPLES OF SIMULATED EVENTS

The analysis described in this article uses pp LHC collision data collected at a center-of-mass energy of 7 TeV with the ATLAS detector [20] between March and November 2011. In this data-taking period, the average number of pp collisions per bunch crossing was nine. The selected events were recorded based on single-electron or single-muon triggers. Stringent detector and data quality requirements are applied, resulting in a data set corresponding to an integrated luminosity of 4.59 ± 0.08 fb^{-1} [21].

A. The ATLAS detector

The ATLAS detector [20] is built from a set of cylindrical subdetectors, which cover almost the full solid angle around the interaction point [22]. ATLAS is composed of an inner tracking detector (ID) close to the interaction point, surrounded by a superconducting solenoid providing a 2 T axial magnetic field, electromagnetic and hadronic calorimeters, and a muon spectrometer (MS). The ID consists of a silicon pixel detector, a silicon microstrip detector (SCT), and a straw-tube transition radiation tracker (TRT). The electromagnetic calorimeter is a lead and liquid-argon (LAr) sampling calorimeter with high granularity. An iron/scintillator tile calorimeter provides hadronic energy measurements in the central pseudorapidity range. The endcap and forward regions are instrumented with LAr calorimeters for both the electromagnetic and hadronic energy measurements. The MS consists of three large superconducting toroids with eight coils each, a system of trigger chambers, and precision tracking chambers.

B. Trigger requirements

ATLAS employs a three-level trigger system. The first level (L1) is built from custom-made hardware, while the second and third levels are software based and collectively referred to as the High Level Trigger (HLT). The data sets used in this analysis are defined by high-p_T single electron or single muon triggers [23]. During the data-taking period slightly different trigger conditions were used to cope with the increasing number of multiple pp collisions per bunch crossing (pile-up).

At L1, electron candidate events are required to have an electromagnetic energy deposit of $E_T > 14$ GeV; in the second part of the data-taking period the requirement was $E_T > 16$ GeV. At the HLT level, the full granularity of the calorimeter and tracking information is available. The calorimeter cluster is matched to a track and the trigger electron object has to have $E_T > 20$ GeV or $E_T > 22$ GeV, exceeding the corresponding L1 requirements by 6 GeV.

The single muon trigger is based on muon candidates reconstructed in the muon spectrometer. At L1, a threshold of $p_T = 10$ GeV is applied. At the HLT level, the requirement is tightened to $p_T > 18$ GeV.

C. Simulated events

Samples of simulated t-channel single top-quark events are produced with the NLO matrix-element generator POWHEG-BOX [24] interfaced to PYTHIA [25] (version 6.4.27) for showering and hadronization. In POWHEG-BOX the four-flavor scheme calculation is used to simulate t-channel single top-quark production. The events are generated using the fixed four-flavor NLO PDF set CT104f [26] and the renormalization and factorization scales are calculated event-by-event [27] with $\mu_R = \mu_F = 4 \cdot \sqrt{m_b^2 + p_{T,b}^2}$, where m_b and $p_{T,b}$ are the mass and p_T of the b-quark from the initial gluon splitting.

Samples of $t\bar{t}$ events, Wt events, and s-channel single top-quark events are generated with POWHEG-BOX interfaced to PYTHIA using the CT10 NLO PDF set [26]. All processes involving top quarks are produced assuming $m_t = 172.5$ GeV, and the parameters of the PYTHIA generator controlling the modeling of the parton shower and the underlying event are set to the values of the Perugia 2011 tune [28].

Vector-boson production in association with jets (W/Z+jets) is simulated using the multileg LO generator ALPGEN [29] (version 2.13) using the CTEQ6L1 PDF set [30]. The partonic events are showered with HERWIG [31] (version 6.5.20), and the underlying event is simulated with the JIMMY [32] model (version 4.31) using values of the ATLAS Underlying Event Tune 2 [33]. W+jets and Z+jets events with up to five additional partons are generated. The MLM matching scheme [34] is used to remove overlap between partonic configurations generated by the matrix element and by parton shower evolution. The double counting between the inclusive $W + n$-parton samples and samples with associated heavy-quark pair-production

is removed utilizing an overlap removal based on a ΔR matching. The diboson processes WW, WZ and ZZ are generated using HERWIG and JIMMY.

After the event generation step, all samples are passed through the full simulation of the ATLAS detector [35] based on GEANT4 [36] and are then reconstructed using the same procedure as for collision data. The simulation includes the effect of multiple pp collisions per bunch crossing. The events are weighted such that the distribution of the number of collisions per bunch crossing is the same as in collision data.

III. PHYSICS OBJECT DEFINITIONS

In this section the definition of the physics objects is given, namely reconstructed electrons, muons, and jets, as well as E_T^{miss}. The definition of these objects involves the reconstructed position of the hard interaction. Primary interaction vertices are computed from reconstructed tracks that are compatible with coming from the luminous interaction region. The hard-scatter primary vertex is chosen as the vertex featuring the highest $\sum p_T^2$, the sum running over all tracks with $p_T > 0.4$ GeV associated with the vertex.

A. Electrons

Electron candidates are selected from energy deposits (clusters) in the LAr electromagnetic calorimeter matched to tracks [37] and are required to have $E_T > 25$ GeV and $|\eta_{cl}| < 2.47$, where η_{cl} denotes the pseudorapidity of the cluster. Clusters falling in the calorimeter barrel/endcap transition region, corresponding to $1.37 < |\eta_{cl}| < 1.52$, are ignored. The energy of an electron candidate is taken from the cluster, while its η and ϕ are taken from the track. The z-position of the track has to be compatible with the hard-scatter primary vertex. Electron candidates are further required to fulfill stringent criteria regarding calorimeter shower shape, track quality, track–cluster matching, and fraction of high-threshold hits in the TRT to ensure high identification quality.

Hadronic jets mimicking the signature of an electron, electrons from b-hadron or c-hadron decays, and photon conversions constitute the major backgrounds for high-p_T electrons originating from the decay of a W boson. Since signal electrons from W-boson decay are typically isolated from jet activity, these backgrounds can be suppressed via isolation criteria that require minimal calorimeter activity (calorimeter isolation) and only few tracks (track isolation) in an (η, ϕ) region around the electron. Electron candidates are isolated by imposing thresholds on the scalar sum of the transverse momenta of calorimeter energy deposits Σp_T^{calo} within a surrounding cone of radius $\Delta R = 0.2$, excluding the energy deposit associated with the candidate, and on the scalar sum of the transverse momenta of tracks $\Sigma p_T^{\text{track}}$ in a cone of radius $\Delta R = 0.3$ around the candidate excluding the track associated with the electron candidate. The Σp_T^{calo} variable is corrected for pile-up effects as a function of the number of reconstructed vertices. The thresholds applied to Σp_T^{calo} and $\Sigma p_T^{\text{track}}$ vary as

a function of the electron p_T, the electron η, and the number of reconstructed primary vertices and are chosen such that the efficiency for electrons from W-boson or Z-boson decays to pass this isolation requirement is 90%.

B. Muons

Muon candidates are reconstructed by combining track segments found in the ID and in the MS [38]. The momentum as measured using the ID is required to agree with the momentum measured using the MS after correcting for the predicted muon energy loss in the calorimeter. Only candidates that have $p_T > 25$ GeV and $|\eta| < 2.5$ are considered. Selected muons must additionally satisfy a series of requirements on the number of track hits present in the various tracking subdetectors. Muon tracks are required to have at least two hits in the pixel detector, and six or more hits in the SCT. Tracks are rejected if they have more than two missing hits in the SCT and pixel detectors, or tracks with an excessive number of outlier hits in the TRT. Isolated muon candidates are selected by requiring $\Sigma p_T^{\mathrm{calo}} < 4$ GeV within a surrounding cone of radius $\Delta R = 0.2$, and $\Sigma p_T^{\mathrm{track}} < 2.5$ GeV within a surrounding cone of radius $\Delta R = 0.3$. The efficiency of this combined isolation requirement varies between 95% and 97%, depending on the data-taking period.

The reconstruction, identification and trigger efficiencies of electrons and muons are measured using tag-and-probe methods on samples enriched with $Z \rightarrow \ell\ell$, $J/\psi \rightarrow \ell\ell$, or $W^{\pm} \rightarrow \ell\nu$ ($\ell = e, \mu$) events [37, 38].

C. Jets and missing transverse momentum

Jets are reconstructed using the anti-k_t algorithm [39] with a radius parameter of 0.4, using topological clusters [40] identified in the calorimeter as inputs to the jet clustering. The jet energy is corrected for the effect of multiple pp interactions, both in collision data and in simulated events. Further energy corrections apply factors depending on the jet energy and the jet η to achieve a calibration that matches the energy of stable particle jets in simulated events [41]. Differences between data and Monte Carlo simulation are evaluated using in situ techniques and are corrected for in an additional step [42]. The in situ calibration exploits the p_T balance in Z+jet, γ+jet, and dijet events. Z+jet and γ+jet data are used to set the jet energy scale (JES) in the central detector region, while p_T balancing in dijet events is used to achive an η intercalibration of jets in the forward region with respect to central jets.

Jets with separation $\Delta R < 0.2$ from selected electron candidates are removed, as in these cases the jet and the electron are very likely to correspond to the same physics object. In order to reject jets from pile-up events, a quantity called the jet-vertex fraction $\varepsilon_{\mathrm{jvf}}$ is defined as the ratio of $\sum p_T$ for all tracks within the jet that originate from the hard-scatter primary vertex to the $\sum p_T$ of all tracks matched to the jet. It is required that $\varepsilon_{\mathrm{jvf}} > 0.75$ for those jets that have associated tracks. The $\varepsilon_{\mathrm{jvf}}$ criterion is omitted for jets without matched

tracks. An overlap removal between jets and muons is applied, removing any muon with separation $\Delta R < 0.4$ from a jet with $p_T > 25$ GeV and $\varepsilon_{\mathrm{jvf}} > 0.75$. In the same way an overlap removal is applied between jets and electrons, removing any electron separated from a jet by $0.2 < \Delta R < 0.4$.

Only jets having $p_T > 30$ GeV and $|\eta| < 4.5$ are considered. Jets in the endcap/forward-calorimeter transition region, corresponding to $2.75 < |\eta| < 3.5$, must have $p_T > 35$ GeV.

The E_T^{miss} is a measure of the momentum of the escaping neutrinos, but is also affected by energy losses due to detector inefficiencies. The E_T^{miss} is calculated based on the vector sum of energy deposits in the calorimeter projected onto the transverse plane and is corrected for the presence of electrons, muons, and jets [43].

D. Identification of b-quark jets

The identification of jets originating from the fragmentation of b-quarks is one of the most important techniques for selecting top-quark events. Several properties can be used to distinguish b-quark jets from other jets: the long lifetime of b-hadrons, the large b-hadron mass, and the large branching ratio to leptons. The relatively long lifetime of b-flavored hadrons results in a significant flight path length, leading to reconstructable secondary vertices and tracks with large impact parameters relative to the primary vertex.

Jets containing b-hadrons are identified in the region $|\eta| < 2.5$ by reconstructing secondary and tertiary vertices from the tracks associated with each jet and combining lifetime-related information in a neural network [44]. Three different neural networks are trained corresponding to an optimal separation of b-quark jets, c-quark jets, and light-quark jets. The output of the networks is given in terms of probabilities p_b, p_c, and p_l, which are then combined to form a final discriminant. In order to achieve excellent rejection of c-quark jets the ratio p_b/p_c is calculated. The chosen working point corresponds to a b-tagging efficiency of about 54% and a light-quark jet rejection rate (reciprocal of the efficiency to b-tag light-quark jets) of 207 for jets in $t\bar{t}$ events. The misidentification efficiency for c-quark jets is 4.8%, as derived from simulated $t\bar{t}$ events. Jets passing the requirement on the identification discriminant are called b-tagged jets. Scale factors, determined from collision data, are applied to correct the b-tagging efficiency in simulated events to match the data.

IV. EVENT SELECTION

The event selection requires exactly one charged lepton, e or μ, exactly two or three jets, and $E_T^{\mathrm{miss}} > 30$ GeV. At least one of the jets must be b-tagged. A trigger matching requirement is applied according to which the lepton must lie within $\Delta R = 0.15$ cone around its trigger-level object. Candidate events are selected if they contain at least one good primary vertex candidate with at least five associated tracks. Events containing jets with transverse momentum $p_T > 20$ GeV failing to satisfy quality criteria against misreconstruction [41]

are rejected.

Since the multijet background is difficult to model precisely, its contribution is reduced by requiring the transverse mass of the lepton-E_T^{miss} system,

$$m_T\left(\ell E_T^{\text{miss}}\right) = \sqrt{2 p_T(\ell) \cdot E_T^{\text{miss}}\left[1 - \cos\left(\Delta\phi\left(\ell, E_T^{\text{miss}}\right)\right)\right]}\,, \tag{1}$$

to be larger than 30 GeV. Further reduction of the multijet background is achieved by placing an additional requirement on events with a charged lepton that is back-to-back with the leading jet in p_T. This is realized by the following condition between the lepton p_T and the $\Delta\phi\left(j_1, \ell\right)$:

$$p_T(\ell) > 40\,\text{GeV} \cdot \left(1 - \frac{\pi - |\Delta\phi\left(j_1, \ell\right)|}{\pi - 1}\right) \tag{2}$$

where j_1 denotes the leading jet.

In the subsequent analysis, signal events are divided into different analysis channels according to the sign of the lepton charge and the number of jets. In the 2-jet channels, exactly one jet is required to be b-tagged. To further reduce the W+jets background in these channels, the absolute value of the difference in pseudorapidity $|\Delta\eta|$ of the lepton and the b-tagged jet is required to be smaller than 2.4. In the 3-jet channels, events with exactly one and exactly two b-tagged jets are considered and separated accordingly. In the 3-jet-2-tag category no distinction is made between events with positive and negative lepton charge, since this channel is dominated by $t\bar{t}$ background and can be used to further constrain the uncertainty on the b-tagging efficiency. Finally, the resulting channels are referred to as: 2-jet-ℓ^+, 2-jet-ℓ^-, 3-jet-ℓ^+-1-tag, 3-jet-ℓ^--1-tag, and 3-jet-2-tag.

A control region is defined to be orthogonal to the signal region in the same kinematic phase space to validate the modeling of the backgrounds by simulated events. Events in these control regions feature exactly one b-tagged jet, which was identified with a less stringent b-tagging algorithm than used to define the signal region. The signal region is excluded from the control region by applying a veto.

V. BACKGROUND ESTIMATION

One of the largest backgrounds to single top-quark processes in the lepton+jets channel is W+jets production. If one of the jets contains b-hadrons or c-hadrons, these events have the same signature as signal events. Due to possible misidentification of a light-quark jet as a b-quark jet, W+light-jets production also contributes to the background. An equally important background comes from top-quark-antiquark ($t\bar{t}$) pair production events, which are difficult to separate from single top-quark events, since they contain top quarks as well. Another background is due to multijet production via the strong interaction. In these events a hadronic jet is misidentified as a lepton, usually an electron, or a real high-p_T lepton is produced within a jet due to the semileptonic decay of a heavy-flavor (b or c) hadron and satisfies the lepton isolation criteria. Other smaller backgrounds come from diboson (WW, WZ, and ZZ) and Z+jets production.

A. W/Z+jets background

The W+jets background is initially normalized to the theoretical prediction and then subsequently determined simultaneously both in the context of the multijet background estimation and as part of the extraction of the signal cross section. The estimated number of events of the much smaller Z+jets background is calculated using the theoretical prediction.

The cross sections for inclusive W-boson production and Z-boson production are predicted with NNLO precision using the FEWZ program [45], resulting in a LO-to-NNLO scale factor of 1.2 and an uncertainty of 4%. The uncertainty includes the uncertainty on the PDF and scale variations. The scale factor is applied to the prediction based on the LO ALPGEN calculation for the $W+b\bar{b}$, $W+c\bar{c}$, and W+light-jets samples. An uncertainty for associated jet production is estimated using variations of the factorization and renormalization scale and the ALPGEN matching parameter. These variations yield an uncertainty of 5% for the production of two additional light-quark jets and 15% for two additional heavy-quark jets. An additional relative uncertainty of 50% is assigned to the $W+b\bar{b}$ and $W+c\bar{c}$ production rates to take uncertainties on heavy-flavor production into account. This uncertainty is estimated using a tag-counting method in control regions [15].

The ALPGEN prediction for the $W+c$ process is scaled by a factor of 1.52 that is obtained from a study based on NLO calculations using MCFM [46]. Normalization uncertainties on the factorization and renormalization scale and PDF uncertainties are 24%.

The processes $W+b\bar{b}$, $W+c\bar{c}$, and W+light-jets, being asymmetric in lepton charge, are combined and are used as a single process in the binned maximum-likelihood fit to determine the signal yield.

B. Multijet background

Multijet background events pass the signal selection if a jet is misidentified as an isolated lepton or if the event has a non-prompt lepton that appears to be isolated. Since it is neither possible to simulate a sufficient number of those events nor possible to calculate the rate precisely, different techniques are developed to model multijet events and to estimate the production rate.

In the electron channel, misidentified jets are the main source of multijet background events. This motivates the jet-lepton method in which an electron-like jet is selected with special requirements and redefined as a lepton. This jet has to fulfill the same p_T and η requirements as a signal electron, and contain at least four tracks to reduce the contribution from converted photons. In addition, the jet must deposit 80–95% of its energy in the electromagnetic calorimeter. Events are selected using the same criteria as for the signal selection except for the selection of the electron. To avoid contamination of the selected sample with real electrons, events are rejected if they contain one or more leptons that are identified according to high-efficiency but low-purity identification criteria. The event is accepted if exactly one such 'jet lepton'
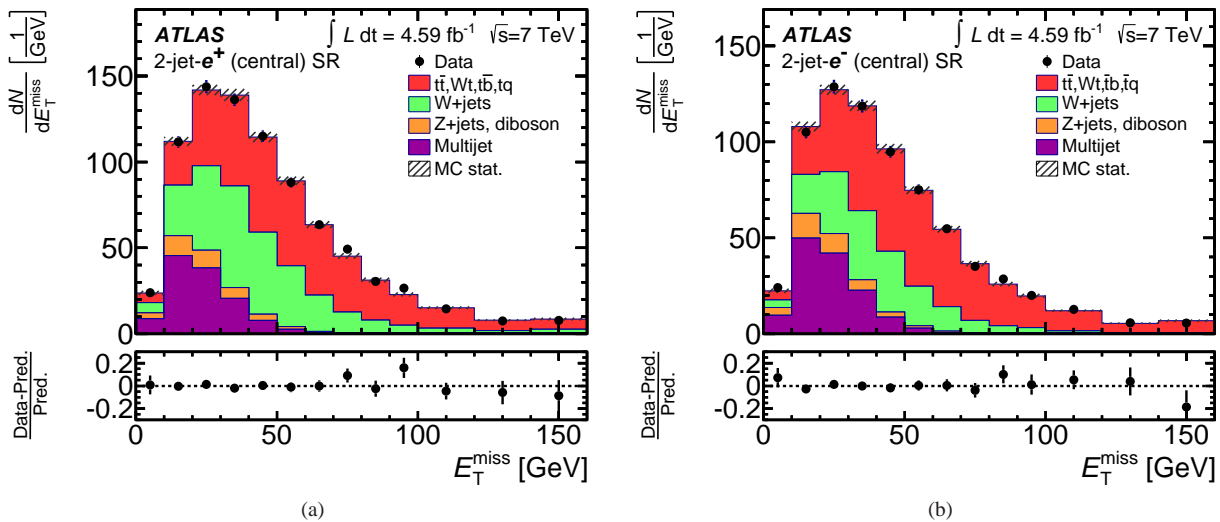
FIG. 2. E_T^{miss} distributions in the signal region (SR) for the (a) 2-jet-e^+ and (b) 2-jet-e^- channels for central electrons. The distributions are normalized to the result of a binned maximum-likelihood fit described in Sec. V B. The relative difference between the observed and expected number of events in each bin is shown in the lower panels.

is found. The jet-lepton selection is applied to a PYTHIA dijet sample and the resulting set of events is used to model the multijet background in the electron channel.

To determine the normalization of the multijet background in the electron channel, a binned maximum-likelihood fit to observed data in the E_T^{miss} distribution is performed after applying all selection criteria except for the E_T^{miss} requirement. In each channel two fits are performed separately; one for electrons in the central ($|\eta| < 1.5$) region and one for the endcap ($|\eta| > 1.5$) region of the electromagnetic calorimeter. The multijet template is fitted together with templates derived from Monte Carlo simulation for all other background processes whose rate uncertainties are accounted for in the fitting process in the form of additional constrained nuisance parameters. For the purpose of these fits the contributions from W+light-jets and $W+b\bar{b}$, $W+c\bar{c}$, $W+c$, the contributions from $t\bar{t}$ and single top-quark production, and the contributions from Z+jets and diboson production, are each combined into one template. Distributions normalized to the fit results in the 2-jet-e^+ and 2-jet-e^- signal regions for central electrons are shown in Fig. 2.

In the muon channel, the matrix method [47] is used to obtain both the normalization and shape of the multijet background. The method estimates the number of multijet background events in the signal region based on loose and tight lepton isolation definitions, the latter selection being a subset of the former. Hence, the loose selection is defined to contain leptons of similar kinematics, but results in much higher event yields and is, except for the muon isolation requirement, identical to the signal selection. The number of multijet events N_{fake}^{tight} passing the tight (signal) isolation requirements can be expressed as,

$$N_{fake}^{tight} = \frac{\varepsilon_{fake}}{\varepsilon_{real} - \varepsilon_{fake}} \cdot (N^{loose}\varepsilon_{real} - N^{tight}), \qquad (3)$$

where ε_{real} and ε_{fake} are the efficiencies for real and fake loose leptons being selected as tight leptons, N^{loose} is the number of selected events in the loose sample, and N^{tight} is the number of selected events in the signal sample. The fake efficiencies are determined from collision data in a sample of selected muon candidates with high impact parameter significance which is defined by the impact parameter divided by its uncertainty. The real efficiencies are also estimated from collision data using a "tag-and-probe" method, which is based on the identification of a tight lepton and a loose lepton in events originating from a leptonically decaying Z boson.

An uncertainty of 50% is applied to the estimated yield of multijet background events based on comparisons of the rates obtained by using alternative methods, i.e. the matrix method in the electron channel and the jet-lepton method in the muon channel, and using an alternative variable, i.e. $m_T(\ell E_T^{miss})$ instead of E_T^{miss} for the binned maximum-likelihood fit.

C. $t\bar{t}$ production and other backgrounds

The $t\bar{t}$ cross section is calculated at NNLO in QCD including resummation of next-to-next-to-leading logarithmic (NNLL) soft gluon terms [48–52] with Top++2.0 [53]. The PDF and α_s uncertainties are calculated using the PDF4LHC prescription [54] with the MSTW2008 NNLO [10, 55] at 68% confidence level (CL), the CT10 NNLO [26, 56], and the NNPDF2.3 [57] PDF sets, and are added in quadrature to the scale uncertainty, yielding a final uncertainty of 6%.

Since Wt production is charge symmetric with respect to top-quark and top-antiquark production, the combined cross section of $\sigma(Wt) = 15.7 \pm 1.1$ pb [58] is used in the analysis. The predicted cross sections for s-channel production are $\sigma(t\bar{b}) = 3.1 \pm 0.1$ pb and $\sigma(\bar{t}b) = 1.4 \pm 0.1$ pb [59]. The pre-

dictions of $\sigma(Wt)$, $\sigma(t\bar{b})$, and $\sigma(\bar{t}b)$ are given at approximate NNLO precision, applying soft-gluon resummation. Theoretical uncertainties including PDF and scale uncertainties are 4.4% [59] for s-channel single top-quark production and 7.0% [58] for Wt production. The PDF uncertainties are evaluated using the 40 associated eigenvector PDF sets of MSTW 2008 at 90% CL. The cross sections given above are used to compute the number of expected single top-quark events by normalizing the samples of simulated events.

All top-quark background processes are shown combined in the figures and used as a single process in the analysis. The charge asymmetry in s-channel production is taken from the approximate NNLO prediction.

Diboson events (WW, WZ and ZZ) are normalized to the NLO cross-section prediction calculated with MCFM [46]. The cross-section uncertainty for these processes is 5%.

D. Event yields

Table I provides the event yields after event selection. The yields are presented for the tagged channels, where exactly one b-tagged jet is required, separated according to the lepton charge and for the 3-jet-2-tag channel. Small contributions from the tq process in the ℓ^- regions and the $\bar{t}q$ process in the ℓ^+ regions originate from lepton charge misidentification.

VI. SIGNAL AND BACKGROUND DISCRIMINATION

To separate t-channel single top-quark signal events from background events, several kinematic variables are combined to form powerful discriminants by employing neural networks. A large number of potential input variables were studied, including not only kinematic variables of the identified physics objects, but also variables obtained from the reconstruction of the W boson and the top quark.

A. Top-quark reconstruction

When reconstructing the W boson, the transverse momentum of the neutrino is given by the x- and y-components of the $E_{\mathrm{T}}^{\mathrm{miss}}$, while the unmeasured z-component of the neutrino momentum $p_z(\nu)$ is inferred by imposing a W-boson mass constraint on the lepton–neutrino system. Since the constraint leads to a quadratic equation for $p_z(\nu)$, a two-fold ambiguity arises. In the case of two real solutions, the one with the lower $|p_z(\nu)|$ is chosen. In case of complex solutions, which can occur due to the low $E_{\mathrm{T}}^{\mathrm{miss}}$ resolution, a kinematic fit is performed that rescales the neutrino p_x and p_y such that the imaginary part vanishes and at the same time the transverse components of the neutrino momentum are kept as close as possible to the $E_{\mathrm{T}}^{\mathrm{miss}}$. As a result of this algorithm, the four-momentum of the neutrino is reconstructed.

The top quark is reconstructed by adding the four-momenta of the reconstructed W boson and the b-tagged jet. Several

angular variables, invariant masses and differences in p_{T} are defined using the reconstructed physics objects.

B. Selection of discriminating variables

The NeuroBayes [60] tool is used for preprocessing the input variables and for the training of the NNs. The ranking of the variables in terms of their discrimination power is automatically determined as part of the preprocessing step and is independent of the training procedure [15]. Only the highest-ranking variables are chosen for the training of the NNs. Separate NNs are trained in the 2-jet channel and 3-jet channel. In the training, no separation is made according to lepton charge. Dedicated studies show that training in the channels separated by lepton charge does not lead to an improvement in sensitivity.

As a result of the optimization procedure in the 2-jet channel, 13 kinematic variables are identified as inputs to the NN. In the 3-jet channel, 11 variables are used. It was found that reducing the number of variables further would result in a considerable loss of sensitivity. The input variables to the NNs are listed in Table II. The separation between signal and the two most important backgrounds, the top-quark background and the combined W+light-jets, $W+c\bar{c}$, and $W+b\bar{b}$ background, is shown in Fig. 3 for the two most important discriminating variables in the 2-jet channel.

The modeling of the input variables is checked in a control region (see Sec. IV for the definition) that is enriched in W+jets events. Figures 4 and 5 show the three most discriminating variables in the 2-jet-$\ell^\pm$ and 3-jet-$\ell^\pm$-1-tag channels, respectively. Good modeling of the variables is observed.

C. Neural network training

After choosing a set of variables based on the criteria outlined above, the analysis proceeds with the training of the NNs using a three-layer feed-forward architecture. Samples of simulated events are used for the training process. All background processes are used in the training, except for the multijet background whose modeling is associated with large uncertainties. The ratio of signal events to background events in the training is chosen to be 1:1, while the different background processes are weighted relative to each other according to the number of expected events.

Regularization techniques are applied in the training process to dampen statistical fluctuations in the training sample and to avoid overtraining. At the preprocessing stage mentioned above (Sec. VI B), the input variables are transformed in several steps to define new input variables that are optimally prepared to be fed into an NN. First, the variables are transformed, such that they populate a finite interval and are distributed according to a uniform distribution. The influence of outliers is thereby strongly reduced. The distributions of the transformed variables are discretized using 100 bins, and the distributions for signal events are divided by the sum of signal and background events bin-by-bin, yielding the purity

TABLE I. Predicted and observed events yields for the 2-jet and 3-jet channels considered in this measurement. The multijet background is estimated using data-driven techniques (see Sec. V B); an uncertainty of 50% is applied. All the other expectations are derived using theoretical cross sections and their uncertainties (see Sec. V A and Sec. V C).

| | 2-jet channels | | 3-jet channels | | |
	ℓ^+	ℓ^-	ℓ^+	ℓ^-	2-tag
tq	2550 ± 220	3.6 ± 0.3	845 ± 74	1.2 ± 0.1	309 ± 26
$\bar{t}q$	1.5 ± 0.1	1390 ± 120	0.52 ± 0.05	435 ± 38	162 ± 14
$t\bar{t}, Wt, t\bar{b}, \bar{t}b$	5250 ± 530	5130 ± 510	8200 ± 820	8180 ± 820	5850 ± 580
$W^+ + b\bar{b}, c\bar{c}$,light jets	5700 ± 2500	16.3 ± 8.2	2400 ± 1200	11.5 ± 5.7	200 ± 100
$W^- + b\bar{b}, c\bar{c}$,light jets	9.2 ± 4.6	3400 ± 1700	4.1 ± 2.0	1470 ± 740	137 ± 68
$W+c$	1460 ± 350	1620 ± 390	388 ± 93	430 ± 100	6.5 ± 1.6
Z+jets, diboson	370 ± 220	310 ± 180	190 ± 120	180 ± 110	22 ± 13
Multijet	750 ± 340	740 ± 370	320 ± 160	440 ± 220	21 ± 11
Total expectation	16100 ± 2600	12600 ± 2000	12400 ± 1500	11100 ± 1100	6710 ± 610
Data	16198	12837	12460	10819	6403

TABLE II. Input variables of the NNs in the 2-jet channels and in the 3-jet channels. The definitions of the variables use the term *leading jet* and *2nd leading jet*, defined as the jet with the highest or 2nd highest p_T, respectively. In the 2-jet channels, exactly one jet is required to be b-tagged. The jet that is not b-tagged is denoted *untagged* jet.

Variables used in the 2-jet channels and the 3-jet channels	
$m(\ell\nu b)$	The invariant mass of the reconstructed top quark.
$m_T(\ell E_T^{miss})$	The transverse mass of the lepton–E_T^{miss} system, as defined in Eq. (1).
$\eta(\ell\nu)$	The pseudorapidity of the system of the lepton and the reconstructed neutrino.
$m(\ell b)$	The invariant mass of the charged lepton and the b-tagged jet.
H_T	The scalar sum of the transverse momenta of the jets, the charged lepton, and the E_T^{miss}.

Variables used in the 2-jet channels only	
$m(jb)$	The invariant mass of the untagged jet and the b-tagged jet.
$|\eta(j)|$	The absolute value of the pseudorapidity of the untagged jet.
$\Delta R(\ell, j)$	ΔR between the charged lepton and the untagged jet.
$\Delta R(\ell\nu b, j)$	ΔR between the reconstructed top quark and the untagged jet.
$|\eta(b)|$	The absolute value of the pseudorapidity of the b-tagged jet.
$|\Delta p_T(\ell, j)|$	The absolute value of the difference between the transverse momentum of the charged lepton and the untagged jet.
$|\Delta p_T(\ell\nu b, j)|$	The absolute value of the difference between the transverse momentum of the reconstructed top quark and the untagged jet.
E_T^{miss}	The missing transverse momentum.

Variables used in the 3-jet channels only	
$|\Delta y(j_1, j_2)|$	The absolute value of the rapidity difference of the leading and 2nd leading jets.
$m(j_2 j_3)$	The invariant mass of the 2nd leading jet and the 3rd leading jet.
$\cos\theta(\ell, j)_{\ell\nu b \, r.f.}$	The cosine of the angle θ between the charged lepton and the leading untagged jet in the rest frame of the reconstructed top quark.
$\Sigma\eta(j_i)$	The sum of the pseudorapidities of all jets in the event.
$m(j_1 j_2)$	The invariant mass of the two leading jets.
$p_T(\ell\nu b)$	The transverse momentum of the reconstructed top quark.
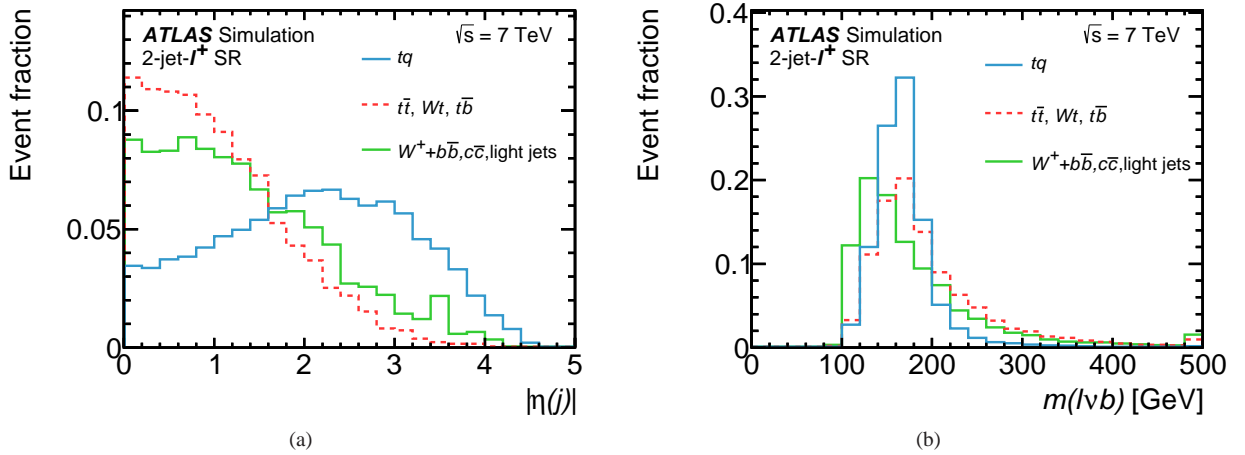
FIG. 3. Probability densities of the two most important discriminating variables in the 2-jet channels, shown in the 2-jet-ℓ^+ channel in the signal region (SR). The distributions are normalized to unit area. The absolute value of the pseudorapidity of the untagged jet $|\eta(j)|$ is shown in (a), and the invariant mass of the reconstructed top quark $m(\ell\nu b)$ is shown in (b).

distributions in each variable. Next, these purity curves are fitted with a regularized spline function, thereby yielding a continuous transformation from the original input variables to the purities. By means of the spline fit statistical fluctuations in the input variables are significantly reduced. Applying the continuous purity functions to the input variables yields purity distributions that are further transformed, such that the distributions of the resulting variables are centered at zero and have an RMS of one. These variables are input to the NNs. In the training process, the network structure is pruned to arrive at a minimal topology, i.e. statistically insignificant network connections and nodes are removed.

In Fig. 6, the probability densities of the resulting NN discriminants are shown for the signal, the top-quark backgrounds, and the combined W+light-jets, W+$c\bar{c}$, and W+$b\bar{b}$ background. The separation between signal and backgrounds is equally good for the positive and the negative charge channels, which demonstrates that the choice of training the NNs with a charge-combined sample is appropriate.

D. Extraction of the signal yield

The cross sections $\sigma(tq)$ and $\sigma(\bar{t}q)$ are extracted by performing a binned maximum-likelihood fit to the NN discriminant distributions in the 2-jet-ℓ^+, 2-jet-ℓ^-, 3-jet-ℓ^+-1-tag, and 3-jet-ℓ^--1-tag channels and to the event yield in the 3-jet-2-tag channel, treating t-channel top-quark and t-channel top-antiquark production as independent processes. The signal rates, the rate of the combined top-quark background, the rate of the combined W+light-jets, W+$c\bar{c}$, and W+$b\bar{b}$ background, and the b-tagging efficiency correction factor (discussed in Sec. III D) are fitted in all channels simultaneously. The event yields of the multijet background and the W+c background are not allowed to vary in the fit, but instead are fixed to the estimates given in Table I. The cross-section ratio is subsequently computed as $R_t = \sigma(tq)/\sigma(\bar{t}q)$.

The maximum-likelihood function is given by the product of Poisson probability terms for the individual histogram bins (see Ref. [15]). Gaussian priors are added multiplicatively to the maximum-likelihood function to constrain the background rates subject to the fit and the correction factor of the b-tagging efficiency to their predictions within the associated uncertainties.

The sensitivity to the background rates is mostly given by the background-dominated region close to zero in the NN discriminant distributions, while the sensitivity to the b-tagging efficiency stems from the event yield in the 3-jet-2-tag channel with respect to the event yields in the 1-tag channels.

In Fig. 7 the observed NN discriminant distributions are shown compared to the compound model of signal and background normalized to the fit results. Figures 8 and 9 show the three most discriminating variables normalized to the fit results in the 2-jet-$\ell^\pm$ and 3-jet-$\ell^\pm$-1-tag channels, respectively. Differences between data and prediction are covered by the normalization uncertainty of the different processes after the fit.

E. High-purity region

A high-purity region (HPR) is defined to measure the differential cross sections in the 2-jet-ℓ^+ and 2-jet-ℓ^- channels, by requiring the NN discriminant to be larger than 0.8. In the 2-jet-ℓ^+ HPR the signal contribution is twice as large as the background contribution. The signal and background contributions in the 2-jet-ℓ^- HPR are of approximately the same size. The result of the fit described above is used to normalize the background in the HPR. Figure 10 shows the three most discriminating variables in the 2-jet-ℓ^+ and 2-jet-ℓ^- high-purity channels, normalized to the fit results. The data are well described by the predicted compound model.
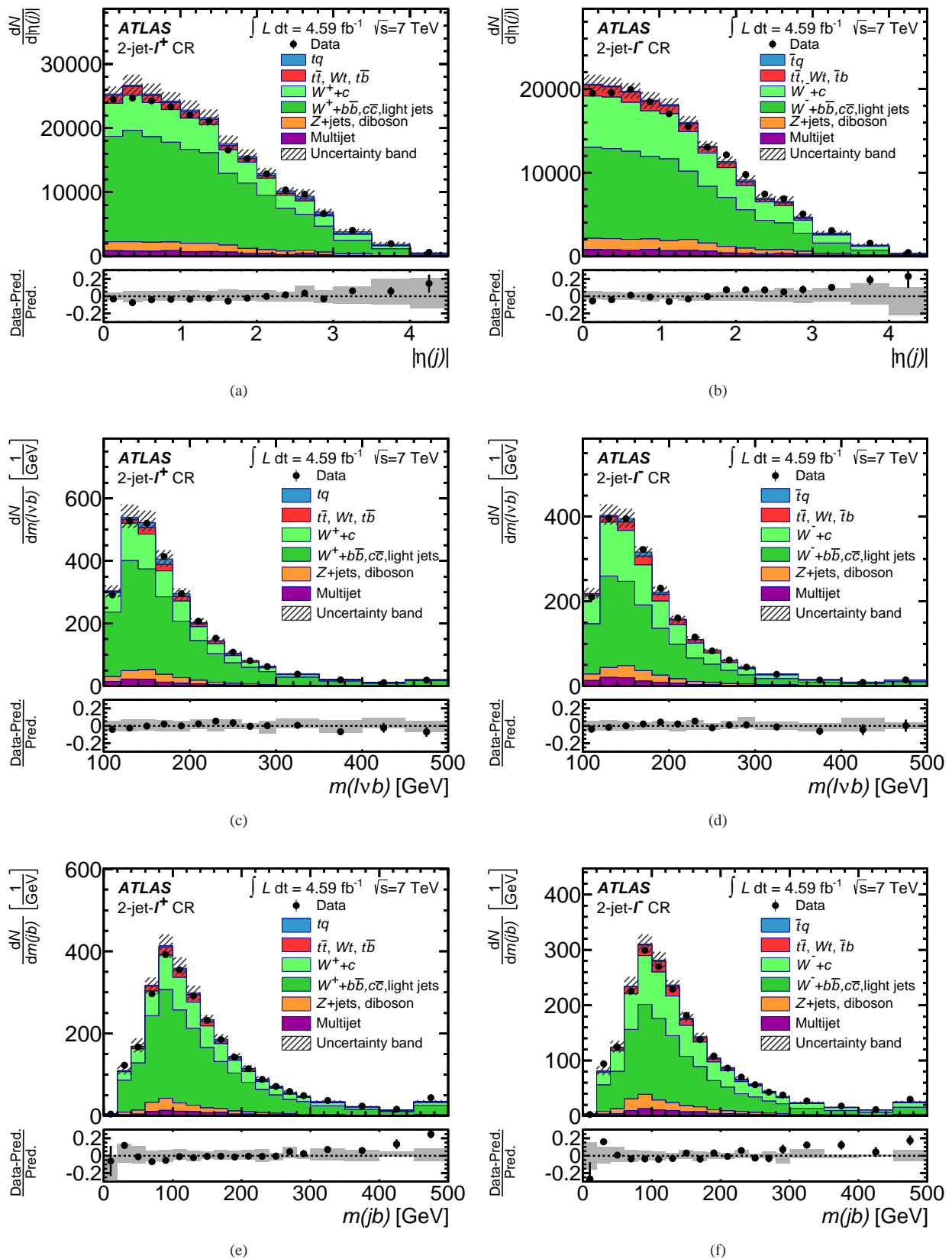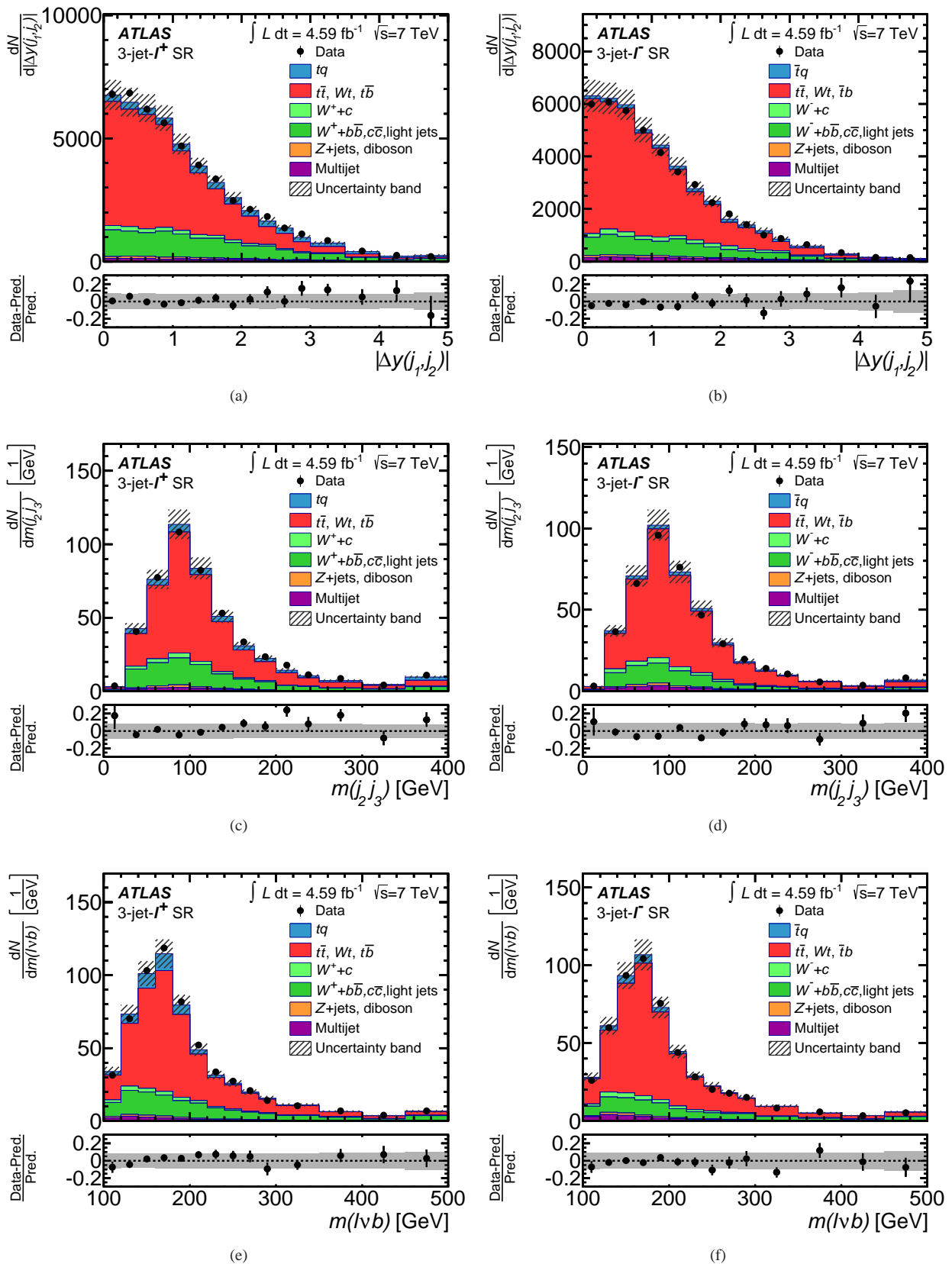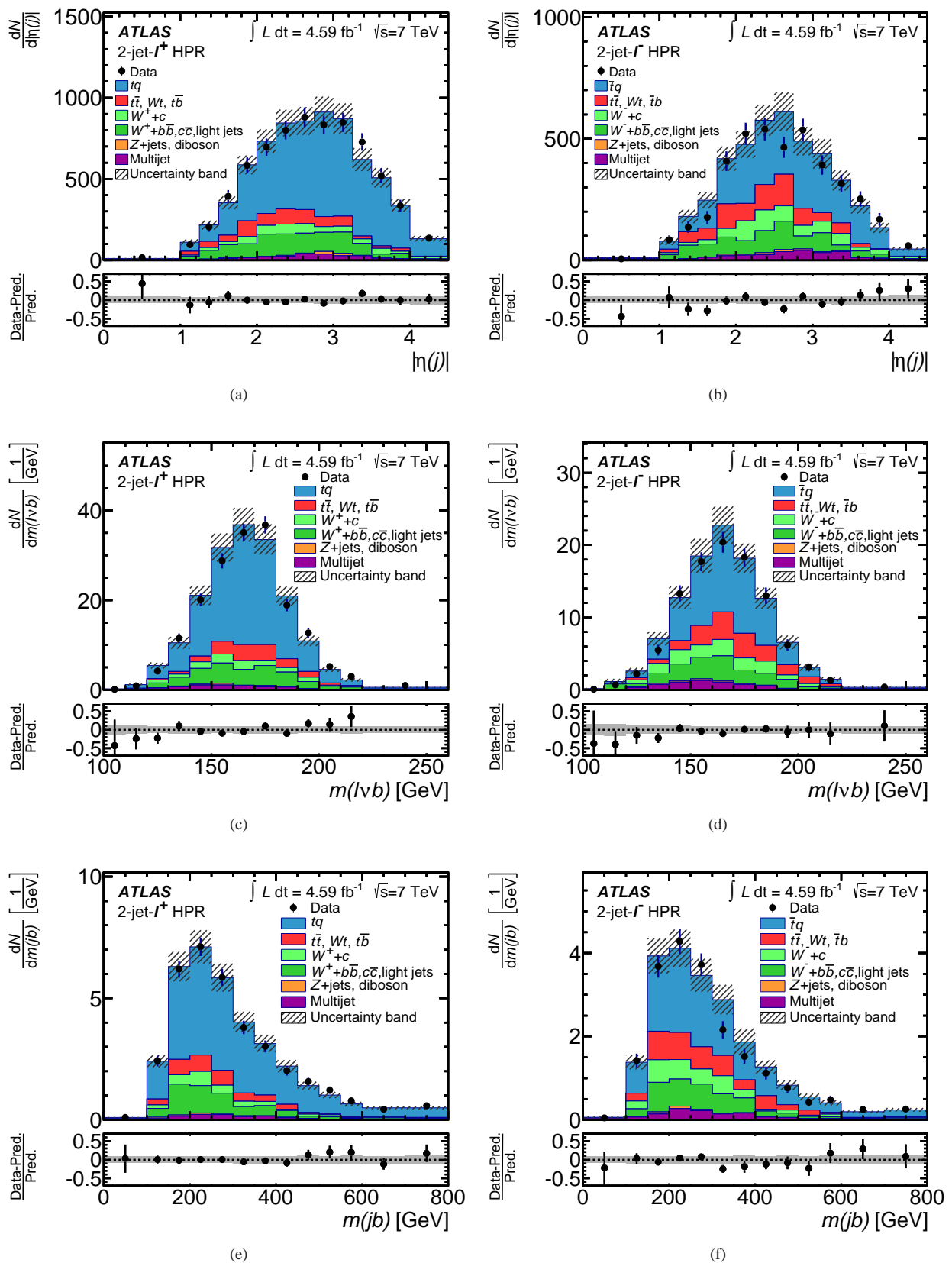
FIG. 4. Distributions of the three most important discriminating variables in the 2-jet-ℓ^+ and 2-jet-ℓ^- channels in the control region (CR). Figures (a) and (b) display the absolute value of the pseudorapidity of the untagged jet $|\eta(j)|$. Figures (c) and (d) show the invariant mass of the reconstructed top quark $m(\ell\nu b)$, (e) and (f) the invariant mass of the untagged and the b-tagged jet $m(jb)$. The last histogram bin includes overflows. The multijet and the W+jets event yields are determined by a fit to the E_T^{miss} distribution as described in Sec. V B. The uncertainty band represents the normalization uncertainty due to the uncertainty on the jet energy scale and the Monte Carlo statistical uncertainty. The relative difference between the observed and expected number of events in each bin is shown in the lower panels.

FIG. 5. Distributions of the three most important discriminating variables in the 3-jet-ℓ^+ and 3-jet-ℓ^- channels in the control region (CR). Figures (a) and (b) display the absolute value of the rapidity difference of the leading and 2$^{\text{nd}}$ leading jet $|\Delta y(j_1, j_2)|$, (c) and (d) the invariant mass of the 2$^{\text{nd}}$ leading jet and the 3$^{\text{rd}}$ jet $m(j_2 j_3)$, and (e) and (f) show the invariant mass of the reconstructed top quark $m(\ell \nu b)$. The last histogram bin includes overflows. The multijet and the W+jets event yields are determined by a fit to the $E_{\text{T}}^{\text{miss}}$ distribution as described in Sec. V B. The uncertainty band represents the normalization uncertainty due to the uncertainty on the jet energy scale and the Monte Carlo statistical uncertainty. The relative difference between the observed and expected number of events in each bin is shown in the lower panels.

FIG. 6. Probability densities of the NN discriminants in the 2-jet channels and 3-jet channels in the signal region (SR): (a) 2-jet-ℓ^+ channel, (b) 2-jet-ℓ^- channel, (c) 3-jet-ℓ^+ channel, and (d) 3-jet-ℓ^- channel. The distributions are normalized to unit area.
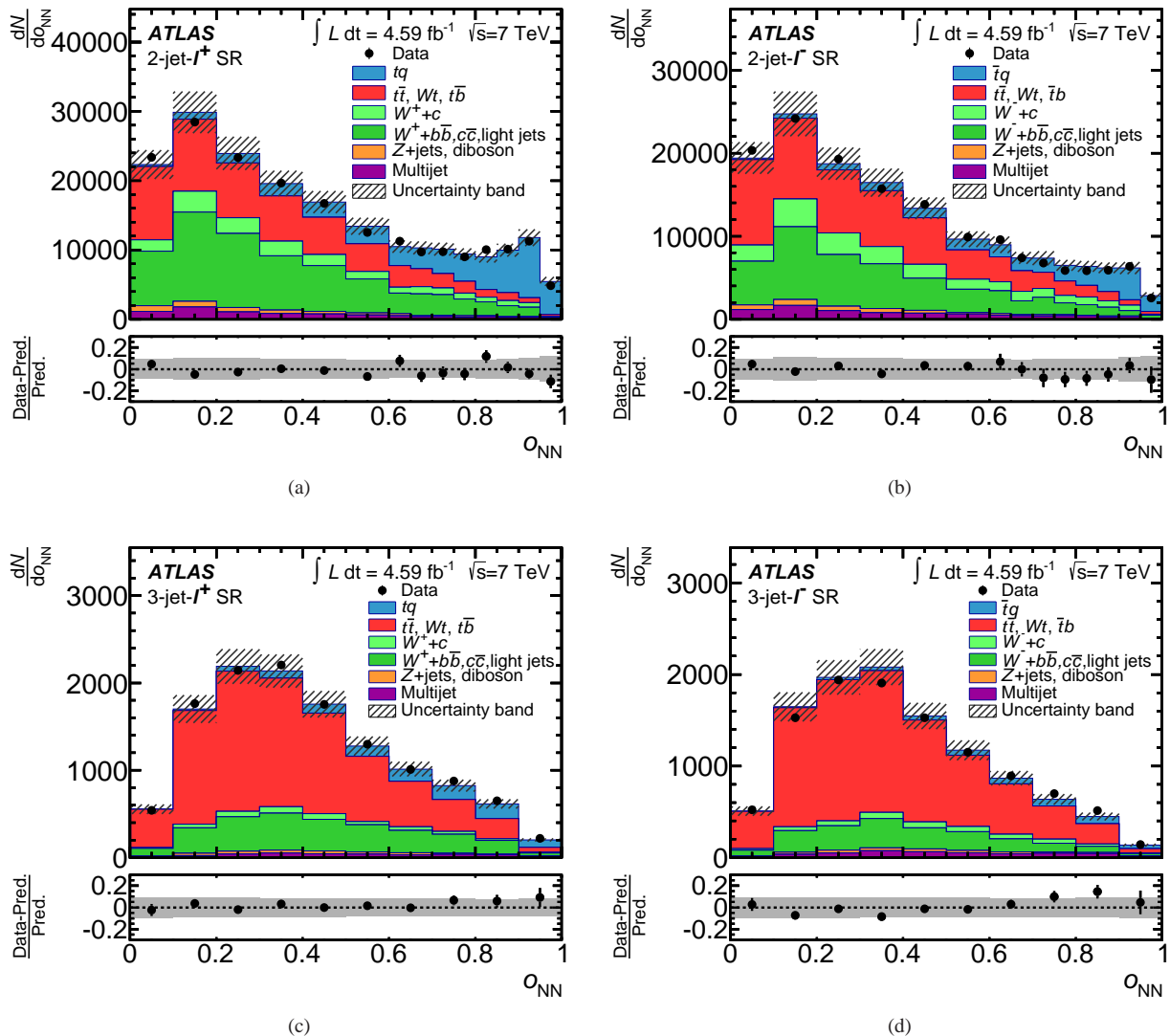
FIG. 7. Neural network discriminant distributions normalized to the result of the binned maximum-likelihood fit in (a) the 2-jet-ℓ^+ channel, (b) the 2-jet-ℓ^- channel, (c) the 3-jet-ℓ^+ channel, and (d) the 3-jet-ℓ^- channel. The uncertainty band represents the normalization uncertainty of all processes after the fit and the Monte Carlo statistical uncertainty, added in quadrature. The relative difference between the observed and expected number of events in each bin is shown in the lower panels.

FIG. 8. Distributions of the three most important discriminating variables in the 2-jet-ℓ^+ and 2-jet-ℓ^- channels in the signal region normalized to the result of the binned maximum-likelihood fit to the NN discriminant as described in Sec. VI D. Figures (a) and (b) display the absolute value of the pseudorapidity of the untagged jet $|\eta(j)|$. Figures (c) and (d) show the invariant mass of the reconstructed top quark $m(\ell\nu b)$, (e) and (f) the invariant mass of the b-tagged and the untagged jet $m(jb)$. The last histogram bin includes overflows. The uncertainty band represents the normalization uncertainty of all processes after the fit and the Monte Carlo statistical uncertainty, added in quadrature. The relative difference between the observed and expected number of events in each bin is shown in the lower panels.

FIG. 9. Distributions of the three most important discriminating variables in the 3-jet-ℓ^+ and 3-jet-ℓ^- channels in the signal region normalized to the result of the binned maximum-likelihood fit to the NN discriminant as described in Sec. VI D. Figures (a) and (b) display the absolute value of the rapidity difference of the leading and 2nd leading jet $|\Delta y(j_1, j_2)|$, (c) and (d) the invariant mass of the 2nd leading jet and the 3rd jet $m(j_2 j_3)$, and (e) and (f) show the invariant mass of the reconstructed top quark $m(\ell\nu b)$. The last histogram bin includes overflows. The uncertainty band represents the normalization uncertainty of all processes after the fit and the Monte Carlo statistical uncertainty, added in quadrature. The relative difference between the observed and expected number of events in each bin is shown in the lower panels.

FIG. 10. Distributions of the three most important discriminating variables in the 2-jet-ℓ^+ and 2-jet-ℓ^- channels in the high-purity region (HPR) normalized to the result of the binned maximum-likelihood fit to the NN discriminant as described in Sec. VI D. Figures (a) and (b) display the absolute value of the pseudorapidity of the untagged jet $|\eta(j)|$. Figures (c) and (d) show the invariant mass of the reconstructed top quark $m(\ell\nu b)$, (e) and (f) the invariant mass of the b-tagged and the untagged jet $m(jb)$. The last histogram bin includes overflows. The uncertainty band represents the normalization uncertainty of all processes after the fit and the Monte Carlo statistical uncertainty, added in quadrature. The relative difference between the observed and expected number of events in each bin is shown in the lower panels.

VII. SYSTEMATIC UNCERTAINTIES

For both the physical object definitions and the background estimations, systematic uncertainties are assigned to account for detector calibration and resolution uncertainties, as well as the uncertainties of theoretical predictions. These variations affect both normalization and shape of distributions for signal and backgrounds. The uncertainties can be split into the following categories: physics object modeling, Monte Carlo generators, PDFs, theoretical cross-section normalization, and luminosity.

A. Physics object modeling

Systematic uncertainties on the reconstruction and energy calibration of jets, electrons and muons are propagated through the entire analysis. The main source of object modeling uncertainty comes from the jet energy scale (JES). The JES uncertainty has been evaluated for the in situ jet calibration [41, 42], which uses Z+jet, γ+jet, and dijet p_T-balance measurements in data. The JES uncertainty is evaluated in several different categories:

- Detector: The different p_T-balance measurements have uncertainties due to the jet resolution, the electron and photon energy scale and the photon purity.

- Physics modeling: The uncertainties in the in situ calibration techniques due to the choice of Monte Carlo generator, radiation modeling, and the extrapolation of $\Delta\phi$ between the jet and the Z boson.

- Statistics: The uncertainty due to the limited size of the data sets of the in situ jet calibration measurements.

- Mixed detector and modeling: In this category the uncertainty due to the modeling of the underlying event and soft radiation as well as modeling of the jet fragmentation are considered.

- η intercalibration modeling: The uncertainty in the dijet-p_T-balance technique due to the modeling of additional parton radiation is estimated by comparing dijet events simulated with PYTHIA and HERWIG. This JES category is the largest contribution from the jet energy scale to the cross-section measurements.

- Close-by jets: The jet calibration can be affected by the presence of close-by jets, located at radii $\Delta R < 1.0$.

- Pile-up: Uncertainties due to the modeling of the large pile-up effects in data are included as a function of jet p_T and η.

- Flavor composition: This uncertainty covers effects due to the difference in quark–gluon composition between the jets used in the calibration and the jets used in this analysis. Since the response to quark and gluon jets is different, the uncertainty on the quark–gluon composition in a given data sample leads to an uncertainty in the jet calibration.

- Flavor response: In this category an uncertainty is considered due to imperfect knowledge of the calorimeter response to light-quark jets and gluon jets.

- b-JES: An additional JES uncertainty is evaluated for b-quark jets by varying the modeling of b-quark fragmentation.

The uncertainty due to the jet energy resolution is modeled by varying the p_T of the jets according to the systematic uncertainties of the resolution measurement performed on data using the dijet-balance method [61]. The effect of uncertainties associated with the jet vertex fraction is also considered for each jet.

The tagging efficiencies of b-jets, c-jets, and light jets are derived from data [62–64] and parameterized as a function of p_T and η of the jet. The corresponding efficiencies in simulated events are corrected to be the same as those observed in data, and the uncertainties in the calibration method are propagated to the analysis. The difference in the b-tagging efficiency between jets initiated by b-quark and b-antiquark is ∼1%, estimated from simulated tq and $\bar{t}q$ events. To account for a possible uncertainty in the modeling of the detector response the full difference is taken as a systematic uncertainty. In Table III this uncertainty is called $b/\bar{b}$ acceptance.

The uncertainties due to lepton reconstruction, identification and trigger efficiencies are evaluated using tag-and-probe methods in $Z \rightarrow \ell\ell$ events. Uncertainties due to the energy scale and resolution are considered for electrons and muons. Additionally, the lepton charge misidentification is taken into account and was evaluated to be about 0.1%. All lepton uncertainties are summarized in Table III in one item.

Other minor uncertainties are assigned to the reconstruction of E_T^{miss} and to account for the impact of pile-up collisions on the calculation of E_T^{miss}. The uncertainties on E_T^{miss} are summarized under E_T^{miss} modeling in Table III.

B. Monte Carlo generators

Systematic uncertainties arising from the modeling of the single top-quark signal, the $t\bar{t}$ background, and the W+jets background are taken into account.

The uncertainty due to the choice of single top-quark t-channel generator and parton shower model is estimated by comparing events generated with POWHEG-BOX interfaced to PYTHIA and events generated with the NLO matrix-element generator aMC@NLO [65] and showered with HERWIG and JIMMY. Again the fixed four-flavor PDF set CT10f4 [26] is used, and the renormalization and factorization scales are set to $\mu_R = \mu_F = 4 \cdot \sqrt{m_b^2 + p_{T,b}^2}$, where $m_b = 4.75$ GeV is the b-quark mass, and $p_{T,b}$ is the transverse momentum of the b-quark. The uncertainty on the choice of μ_R and μ_F is estimated using events generated with POWHEG-BOX interfaced to PYTHIA. Factorization and renormalization scales are varied independently by factors of 0.5 and 2.0, while the scale of the parton shower is varied consistently with the renormalization scale. The uncertainty

related to scale variations is then given by the envelope of all variations.

The modeling uncertainty for the $t\bar{t}$ background is evaluated by comparing events simulated with the NLO generator POWHEG-BOX interfaced to PYTHIA and the multi-leg LO generator ALPGEN interfaced to HERWIG. An additional uncertainty for the top-quark background processes comes from the amount of initial-state and final-state radiation, estimated using dedicated ACERMC samples interfaced to PYTHIA where parameters controlling initial-state and final-state radiation (ISR/FSR) emission are varied. The variations of the parameters are constrained by a measurement of $t\bar{t}$ production with a veto on additional central jet activity [66].

A shape uncertainty is assigned to the W+jets background, based on variation of the choices of the matching scale and of the functional form of the factorization scale in ALPGEN.

The impact of using simulation samples of limited size is also taken into account.

C. Parton distribution function

The systematic uncertainties related to the PDFs are taken into account for the acceptance of all single top-quark processes and $t\bar{t}$ production. The simulated events are reweighted according to each of the PDF uncertainty eigenvectors. The uncertainty is calculated following the recommendation of the respective PDF group. The final PDF uncertainty is the envelope of the estimated uncertainties for the CT10 PDF set, the MSTW2008nlo [55] PDF set and the NNPDF2.3 [57] PDF set. For all PDFs the variable flavor number scheme [67] is used.

D. Theoretical cross-section normalization

In Sec. V the theoretical cross sections and their uncertainties are quoted for each background process. Since the $t\bar{t}$, single top-quark Wt and s-channel processes are grouped together in the statistical analysis, their uncertainties are added in proportion to their relative fractions, leading to a combined uncertainty of 6.7%. The uncertainty on the combined Z+jets and diboson background is 60% including a conservative estimate of the uncertainty of the heavy-flavor fraction of 50%, while the uncertainties of the W+jets backgrounds are 24% for $W+c$ and 36% for the combined $W+b\bar{b}$, $c\bar{c}$ and light jets including the same heavy-flavor-fraction uncertainty on the $b\bar{b}$ and $c\bar{c}$ contributions. Additionally, an uncertainty on the relative fraction of 2-jet to 3-jet events of 5% for events with light-flavor jets and 7% for events with heavy-flavor jets is applied for the W+jets estimation. This uncertainty was estimated by varying the following input parameters of the generation with ALPGEN by a factor of two: the hard scattering scale, the coupling of the hard interaction, and the minimum p_T and ΔR separation of the partons.
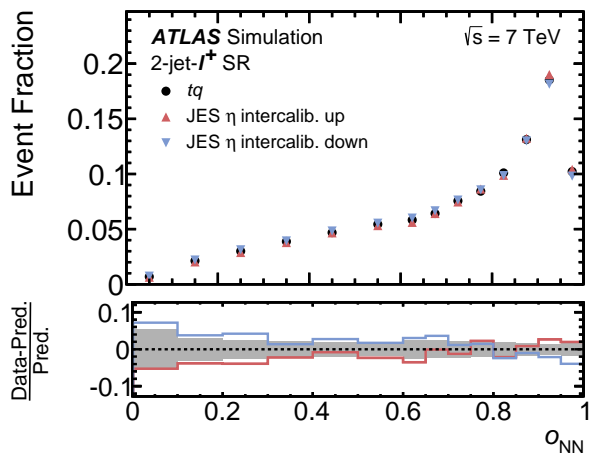
FIG. 11. The normalized shape variation of the NN discriminant for the JES variation due to the uncertainty on the η intercalibration in the 2-jet-ℓ^+ channel, shown for the tq sample. The nominal shape is shown by the black points. Red denotes the JES shift-up and blue the NN response for JES shift-down. In the lower panel the relative difference between the number of expected events in the systematic variation and the nominal distribution is shown for each bin. The grey uncertainty band in the lower histogram represents the normalization uncertainty due to the Monte Carlo statistical uncertainty.

E. Luminosity

The luminosity measurement is calibrated using dedicated beam-separation scans, referred to as van der Meer scans, where the absolute luminosity can be inferred from the measurement of the beam parameters [21]. The resulting uncertainty is 1.8%.

F. Uncertainties on the cross-section measurements

The systematic uncertainties on the individual top-quark and top-antiquark cross-section measurements and their ratio are determined using pseudo-experiments that account for variations of the signal acceptance, the background rates, and the shape of the NN discriminant due to all sources of uncertainty described above. As an example, Fig. 11 shows the shape variation of the NN discriminant for t-channel single top-quark signal events due to the variation of the JES because of the uncertainty on the η intercalibration. The correlations between the different channels and the physics processes are fully accounted for. The probability densities of all possible outcomes of the measurements of $\sigma(tq)$, $\sigma(\bar{t}q)$ and R_t are obtained by performing the measurements on the pseudo-data. The values measured in data are used as central values when generating the pseudo-experiments. The root mean squares of the estimator distributions of the measured quantities are estimators of the measurement uncertainties.

Table III summarizes the contributions of the various

sources of systematic uncertainty to the uncertainties on the measured values of $\sigma(tq)$, $\sigma(\bar{t}q)$, R_t and $\sigma(tq+\bar{t}q)$. The dominant systematic uncertainty on the cross sections is the JES η-intercalibration uncertainty since one of the prominent features of tq production is a jet in the forward region.

VIII.   TOTAL CROSS-SECTION MEASUREMENTS

After performing the binned maximum-likelihood fit and estimating the total uncertainty, the cross sections of top-quark and top-antiquark production in the t-channel and their cross-section ratio R_t are measured to be:

$$\sigma(tq) = 46 \pm 1\,(\text{stat.}) \pm 6\,(\text{syst.})\,\text{pb} \qquad = 46 \pm 6\,\text{pb},$$
$$\sigma(\bar{t}q) = 23 \pm 1\,(\text{stat.}) \pm 3\,(\text{syst.})\,\text{pb} \qquad = 23 \pm 4\,\text{pb}\quad \text{and}$$
$$R_t = 2.04 \pm 0.13\,(\text{stat.}) \pm 0.12\,(\text{syst.}) = 2.04 \pm 0.18,$$

assuming a top-quark mass of $m_t = 172.5$ GeV. Figure 12 compares the measured values of $\sigma(tq)$, $\sigma(\bar{t}q)$, and R_t to NLO predictions from MCFM [11] and Hathor [68] using different PDF sets. Uncertainties on the predicted values include the uncertainty on the renormalization and factorization scales and the combined PDF and α_s uncertainty of the respective PDF set.

All PDF predictions are in agreement with all measurements. For $\sigma(\bar{t}q)$, the predictions of all PDF sets agree well with each other and with the measured value. The predictions for $\sigma(tq)$ and R_t with the ABM11 PDF set show an offset compared to the other predictions. With increasing precision, the measurement of these observables could provide a way to further constrain the involved PDFs.

A.   Inclusive cross-section measurement

The inclusive t-channel cross section $\sigma(tq+\bar{t}q)$ is extracted by using only one scale factor $\beta(tq+\bar{t}q)$ in the likelihood function, scaling the top-quark and the top-antiquark contributions simultaneously. The top-quark-to-antiquark ratio is taken from the approximate NNLO prediction [9] (see Sec. I). The systematic uncertainties on the measured value of inclusive cross-section are determined as described in Sec. VII. A detailed list of the uncertainties is given in Table III.

The binned maximum-likelihood fit yields a cross section of

$$\sigma_t(tq+\bar{t}q) = 68 \pm 2\,(\text{stat.})\ \pm 8\,(\text{syst.})\ \text{pb}$$
$$= 68 \pm 8\,\text{pb},$$

assuming $m_t = 172.5$ GeV. Figure 12(d) compares the measured value for $\sigma(tq+\bar{t}q)$ to NLO predictions [11, 68] obtained with different PDF sets. All predictions are in agreement with the measurement.

B.   Cross-section dependence on the top-quark mass

The t-channel single top-quark cross sections are measured using a signal model with $m_t = 172.5$ GeV. The dependence of the cross-section measurements on m_t is mainly due to acceptance effects and is expressed by the function:

$$\sigma_t = \sigma_t(172.5\,\text{GeV}) + p_1 \cdot \Delta m_t + p_2 \cdot \Delta m_t^2 \qquad (4)$$

with $\Delta m_t = m_t - 172.5$ GeV. The parameters p_1 and p_2 are determined using dedicated signal samples with different m_t and are given in Table IV for $\sigma(tq)$, $\sigma(\bar{t}q)$ and $\sigma(tq+\bar{t}q)$. The cross-section ratio R_t is largely independent of the top-quark mass.

C. V_{tb} extraction

Since $\sigma(tq+\bar{t}q)$ is proportional to $|V_{tb}|^2$, $|V_{tb}|$ can be extracted from the measurement. The $|V_{tb}|$ measurement is independent of assumptions about the number of quark generations and about the unitarity of the CKM matrix. The only assumptions required are that $|V_{tb}| \gg |V_{td}|, |V_{ts}|$ and that the Wtb interaction is an SM-like left-handed weak coupling. The $t\bar{t}$-background rate is unaffected by a variation of $|V_{tb}|$, since the decay to a quark of a potentially existing higher generation are prohibited by kinematics, such that the branching ratio $B(t \to Wb) \sim 1$. On the other hand, the rates of single-top quark Wt and s-channel backgrounds also scale with $|V_{tb}|^2$, but their contributions are small in the signal region. The resulting variation of the total top-quark background yield is less than its systematic uncertainty and thus considered negligible.

The value of $|V_{tb}|^2$ is extracted by dividing the measured value of $\sigma(tq+\bar{t}q)$ by the prediction of the approximate NNLO calculation [9]. The experimental and theoretical uncertainties are added in quadrature. The result obtained is

$$|V_{tb}| = 1.02 \pm 0.01\,(\text{stat.}) \pm 0.06\,(\text{syst.}) \pm 0.02\,(\text{theo.})\,{}^{+0.01}_{-0.00}\,(m_t)$$
$$= 1.02 \pm 0.07.$$

A lower limit on $|V_{tb}|$ is extracted in a Bayesian limit computation, assuming that the likelihood curve of $|V_{tb}|^2$ has a Gaussian shape, centered at the measured value. A flat prior in $|V_{tb}|^2$ is applied, being one in the interval $[0,1]$ and zero otherwise. The resulting lower limit is $|V_{tb}| > 0.88$ at the 95% CL.

IX.   DIFFERENTIAL CROSS-SECTION MEASUREMENTS

Differential cross sections are measured as a function of the p_T and $|y|$ of t and $\bar{t}$ in the 2-jet HPR channels, defined in Sec. VI E.

A.   Signal yield and reconstructed variables

The signal and background composition in the 2-jet-ℓ^+ and the 2-jet-ℓ^- HPR channels can be found in Table V. Figure 13

TABLE III. Detailed list of the contribution of each source of uncertainty to the total uncertainty on the measured values of $\sigma(tq)$, $\sigma(\bar{t}q)$, R_t, and $\sigma(tq+\bar{t}q)$. The evaluation of the systematic uncertainties has a statistical uncertainty of 0.3%. Uncertainties contributing less than 1.0% are marked with "< 1".

Source	$\Delta\sigma(tq)/\sigma(tq)$ [%]	$\Delta\sigma(\bar{t}q)/\sigma(\bar{t}q)$ [%]	$\Delta R_t/R_t$ [%]	$\Delta\sigma(tq+\bar{t}q)/\sigma(tq+\bar{t}q)$ [%]
Data statistical	±3.1	±5.4	±6.2	±2.7
Monte Carlo statistical	±1.9	±3.2	±3.6	±1.9
Multijet normalization	±1.1	±2.0	±1.6	±1.4
Other background normalization	±1.1	±2.8	±1.9	±1.6
JES detector	±1.6	±1.4	< 1	±1.4
JES statistical	< 1	< 1	< 1	< 1
JES physics modeling	< 1	< 1	< 1	< 1
JES η intercalibration	±6.9	±8.4	±1.8	±7.3
JES mixed detector and modeling	< 1	< 1	< 1	< 1
JES close-by jets	< 1	< 1	< 1	< 1
JES pile-up	< 1	< 1	< 1	< 1
JES flavor composition	±1.4	±1.4	±1.2	±1.6
JES flavor response	< 1	< 1	±1.0	< 1
b-JES	< 1	< 1	< 1	< 1
Jet energy resolution	±2.1	±1.6	±1.0	±1.9
Jet vertex fraction	< 1	< 1	< 1	< 1
b-tagging efficiency	±3.8	±4.1	< 1	±3.9
c-tagging efficiency	< 1	±1.4	< 1	< 1
Mistag efficiency	< 1	< 1	< 1	< 1
$b/\bar{b}$ acceptance	±1.0	< 1	< 1	$--$
$E_\mathrm{T}^\mathrm{miss}$ modeling	±2.3	±3.4	±1.6	±2.6
Lepton uncertainties	±2.8	±3.0	±1.0	±2.8
PDF	±3.2	±5.8	±2.5	±3.2
W+jets shape variation	< 1	< 1	< 1	< 1
tq generator + parton shower	±1.9	±1.6	< 1	±1.9
tq scale variations	±2.6	±3.0	< 1	±2.6
$t\bar{t}$ generator + parton shower	< 1	±2.1	±1.6	< 1
$t\bar{t}$ ISR / FSR	< 1	< 1	±1.0	< 1
Luminosity	±1.8	±1.8	±0.5	±1.8
Total systematic	±12.0	±14.9	±6.1	±12.1
Total	±12.4	±15.9	±8.7	±12.4

TABLE IV. Parameterization factors for the m_t dependence (see Eq. (4)) of $\sigma(tq)$, $\sigma(\bar{t}q)$ and $\sigma(tq+\bar{t}q)$.

	p$_1$ [pb/GeV]	p$_2$ [pb/ GeV^2]
$\sigma(tq+\bar{t}q)$	-0.46	-0.06
$\sigma(tq)$	-0.27	-0.04
$\sigma(\bar{t}q)$	-0.19	-0.02

shows the measured distributions of the reconstructed top-quark p_T and the reconstructed top-quark $|y|$ normalized to the result of the binned maximum-likelihood fit performed to measure $\sigma(tq)$ and $\sigma(\bar{t}q)$.

The binning of the differential cross sections is chosen based on the experimental resolution of the p_T and $|y|$ distributions as well as the data statistical uncertainty. Typical values for the resolution of the top-quark p_T are 10 GeV, increas-
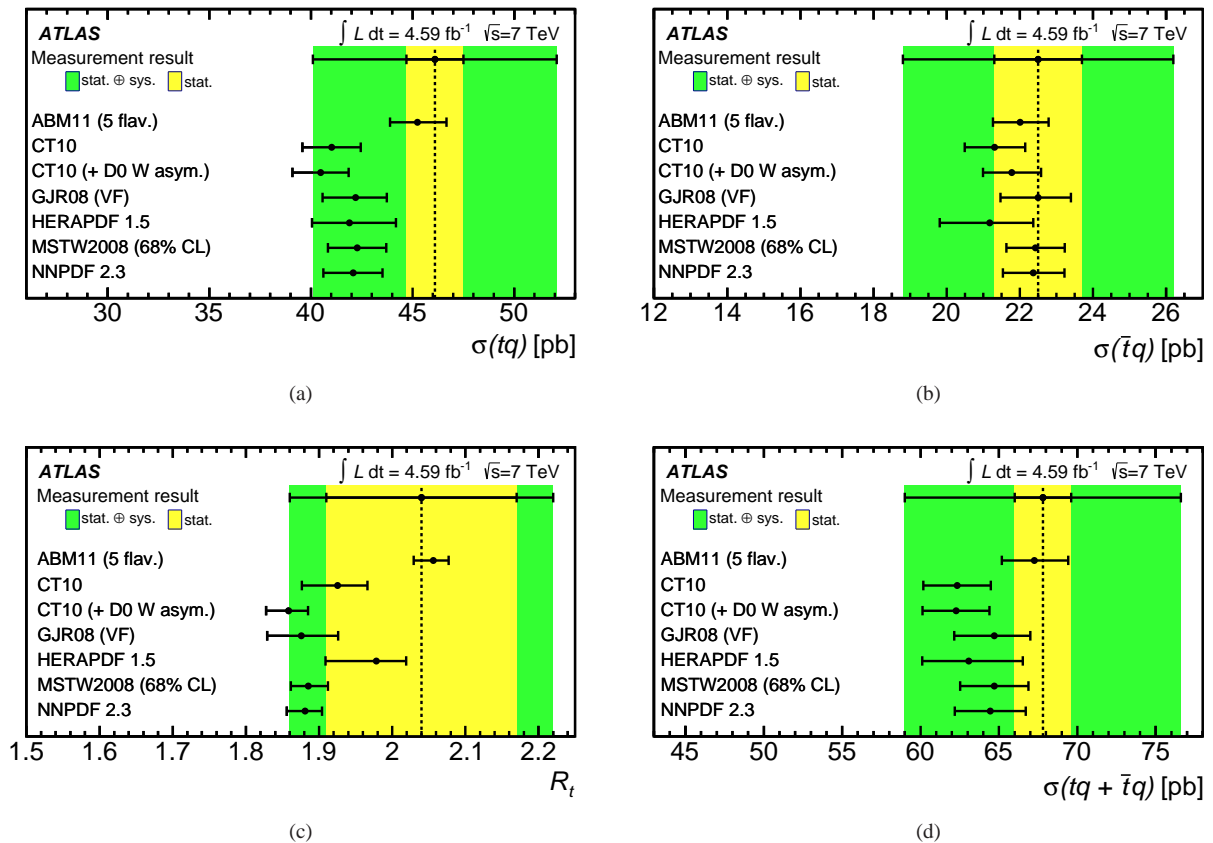
FIG. 12. Comparison between observed and predicted values of (a) $\sigma(tq)$, (b) $\sigma(\bar{t}q)$, (c) R_t, and (d) $\sigma(tq+\bar{t}q)$. The predictions are calculated at NLO precision [11, 68] in the five-flavor scheme and given for different NLO PDF sets and the uncertainty includes the uncertainty on the renormalization and factorization scales, the combined internal PDF and α_s uncertainty. The dotted black line indicates the central value of the measured value. The combined statistical and systematic uncertainty of the measurement is shown in green, while the statistical uncertainty is represented by the yellow error band.

ing to 25 GeV in the tail of the distribution. The resolution of the rapidity varies from 0.2 to 0.4 from central to forward rapidities.

B. Method

The measured distributions are distorted by detector effects and acceptance effects. The observed distributions are unfolded to the (parton level) four-momenta of the top quarks before the decay and after QCD radiation to correct for these distortions. In the following, each bin of the measured distribution is referred to by the index i, while each bin of the parton-level distribution is referred to by the index j. The relation between the measured distribution and the differential cross section in each bin j of the parton-level distribution can be written as:

$$\frac{d\sigma}{dX_j} = \frac{1}{\Delta X_j} \cdot \frac{\sum_i M_{ij}^{-1} \cdot (N_i - B_i)}{\mathcal{L} \cdot \varepsilon_j \cdot B(t \to \ell\nu b)} \quad (5)$$

where ΔX_j is the bin width of the parton-level distribution, N_i (B_i) are the data (expected background) yields in each bin of

TABLE V. Event yields for the 2-jet-ℓ^+ and 2-jet-ℓ^- HPR channels. The expectation for the signal and background yields correspond to the result of the binned maximum-likelihood fit described in Sec. VI D. The uncertainty of the expectations is the normalization uncertainty of each processes after the fit, as described in Sec. VII F.

	2-jet-ℓ^+ HPR	2-jet-ℓ^- HPR
tq	1210 ± 150	1.3 ± 0.2
$\bar{t}q$	0.29 ± 0.05	549 ± 87
$t\bar{t},Wt,t\bar{b},\bar{t}b$	161 ± 18	175 ± 19
$W^++b\bar{b},c\bar{c}$,light jets	250 ± 48	0.35 ± 0.07
$W^-+b\bar{b},c\bar{c}$,light jets	0.7 ± 0.2	166 ± 40
$W+c$	110 ± 26	125 ± 30
Z+jets, diboson	15 ± 10	11.4 ± 6.8
Multijet	59 ± 30	62 ± 31
Total expectation	1810 ± 160	1090 ± 110
Data	1813	1034
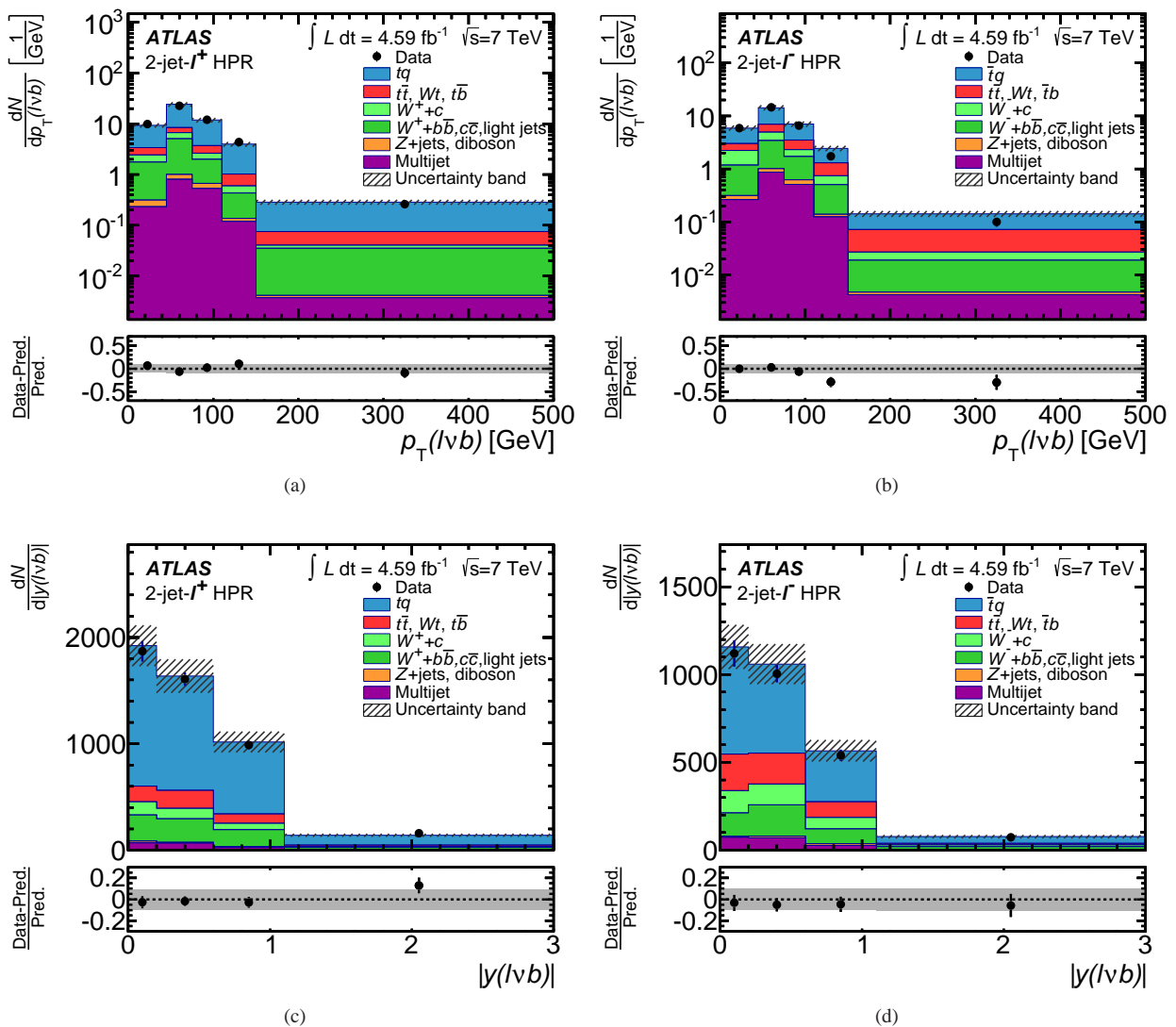
FIG. 13. Measured distributions of (a) the top-quark p_T, (b) top-antiquark p_T, (c) top-quark $|y|$, and (d) top-antiquark $|y|$ shown on reconstruction level in the HPR normalized to the result of the binned maximum-likelihood fit. The uncertainty band represents the normalization uncertainty of all processes after the fit and the Monte Carlo statistical uncertainty, added in quadrature. The relative difference between the observed and expected number of events in each bin is shown in the lower panels.

the measured distribution, $\mathscr{L}$ is the integrated luminosity of the data sample, ε_j is the event selection efficiency and M_{ij}^{-1} is the inverse of the migration matrix. The migration matrix accounts for the detector response and is defined as the probability to observe an event in bin i when it is generated in bin j. The migration matrix is built by relating the variables at the reconstruction and at the parton level using the signal simulation. Figure 14 shows the migration matrices for the p_T and $|y|$ distributions of the top quark and top antiquark. The inverse of the matrix is determined by applying Bayes' theorem iteratively [69] in order to perform the unfolding. The number of iterations is chosen such that the absolute change in the unfolded distributions is on average smaller than 1% of the content in each bin. This procedure results in a total of five iterations for all distributions. The selection efficiency ε_j in

bin j of each variable is defined as the ratio of the parton-level yield before and after selection and is evaluated using simulation. The efficiencies are typically in the 0.5–2.2% range.

The unfolding is applied to the reconstructed $p_T(\ell\nu b)$ and $|y(\ell\nu b)|$ distributions after subtraction of the background contributions. When subtracting the background, all backgrounds are normalized according to Table V.

Closure tests are performed in order to check the validity of the unfolding procedure. The shape of the parton-level distributions in the Monte Carlo simulation are altered to verify that the simulation does not bias the results. It is checked that the altered parton-level distributions are recovered by unfolding the reconstructed distributions with the nominal migration matrix.
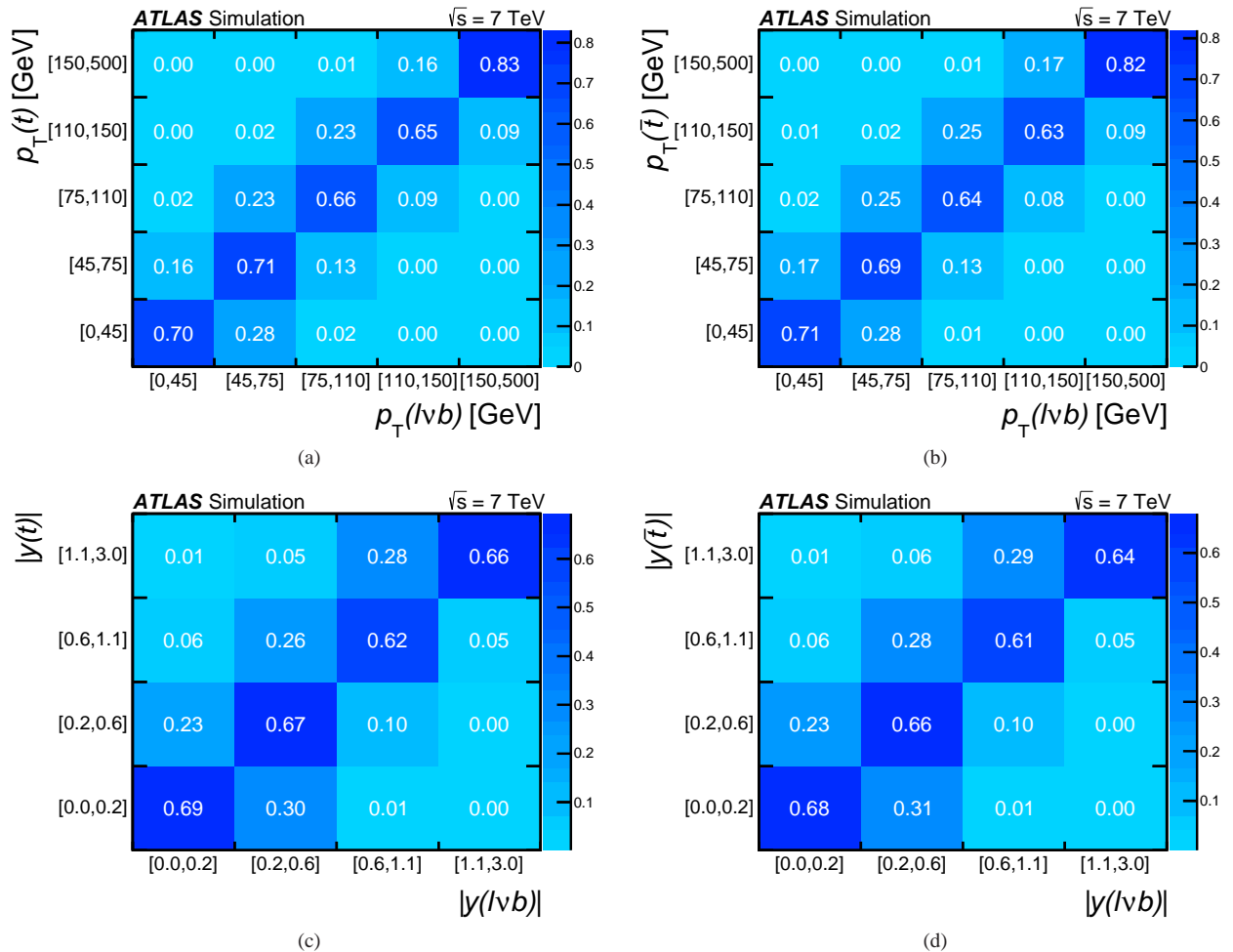
FIG. 14. Migration matrices relating the parton level shown on the *y* axis and reconstruction level shown on the *x* axis for the (a) top-quark p_T, (b) top-antiquark p_T, (c) top-quark $|y|$, and (d) top-antiquark $|y|$ distribution.

C. Treatment of uncertainties

The statistical uncertainty of the unfolded results is estimated using pseudo-experiments, propagating the uncertainties from the measured distribution and from the size of the Monte Carlo signal and background samples through the unfolding process. All sources of systematic uncertainty described in Sec. VII are included for the unfolded distributions. In the case of the background normalization, the uncertainties quoted in Table V are taken into account. The impact of the systematic uncertainties is evaluated by modifying the subtracted background before unfolding in the case of uncertainties on the backgrounds. To assign uncertainties on the signal modeling, systematic shifts are applied to the simulated signal sample. The shifted reconstructed distribution is unfolded and then compared to the nominal distribution at parton level.

D. Results

To reduce the impact of systematic uncertainties normalized differential cross sections $1/\sigma \cdot (d\sigma/dX_j)$ are calculated by dividing the differential cross section by the total cross section evaluated by integrating over all bins.

The absolute differential cross-section results are listed in Table VI and the normalized resutls in Table VII as a function of p_T and $|y|$ of the top quark. A graphical representation of the results is shown in Fig. 15 for the absolute cross sections and in Fig. 16 for the normalized case. They are compared to NLO predictions from MCFM [46] using the MSTW2008 PDF set for all variables. Uncertainties on the predicted values include the uncertainty on the scale and the PDF. To compare the NLO prediction with the measurement, χ^2 values are computed with HERAfitter [70, 71] taking into account the full correlation of the systematic and statistical uncertainties. The χ^2 values for the differential cross sections are listed in Table VIII.

Systematic uncertainties dominate over the statistical uncertainty for the differential cross sections. Large uncertain-

ties originate from the background normalization, the *tq* generator + parton shower uncertainty, the JES due to the uncertainty in the η intercalibration as well as the PDF uncertainties mainly in the top-antiquark distributions. A detailed list of the systematic contributions in each bin of each distributions is shown in Table IX for $d\sigma/dp_{\mathrm{T}}(t)$, in Table X for $d\sigma/dp_{\mathrm{T}}(\bar{t})$, in Table XI for $d\sigma/d|y(t)|$, and in Table XII for $d\sigma/d|y(\bar{t})|$. In the case of the normalized differential cross sections many systematic uncertainties cancel and thus the measurement is dominated by statistical uncertainties from the data distributions and the Monte Carlo sample size. The contribution of systematic uncertainties to the normalized distribution is again dominated by the background normalization, *tq* generator + parton shower, and the JES η-intercalibration uncertainty. Details of the contribution of each systematic uncertainty in each bin of the normalized distributions are listed in Table XIII for $1/\sigma \cdot d\sigma/dp_{\mathrm{T}}(t)$, in Table XIV for $1/\sigma \cdot d\sigma/dp_{\mathrm{T}}(\bar{t})$, in Table XV for $1/\sigma \cdot d\sigma/d|y(t)|$, and in Table XVI for $1/\sigma \cdot d\sigma/d|y(\bar{t})|$. Bin-wise correlation matrices for the statistical uncertainty are given in Fig. 17 for the differential cross sections and in Fig. 18 for the normalized differential cross sections.

Overall, good agreement is observed between the NLO QCD predictions and the differential cross-section measurements. This is also supported by the χ^2 values listed in Table VIII.

X. CONCLUSIONS

In summary, measurements of the single top-quark production cross sections, $\sigma(tq)$, $\sigma(\bar{t}q)$, R_t, and $\sigma(tq+\bar{t}q)$, with the ATLAS detector at the LHC are presented using an integrated luminosity of 4.59 fb^{-1} pp collision data at $\sqrt{s} = 7$ TeV. All measurements are based on neural network (NN) discriminants separating signal events from background events. Binned maximum-likelihood fits to the NN discriminants yield: $\sigma(tq) = 46 \pm 6$ pb, $\sigma(\bar{t}q) = 23 \pm 4$ pb, and $\sigma(tq+\bar{t}q) = 68 \pm 8$ pb. The measured cross-section ratio is $R_t = 2.04 \pm 0.18$. The corresponding coupling at the *Wtb* vertex is $|V_{tb}| = 1.02 \pm 0.07$, and the 95% CL lower limit on the CKM matrix element $|V_{tb}|$ is 0.88. A high-purity region is defined using the signal region of the NN discriminant for the differential cross-section measurements. Using an iterative Bayesian method, differential cross sections are extracted as a function of $p_{\mathrm{T}}(t)$, $p_{\mathrm{T}}(\bar{t})$, $|y(t)|$, and $|y(\bar{t})|$. Good agreement with the NLO QCD predictions is observed.

ACKNOWLEDGEMENTS

FIG. 15. Differential cross section as a function of (a) $p_T(t)$, (b) $p_T(\bar{t})$, (c) $|y(t)|$ and (d) $|y(\bar{t})|$. The differential distributions are compared to the QCD NLO calculation. The black vertical error bars on the data points denote the total combined uncertainty, the green error bars denote the statistical uncertainty, while the red band denotes the theory predictions calculated at NLO using MCFM [46]. Uncertainties on the predicted values include the PDF and scale uncertainties. The horizontal error bars indicate the bin width.
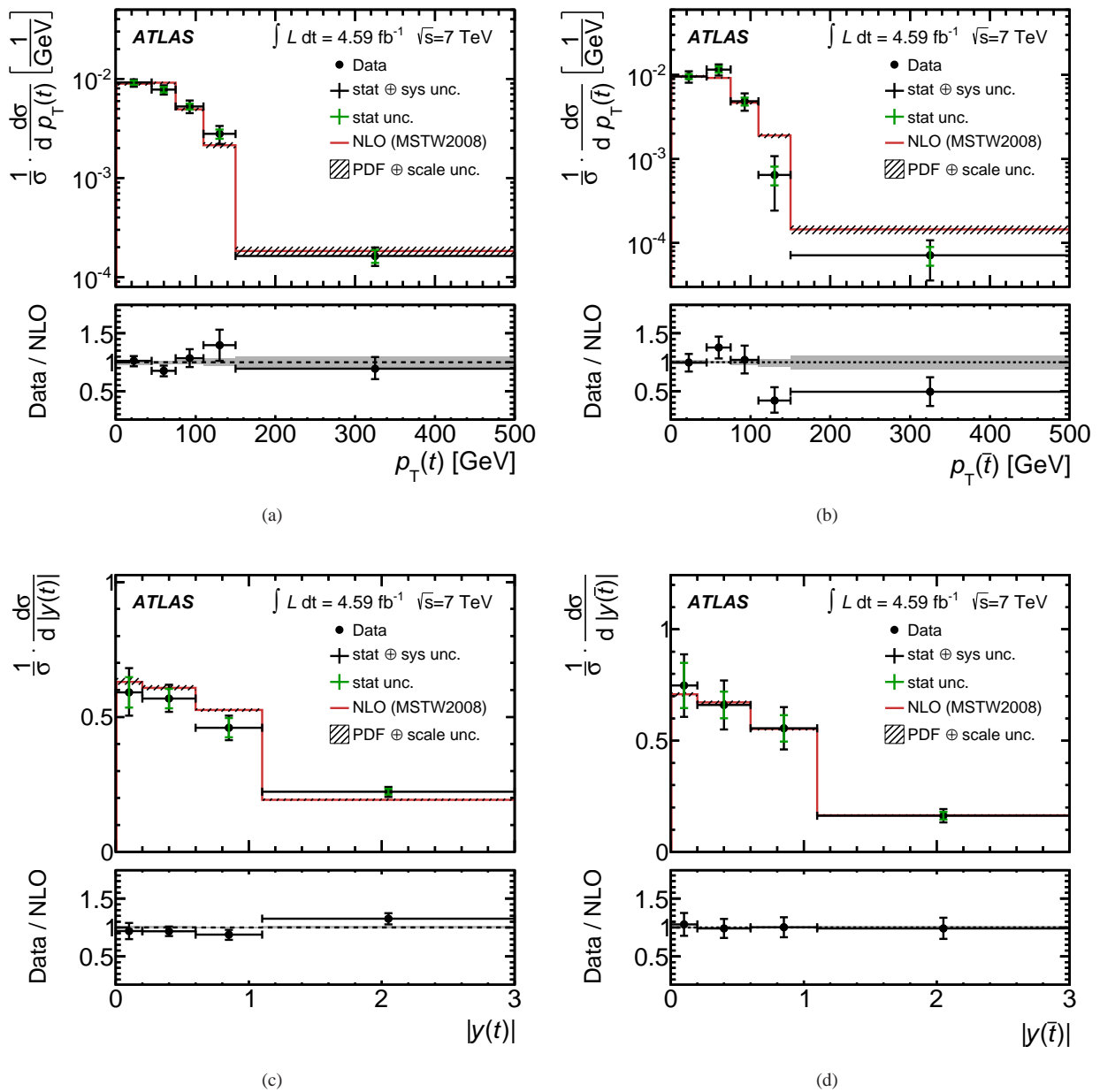
FIG. 16. Normalized differential cross section as a function of (a) $p_T(t)$, (b) $p_T(\bar{t})$, (c) $|y(t)|$ and (d) $|y(\bar{t})|$. The normalized differential distributions are compared to the QCD NLO calculation. The black vertical error bars on the data points denote the total combined uncertainty, the green error bars denote the statistical uncertainty, while the red band denotes the theory predictions calculated at NLO using MCFM [46]. Uncertainties on the predicted values include the PDF and scale uncertainties. The horizontal error bars indicate the bin width.
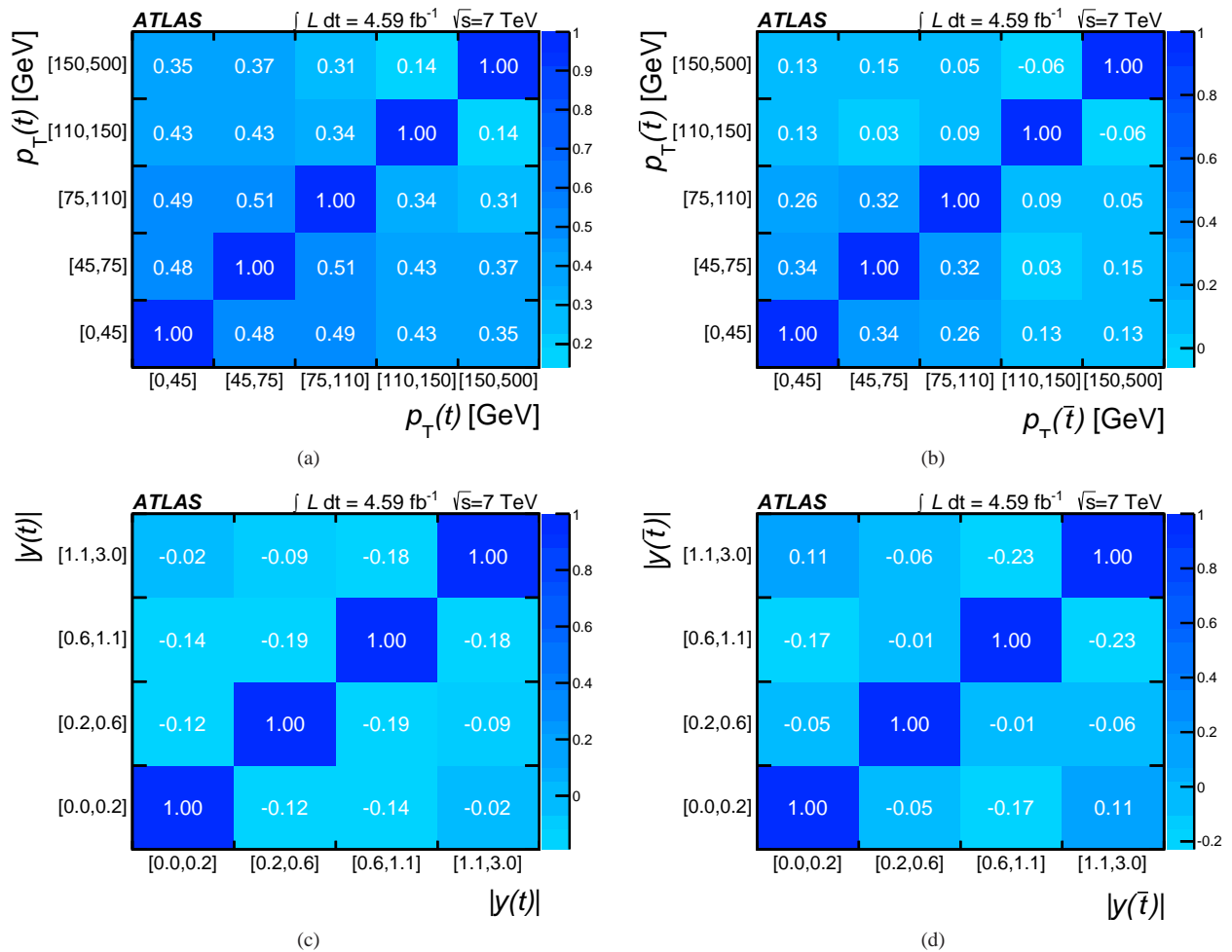
FIG. 17. Statistical correlation matrices for the differential cross section as a function of (a) $p_T(t)$, (b) $p_T(\bar{t})$, (c) $|y(t)|$ and (d) $|y(\bar{t})|$.
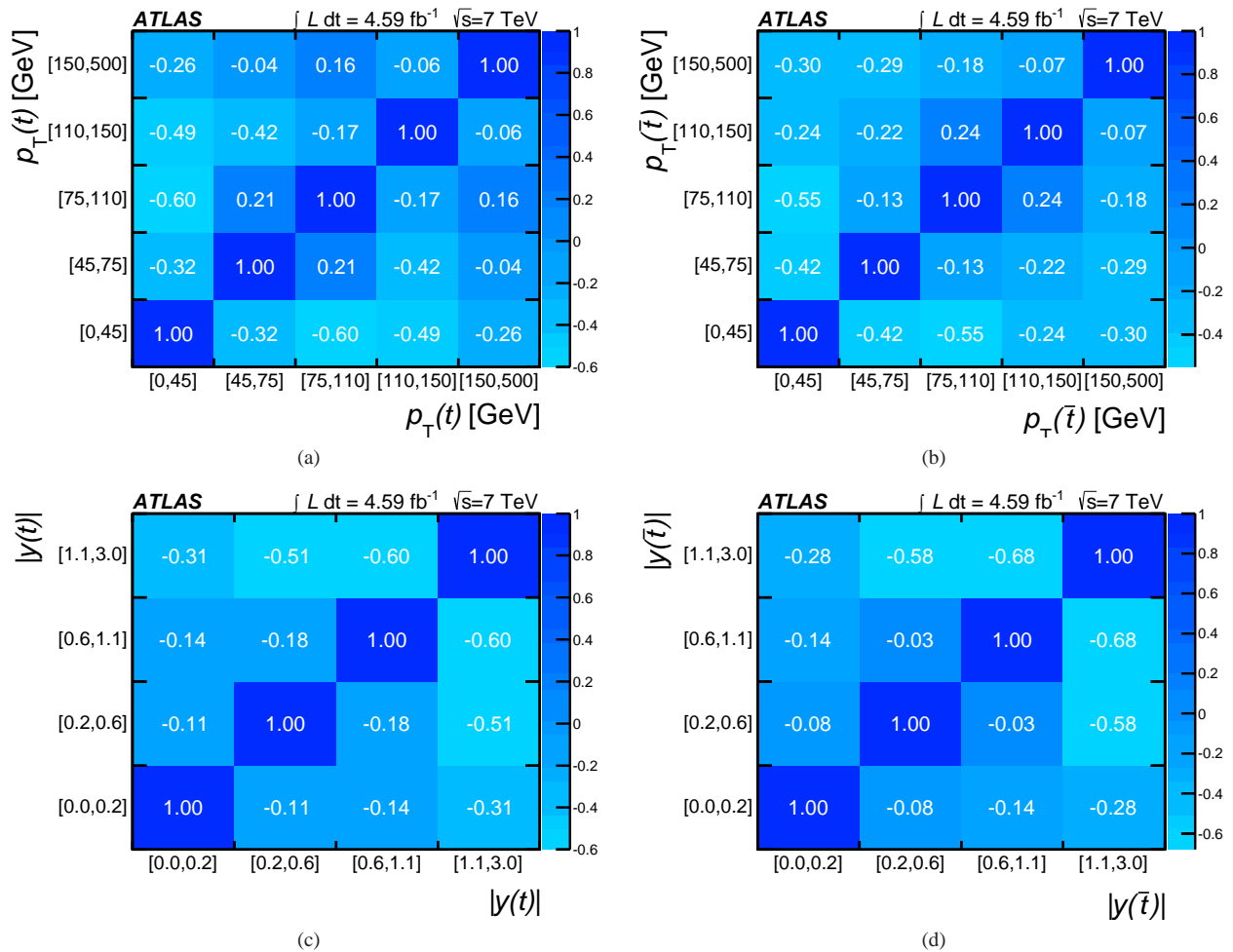
FIG. 18. Statistical correlation matrices for the normalized differential cross section as a function of (a) $p_{\mathrm{T}}(t)$, (b) $p_{\mathrm{T}}(\bar{t})$, (c) $|y(t)|$ and (d) $|y(\bar{t})|$.

TABLE VI. Differential t-channel top-quark production cross section as a function of $p_{\mathrm{T}}(t)$, $p_{\mathrm{T}}(\bar{t})$, $|y(t)|$ and $|y(\bar{t})|$ with the uncertainties for each bin given in percent.

$p_{\mathrm{T}}(t)$ [GeV]	$\frac{d\sigma}{dp_{\mathrm{T}}(t)}\left[\frac{\mathrm{fb}}{\mathrm{GeV}}\right]$	total [%]	stat. [%]	syst. [%]
$[0,45]$	440 ± 70	±15	±7.4	±13
$[45,75]$	370 ± 60	±16	±6.5	±14
$[75,110]$	250 ± 40	±15	±7.7	±13
$[110,150]$	133 ± 27	±20	±12	±16
$[150,500]$	7.8 ± 1.9	±24	±16	±19

$p_{\mathrm{T}}(\bar{t})$ [GeV]	$\frac{d\sigma}{dp_{\mathrm{T}}(\bar{t})}\left[\frac{\mathrm{fb}}{\mathrm{GeV}}\right]$	total [%]	stat. [%]	syst. [%]
$[0,45]$	190 ± 50	±28	±12	±25
$[45,75]$	230 ± 40	±18	±8.2	±17
$[75,110]$	97 ± 27	±27	±13	±24
$[110,150]$	13.0 ± 9.7	±74	±26	±70
$[150,500]$	1.4 ± 0.9	±59	±26	±53

$|y(t)|$	$\frac{d\sigma}{d|y(t)|}$ [pb]	total [%]	stat. [%]	syst. [%]
$[0,0.2]$	28 ± 4	±15	±9.0	±12
$[0.2,0.6]$	27.3 ± 3.3	±12	±6.3	±10
$[0.6,1.1]$	22.1 ± 3.0	±14	±7.5	±11
$[1.1,3.0]$	10.7 ± 1.6	±15	±7.0	±13

$|y(\bar{t})|$	$\frac{d\sigma}{d|y(\bar{t})|}$ [pb]	total [%]	stat. [%]	syst. [%]
$[0,0.2]$	15.0 ± 3.4	±23	±13	±18
$[0.2,0.6]$	13.3 ± 3.3	±25	±9.5	±23
$[0.6,1.1]$	11.2 ± 2.6	±23	±11	±20
$[1.1,3.0]$	3.3 ± 0.9	±29	±13	±25

TABLE VII. Normalized differential t-channel top-quark production cross section as a function of $p_{\mathrm{T}}(t)$, $p_{\mathrm{T}}(\bar{t})$, $|y(t)|$ and $|y(\bar{t})|$ with the uncertainties for each bin given in percent.

$p_{\mathrm{T}}(t)$ [GeV]	$\frac{1}{\sigma}\frac{d\sigma}{dp_{\mathrm{T}}(t)}\left[\frac{10^{-3}}{\mathrm{GeV}}\right]$	total [%]	stat. [%]	syst. [%]
$[0,45]$	$9.2^{+0.8}_{-0.9}$	$^{+8.4}_{-9.4}$	±5.3	$^{+6.5}_{-7.7}$
$[45,75]$	7.8 ± 0.9	±11	±6.9	±8.8
$[75,110]$	5.3 ± 0.8	±15	±8.0	±13
$[110,150]$	2.8 ± 0.6	±21	±11	±18
$[150,500]$	0.16 ± 0.04	±22	±15	±16

$p_{\mathrm{T}}(\bar{t})$ [GeV]	$\frac{1}{\sigma}\frac{d\sigma}{dp_{\mathrm{T}}(\bar{t})}\left[\frac{10^{-3}}{\mathrm{GeV}}\right]$	total [%]	stat. [%]	syst. [%]
$[0,45]$	9.6 ± 1.6	±17	±8.2	±15
$[45,75]$	11.6 ± 1.8	±15	±8.8	±12
$[75,110]$	4.9 ± 1.2	±25	±13	±21
$[110,150]$	0.7 ± 0.4	$^{+67}_{-61}$	±25.8	$^{+62}_{-56}$
$[150,500]$	0.07 ± 0.04	±51	±26	±45

$|y(t)|$	$\frac{1}{\sigma}\frac{d\sigma}{d|y(t)|}$	total [%]	stat. [%]	syst. [%]
$[0,0.2]$	0.59 ± 0.09	±15	±9.0	±11
$[0.2,0.6]$	0.57 ± 0.05	±9.0	±6.4	±6.3
$[0.6,1.1]$	0.46 ± 0.05	±9.7	±7.5	±6.2
$[1.1,3.0]$	0.223 ± 0.019	±8.5	±4.9	±6.9

$|y(\bar{t})|$	$\frac{1}{\sigma}\frac{d\sigma}{d|y(\bar{t})|}$	total [%]	stat. [%]	syst. [%]
$[0,0.2]$	0.75 ± 0.14	±19	±13	±13
$[0.2,0.6]$	0.66 ± 0.11	±17	±9.1	±14
$[0.6,1.1]$	0.555 ± 0.095	±17	±11	±13
$[1.1,3.0]$	0.163 ± 0.030	±18	±11	±15

TABLE VIII. Comparison between the measured differential cross sections and the predictions from the NLO calculation using the MSTW2008 PDF set. For each variable and prediction a χ^2 value is calculated with HERAfitter using the covariance matrix of each measured spectrum. The theory uncertainties of the predictions are treated as uncorrelated. The number of degrees of freedom (NDF) is equal to the number of bins in the measured spectrum.

	$\frac{d\sigma}{dp_{\mathrm{T}}(t)}$	$\frac{d\sigma}{dp_{\mathrm{T}}(\bar{t})}$	$\frac{d\sigma}{d|y(t)|}$	$\frac{d\sigma}{d|y(\bar{t})|}$
χ^2/NDF	7.55/5	4.68/5	6.30/4	0.32/4

TABLE IX. Detailed list of the contribution of each source of uncertainty to the total relative uncertainty on the measured $\frac{d\sigma}{dp_{\mathrm{T}}(t)}$ distribution given in percent for each bin. The list includes only those uncertainties that contribute with more than 1%. The following uncertainties contribute to the total uncertainty with less than 1% to each bin content: JES detector, JES statistical, JES physics modeling, JES mixed detector and modeling, JES close-by jets, JES pile-up, JES flavor composition, JES flavor response, jet vertex fraction, $b/\bar{b}$ acceptance, $E_{\mathrm{T}}^{\mathrm{miss}}$ modeling, W+jets shape variation, and $t\bar{t}$ generator.

$\frac{d\sigma}{dp_{\mathrm{T}}(t)}$	$p_{\mathrm{T}}(t)$ bins [GeV]				
Source	$[0,45]$	$[45,75]$	$[75,110]$	$[110,150]$	$[150,500]$
Data statistical	±7.4	±6.5	±7.7	±12	±16
Monte Carlo statistical	±5.5	±5.3	±4.8	±6.0	±9.4
Background normalization	±6.1	±7.5	±5.2	±3.0	±5.2
JES η intercalibration	<1	$+2.6/-1.3$	$+3.4/-1.9$	<1	$+9.0/-4.2$
b-JES	<1	$+1.2/-2.3$	<1	±1.6	<1
Jet energy resolution	±1.0	±2.4	±2.3	±3.0	<1
b-tagging efficiency	±3.0	±3.1	±3.3	±3.6	±6.2
c-tagging efficiency	±1.3	±1.5	<1	<1	<1
Mistag efficiency	±2.0	±1.9	<1	<1	±1.2
Lepton uncertainties	±2.6	±2.6	±2.6	±2.6	±2.6
PDF	±3.0	±1.8	±2.3	±2.8	±2.4
tq generator + parton shower	±6.8	±8.2	∓7.9	∓12	$+9.2/-9.7$
tq scale variation	±2.8	<1	±3.7	<1	$+6.0/-6.4$
Unfolding	±1.3	±1.4	<1	<1	<1
Luminosity	±1.8	±1.8	±1.8	±1.8	±1.8
Total systematic	±13	±14	±13	±16	±19
Total	±15	±16	±15	±20	±25

TABLE X. Detailed list of the contribution of each source of uncertainty to the total relative uncertainty on the measured $\frac{d\sigma}{dp_{\mathrm{T}}(\bar{t})}$ distribution given in percent for each bin. The list includes only those uncertainties that contribute with more than 1%. The following uncertainties contribute to the total uncertainty with less than 1% to each bin content: JES detector, JES statistical, JES physics modeling, JES mixed detector and modeling, JES close-by jets, JES pile-up, JES flavor composition, JES flavor response, b-JES, jet vertex fraction, mistag efficiency, $b/\bar{b}$ acceptance, $E_{\mathrm{T}}^{\mathrm{miss}}$ modeling, W+jets shape variation, and $t\bar{t}$ generator.

$\frac{d\sigma}{dp_{\mathrm{T}}(\bar{t})}$	$p_{\mathrm{T}}(\bar{t})$ bins [GeV]				
Source	$[0, 45]$	$[45, 75]$	$[75, 110]$	$[110, 150]$	$[150, 500]$
Data statistical	± 12	± 8.2	± 13	± 26	± 26
Monte Carlo statistical	± 12	± 9.1	± 14	± 28	± 28
Background normalization	± 14	± 11	± 16	± 48	± 33
JES η intercalibration	$-9.0/+8.7$	$+1.9/-3.7$	$+4.9/-1.3$	$+15/-13$	< 1
Jet energy resolution	± 1.0	± 2.2	± 3.4	< 1	± 3.0
b-tagging efficiency	± 3.0	± 3.1	± 3.2	± 3.6	± 5.9
c-tagging efficiency	± 5.6	± 2.0	± 2.2	± 10	± 5.9
Lepton uncertainties	± 2.6	± 2.6	± 2.6	± 2.6	± 2.7
PDF	± 3.8	± 4.3	± 5.3	± 7.2	± 8.2
tq generator + parton shower	± 12.2	< 1	∓ 9.6	± 11	< 1
tq scale variation	± 3.1	< 1	± 3.2	± 1.9	± 5.9
Unfolding	< 1	< 1	< 1	± 6.9	± 2.6
Luminosity	± 1.8	± 1.8	± 1.8	± 1.8	± 1.8
Total systematic	± 25	± 17	± 24	± 70	± 53
Total	± 27	± 18	± 27	± 74	± 59

TABLE XI. Detailed list of the contribution of each source of uncertainty to the total relative uncertainty on the measured $\frac{d\sigma}{d|y(t)|}$ distribution given in percent for each bin. The list includes only those uncertainties that contribute with more than 1%. The following uncertainties contribute to the total uncertainty with less than 1% to each bin content: JES detector, JES statistical, JES physics modeling, JES mixed detector and modeling, JES close-by jets, JES pile-up, JES flavor composition, JES flavor response, jet vertex fraction, $b/\bar{b}$ acceptance, $E_\mathrm{T}^\mathrm{miss}$ modeling, W+jets shape variation, $t\bar{t}$ generator, $t\bar{t}$ ISR/FSR, and unfolding.

$\frac{d\sigma}{d|y(t)|}$	$|y(t)|$ bins			
Source	$[0, 0.2]$	$[0.2, 0.6]$	$[0.6, 1.1]$	$[1.1, 3.0]$
Data statistical	± 9.0	± 6.3	± 7.5	± 7.1
Monte Carlo statistical	± 5.9	± 4.8	± 5.0	± 4.4
Background normalization	± 5.3	± 6.5	± 6.7	± 4.7
JES η intercalibration	$+1.7/-0.6$	< 1	$+1.7/-0.4$	< 1
b-JES	$+1.1/-1.7$	< 1	$+1.1/+0.2$	< 1
Jet energy resolution	± 3.2	± 1.7	< 1	± 3.1
b-tagging efficiency	± 3.3	± 3.4	± 3.4	± 3.2
c-tagging efficiency	± 1.3	± 1.2	± 1.2	± 1.0
Mistag efficiency	< 1	± 1.3	± 2.0	± 1.4
Lepton uncertainties	± 2.6	± 2.7	± 2.6	± 2.5
PDF	± 3.6	± 3.6	± 2.8	± 2.8
tq generator + parton shower	∓ 5.7	± 0.8	± 4.0	± 8.7
tq scale variation	± 3.5	< 1	± 2.6	± 4.7
Luminosity	± 1.8	± 1.8	± 1.8	± 1.8
Total systematic	± 12	± 10	± 11	± 14
Total	± 15	± 12	± 14	± 15

TABLE XII. Detailed list of the contribution of each source of uncertainty to the total relative uncertainty on the measured $\frac{d\sigma}{d|y(\bar{t})|}$ distribution given in percent for each bin. The list includes only those uncertainties that contribute with more than 1%. The following uncertainties contribute to the total uncertainty with less than 1% to each bin content: JES detector, JES statistical, JES physics modeling, JES mixed detector and modeling, JES close-by jets, JES pile-up, JES flavor composition, JES flavor response, b-JES, jet vertex fraction, $b/\bar{b}$ acceptance, mistag efficiency, $E_{\mathrm{T}}^{\mathrm{miss}}$ modeling, W+jets shape variation, $t\bar{t}$ generator, $t\bar{t}$ ISR/FSR, and unfolding.

$\frac{d\sigma}{d|y(\bar{t})|}$	$|y(\bar{t})|$ bins			
Source	$[0, 0.2]$	$[0.2, 0.6]$	$[0.6, 1.1]$	$[1.1, 3.0]$
Data statistical	± 13	± 9.5	± 11	± 13
Monte Carlo statistical	± 11	± 12	± 11	± 17
Background normalization	± 11	± 16	± 13	± 15
JES η intercalibration	< 1	$+1.0/-1.8$	< 1	$+2.3/-0.9$
Jet energy resolution	± 2.3	± 2.2	± 1.0	± 3.2
b-tagging efficiency	± 3.4	± 3.3	± 3.2	± 3.2
c-tagging efficiency	± 2.5	± 3.6	± 2.9	± 4.0
Lepton uncertainties	± 2.7	± 2.7	± 2.6	± 2.4
PDF	± 6.0	± 5.3	± 4.4	± 4.1
tq generator + parton shower	± 1.0	∓ 5.6	± 6.6	± 6.2
tq scale variation	± 2.1	± 2.6	± 1.6	± 4.3
Luminosity	± 1.8	± 1.8	± 1.8	± 1.8
Total systematic	± 18	± 23	± 20	± 25
Total	± 23	± 25	± 23	± 29

TABLE XIII. Detailed list of the contribution of each source of uncertainty to the total relative uncertainty on the measured $\frac{1}{\sigma}\frac{d\sigma}{dp_{\mathrm{T}}(t)}$ distribution given in percent for each bin. The list includes only those uncertainties that contribute with more than 1%. The JES η intercalibration uncertainty has a sign switch from the first to the second bin. For the tq generator + parton shower uncertainty a sign switch is denoted with $\mp$. The following uncertainties contribute to the total uncertainty with less than 1% to each bin content: JES detector, JES statistical, JES physics modeling, JES mixed detector and modeling, JES close-by jets, JES pile-up, JES flavor composition, JES flavor response, b-JES, jet vertex fraction, $b/\bar{b}$ acceptance, c-tagging efficiency, $E_{\mathrm{T}}^{\mathrm{miss}}$ modeling, lepton uncertainties, W+jets shape variation, and $t\bar{t}$ generator.

$\frac{1}{\sigma}\frac{d\sigma}{dp_{\mathrm{T}}(t)}$	$p_{\mathrm{T}}(t)$ bins [GeV]				
Source	$[0,45]$	$[45,75]$	$[75,110]$	$[110,150]$	$[150,500]$
Data statistical	± 5.3	± 6.9	± 8.0	± 11	± 15
Monte Carlo statistical	± 4.2	± 5.5	± 5.2	± 6.2	± 9.3
Background normalization	< 1	± 1.7	< 1	± 3.0	< 1
JES η intercalibration	$-4.7/+1.5$	$+3.5/-2.3$	$+4.1/-0.8$	< 1	$+9.6/-3.1$
Jet energy resolution	< 1	< 1	< 1	∓ 1.4	± 2.7
b-tagging efficiency	< 1	< 1	< 1	< 1	± 2.8
Mistag efficiency	< 1	< 1	< 1	± 1.0	< 1
tq generator + parton shower	± 3.9	± 5.4	∓ 11	∓ 14	± 6.9
tq scale variation	< 1	∓ 1.8	± 1.3	∓ 2.7	$+4.4/-5.1$
Unfolding	< 1	± 1.7	< 1	< 1	± 1.1
Total systematic	$+6.5/-7.7$	± 8.8	± 13	± 18	± 16
Total	$+8.4/-9.4$	± 11	± 15	± 21	± 22

TABLE XIV. Detailed list of the contribution of each source of uncertainty to the total relative uncertainty on the measured $\frac{1}{\sigma}\frac{d\sigma}{dp_{\mathrm{T}}(\bar{t})}$ distribution given in percent for each bin. The list includes only those uncertainties that contribute with more than 1%. Sign switches within one uncertainty are denoted with $\mp$ and $\pm$. The following uncertainties contribute to the total uncertainty with less than 1% to each bin content: JES detector, JES statistical, JES physics modeling, JES mixed detector and modeling, JES close-by jets, JES pile-up, JES flavor composition, JES flavor response, b-JES, jet vertex fraction, $b/\bar{b}$ acceptance, mistag efficiency, $E_{\mathrm{T}}^{\mathrm{miss}}$ modeling, lepton uncertainties, W+jets shape variation, and $t\bar{t}$ generator.

$\frac{1}{\sigma}\frac{d\sigma}{dp_{\mathrm{T}}(\bar{t})}$	$p_{\mathrm{T}}(\bar{t})$ bins [GeV]				
Source	[0,45]	[45,75]	[75,110]	[110,150]	[150,500]
Data statistical	± 8.2	± 8.8	± 13	± 26	± 26
Monte Carlo statistical	± 8.7	± 9.6	± 14	± 28	± 27
Background normalization	< 1	± 4.5	± 1.8	± 39	± 22
JES η intercalibration	$-7.5/+6.7$	$+3.8/-5.3$	$+6.9/-3.1$	$+17/-9.9$	< 1
Jet energy resolution	< 1	< 1	∓ 1.6	± 1.8	∓ 1.2
b-tagging efficiency	< 1	< 1	< 1	< 1	$+2.4/-2.8$
c-tagging efficiency	∓ 1.8	± 2.0	± 1.7	$-6.2/+5.9$	∓ 2.0
PDF	< 1	< 1	< 1	± 2.5	± 3.6
tq generator + parton shower	$+7.7/-8.2$	$-3.6/+3.7$	$-13/+14$	$+6.4/-7.0$	$-4.2/+4.5$
tq scale variation	± 1.3	∓ 3.0	± 1.4	∓ 1.8	± 5.1
Unfolding	< 1	< 1	< 1	± 6.7	± 2.8
Total systematic	± 15	± 13	± 21	$+62/-56$	± 45
Total	± 17	± 15	± 25	$+67/-61$	± 52

TABLE XV. Detailed list of the contribution of each source of uncertainty to the total relative uncertainty on the measured $\frac{1}{\sigma}\frac{d\sigma}{d|y(t)|}$ distribution given in percent for each bin. The list includes only those uncertainties that contribute with more than 1%. Sign switches within one uncertainty are denoted with $\mp$ and $\pm$. The following uncertainties contribute to the total uncertainty with less than 1% to each bin content: JES detector, JES statistical, JES physics modeling, JES mixed detector and modeling, JES close-by jets, JES pile-up, JES flavor composition, JES flavor response, b-JES, jet vertex fraction, $b/\bar{b}$ acceptance, b-tagging efficiency, c-tagging efficiency, mistag efficiency, $E_{\mathrm{T}}^{\mathrm{miss}}$ modeling, lepton uncertainties, W+jets shape variation, $t\bar{t}$ generator, $t\bar{t}$ ISR/FSR, and unfolding.

$\frac{1}{\sigma}\frac{d\sigma}{d|y(t)|}$	$|y(t)|$ bins			
Source	$[0, 0.2]$	$[0.2, 0.6]$	$[0.6, 1.1]$	$[1.1, 3.0]$
Data statistical	± 9.0	± 6.4	± 7.5	± 5.0
Monte Carlo statistical	± 5.9	± 4.8	± 4.9	± 3.2
Background normalization	< 1	< 1	± 1.1	± 1.0
JES η intercalibration	$+1.6/-1.5$	$-0.5/+2.3$	$+1.4/-1.5$	< 1
Jet energy resolution	± 1.2	< 1	∓ 1.6	± 1.0
PDF	± 1.7	± 1.8	< 1	± 2.3
tq generator + parton shower	$-9.0/+9.8$	$-2.8/+3.0$	< 1	$+4.8/-5.2$
tq scale variation	< 1	< 1	< 1	± 1.5
Total systematic	± 11	± 6.3	± 6.2	± 6.9
Total	± 15	± 9.0	± 9.7	± 8.5

TABLE XVI. Detailed list of the contribution of each source of uncertainty to the total relative uncertainty on the measured $\frac{1}{\sigma}\frac{d\sigma}{d|y(\bar{t})|}$ distribution given in percent for each bin. The list includes only those uncertainties that contribute with more than 1%. Sign switches within one uncertainty are denoted with $\mp$ and $\pm$. The following uncertainties contribute to the total uncertainty with less than 1% to each bin content: JES detector, JES statistical, JES physics modeling, JES mixed detector and modeling, JES close-by jets, JES pile-up, JES flavor composition, JES flavor response, b-JES, jet energy resolution, jet vertex fraction, $b/\bar{b}$ acceptance, b-tagging efficiency, c-tagging efficiency, mistag efficiency, $E_{\mathrm{T}}^{\mathrm{miss}}$ modeling, lepton uncertainties, W+jets shape variation, $t\bar{t}$ generator, $t\bar{t}$ ISR/FSR, and unfolding.

$\frac{1}{\sigma}\frac{d\sigma}{d|y(\bar{t})|}$	$|y(\bar{t})|$ bins			
Source	$[0, 0.2]$	$[0.2, 0.6]$	$[0.6, 1.1]$	$[1.1, 3.0]$
Data statistical	± 13	± 9.1	± 11	± 11
Monte Carlo statistical	± 12	± 11	± 12	± 14
Background normalization	± 3.4	± 2.4	± 1.1	< 1
JES η intercalibration	< 1	$+0.5/-1.9$	< 1	$+1.5/-0.8$
PDF	± 1.6	± 1.0	< 1	± 1.8
tq generator + parton shower	∓ 1.4	$-7.8/+8.2$	$+4.0/-4.3$	$+3.8/-3.9$
tq scale variation	± 1.9	< 1	< 1	< 1
Total systematic	± 13	± 14	± 13	± 15
Total	± 19	± 17	± 17	± 18

[1] N. Cabibbo, Phys. Rev. Lett. **10**, 531 (1963).

[2] M. Kobayashi and T. Maskawa, Prog. Theor. Phys. **49**, 652 (1973).

[3] G. Altarelli and G. Parisi, Nucl. Phys. B **126**, 298 (1977).

[4] Y. L. Dokshitzer, Sov. Phys. JETP **46**, 641 (1977).

[5] V. Gribov and L. Lipatov, Sov. J. Nucl. Phys. **15**, 438 (1972).

[6] T. M. Tait and C.-P. Yuan, Phys. Rev. D **63**, 014018 (2000).

[7] J. Aguilar-Saavedra, Nucl. Phys. B **804**, 160 (2008).

[8] J. Gao, C. S. Li, L. L. Yang, and H. Zhang, Phys. Rev. Lett. **107**, 092002 (2011).

[9] N. Kidonakis, Phys. Rev. D **83**, 091503 (2011).

[10] A. Martin, W. Stirling, R. Thorne, and G. Watt, Eur. Phys. J. C **63**, 189 (2009).

[11] J. M. Campbell, R. Frederix, F. Maltoni, and F. Tramontano, Phys. Rev. Lett. **102**, 182003 (2009).

[12] N. Kidonakis, Phys. Rev. D **88**, 031504 (2013).

[13] R. Coimbra, A. Onofre, R. Santos, and M. Won, Eur. Phys. J. C **72**, 2222 (2012).

[14] V. Abazov *et al.* (D0 Collaboration), Phys. Lett. B **682**, 363 (2010).

[15] ATLAS Collaboration, Phys. Lett. B **717**, 330 (2012).

[16] ATLAS Collaboration, Phys. Lett. B **716**, 142 (2012).

[17] CMS Collaboration, J. High Energy Phys. **12**, 035 (2012).

[18] CMS Collaboration, Phys. Rev. Lett. **110**, 022003 (2013).

[19] CMS Collaboration, (2014), arXiv:1403.7366 [hep-ex].

[20] ATLAS Collaboration, JINST **3**, S08003 (2008).

[21] ATLAS Collaboration, Eur. Phys. J. C **73**, 2518 (2013).

[22] ATLAS uses a right-handed coordinate system with its origin at the nominal interaction point in the center of the detector and the *z*-axis along the beam direction. The *z*-axis is parallel to the anti-clockwise beam viewed from above. The pseudorapidity η is defined as $\eta = -\ln[\tan(\theta/2)]$, where the polar angle θ is measured with respect to the *z*-axis. The azimuthal angle ϕ is measured with respect to the *x*-axis, which points toward the center of the LHC ring. Transverse momentum and energy are defined as $p_\mathrm{T} = p\sin\theta$ and $E_\mathrm{T} = E\sin\theta$, respectively. The ΔR distance in (η,ϕ) space is defined as $\Delta R = \sqrt{(\Delta\eta)^2 + (\Delta\phi)^2}$.

[23] ATLAS Collaboration, JINST **7**, C01092 (2012).

[24] P. Nason, J. High Energy Phys. **11**, 040 (2004).

[25] T. Sjostrand, S. Mrenna, and P. Z. Skands, J. High Energy Phys. **05**, 026 (2006).

[26] H.-L. Lai, M. Guzzi, J. Huston, Z. Li, P. M. Nadolsky, J. Pumplin, and C.-P. Yuan, Phys. Rev. D **82**, 074024 (2010).

[27] R. Frederix, E. Re, and P. Torrielli, J. High Energy Phys. **09**, 130 (2012).

[28] P. Z. Skands, Phys. Rev. D **82**, 074018 (2010).

[29] M. L. Mangano, M. Moretti, F. Piccinini, R. Pittau, and A. D. Polosa, J. High Energy Phys. **07**, 001 (2003).

[30] J. Pumplin, D. Stump, J. Huston, H.-L. Lai, P. M. Nadolsky, and W. Tung, J. High Energy Phys. **07**, 012 (2002).

[31] G. Corcella, I. Knowles, G. Marchesini, S. Moretti, K. Odagiri, P. Richardson, and B. Seymour, M.H. Webber, J. High Energy Phys. **01**, 010 (2001).

[32] J. Butterworth, J. R. Forshaw, and M. Seymour, Z. Phys. C **72**, 637 (1996).

[33] ATLAS Collaboration, ATL-PHYS-PUB-2011-008 (2011), https://cds.cern.ch/record/1345343.

[34] J. Alwall, S. Hoche, F. Krauss, N. Lavesson, L. Lonnblad, F. Maltoni, M. L. Mangano, M. Moretti, C. Papadopoulos, F. Piccinini, S. Schumann, M. Treccani, J. Winter, and M. Worek, Eur. Phys. J. C **53**, 473 (2008).

[35] ATLAS Collaboration, Eur. Phys. J. C **70**, 823 (2010).

[36] S. Agostinelli *et al.* (GEANT4), Nucl. Instrum. Meth. A **506**, 250 (2003).

[37] ATLAS Collaboration, (2014), arXiv:1404.2240 [hep-ex].

[38] ATLAS Collaboration, (2014), arXiv:1404.4562 [hep-ex].

[39] M. Cacciari, G. P. Salam, and G. Soyez, J. High Energy Phys. **04**, 063 (2008).

[40] ATLAS Collaboration, ATL-LARG-PUB-2008-002 (2008), https://cdsweb.cern.ch/record/1099735.

[41] ATLAS Collaboration, Eur. Phys. J. C **73**, 2304 (2013).

[42] ATLAS Collaboration, (2014), arXiv:1406.0076 [hep-ex].

[43] ATLAS Collaboration, Eur. Phys. J. C **72**, 1844 (2012).

[44] ATLAS Collaboration, ATLAS-CONF-2011-102 (2011), https://cdsweb.cern.ch/record/1369219.

[45] C. Anastasiou, L. J. Dixon, K. Melnikov, and F. Petriello, Phys. Rev. D **69**, 094008 (2004).

[46] J. M. Campbell and R. Ellis, Nucl. Phys. Proc. Suppl. **205-206**, 10 (2010).

[47] ATLAS Collaboration, Phys. Lett. B **711**, 244 (2012).

[48] M. Cacciari, M. Czakon, M. Mangano, A. Mitov, and P. Nason, Phys. Lett. B **710**, 612 (2012).

[49] P. Baernreuther, M. Czakon, and A. Mitov, Phys. Rev. Lett. **109**, 132001 (2012).

[50] M. Czakon and A. Mitov, J. High Energy Phys. **12**, 054 (2012).

[51] M. Czakon and A. Mitov, J. High Energy Phys. **01**, 080 (2013).

[52] M. Czakon, P. Fiedler, and A. Mitov, Phys. Rev. Lett. **110**, 252004 (2013).

[53] M. Czakon and A. Mitov, (2011), arXiv:1112.5675 [hep-ph].

[54] M. Botje, J. Butterworth, A. Cooper-Sarkar, A. de Roeck, J. Feltesse, S. Forte, A. Glazov, J. Huston, R. McNulty, T. Sjostrand, and R. Thorne, (2011), arXiv:1101.0538 [hep-ph].

[55] A. Martin, W. Stirling, R. Thorne, and G. Watt, Eur. Phys. J. C **64**, 653 (2009).

[56] J. Gao, M. Guzzi, J. Huston, H.-L. Lai, Z. Li, P. M. Nadolsky, J. Pumplin, D. Stump, and C.-P. Yuan, Phys. Rev. D **89**, 033009 (2014).

[57] R. D. Ball, V. Bertone, S. Carrazza, C. S. Deans, L. Del Debbio, S. Forte, A. Guffanti, N. P. Hartland, J. I. Latorre, J. Rojo, and M. Ubiali, Nucl. Phys. B **867**, 244 (2013).

[58] N. Kidonakis, Phys. Rev. D **82**, 054018 (2010).

[59] N. Kidonakis, Phys. Rev. D **81**, 054028 (2010).

[60] M. Feindt and U. Kerzel, Nucl. Instrum. Meth. A **559**, 190 (2006).

[61] ATLAS Collaboration, Eur. Phys. J. C **73**, 2306 (2013).

[62] ATLAS Collaboration, ATLAS-CONF-2012-043 (2012), https://cdsweb.cern.ch/record/1435197.

[63] ATLAS Collaboration, ATLAS-CONF-2012-039 (2012), https://cdsweb.cern.ch/record/1435193.

[64] ATLAS Collaboration, ATLAS-CONF-2012-040 (2012), https://cdsweb.cern.ch/record/1435194.

[65] J. Alwall, R. Frederix, S. Frixione, V. Hirschi, F. Maltoni, O. Mattelaer, H.-S. Shao, T. Stelzer, P. Torrielli, and M. Zaro, (2014), arXiv:1405.0301 [hep-ph].

[66] ATLAS Collaboration, Eur. Phys. J. C **72**, 2043 (2012).

[67] R. Thorne, PoS **DIS2010**, 053 (2010).

[68] P. Kant, O. Kind, T. Kintscher, T. Lohse, T. Martini, S. Moelbitz, P. Rieck, and P. Uwer, (2014), arXiv:1406.4403 [hep-ph].

[69] G. D'Agostini, Nucl. Instrum. Meth. A **362**, 487 (1995).

[70] F. Aaron *et al.* (H1 and ZEUS Collaboration), J. High Energy Phys. **01**, 109 (2010).

[71] F. Aaron *et al.* (H1 Collaboration), Eur. Phys. J. C **64**, 561

(2009).

The ATLAS Collaboration

G. Aad[84], B. Abbott[112], J. Abdallah[152], S. Abdel Khalek[116], O. Abdinov[11], R. Aben[106], B. Abi[113], M. Abolins[89],
O.S. AbouZeid[159], H. Abramowicz[154], H. Abreu[153], R. Abreu[30], Y. Abulaiti[147a,147b], B.S. Acharya[165a,165b,a], L. Adamczyk[38a],
D.L. Adams[25], J. Adelman[177], S. Adomeit[99], T. Adye[130], T. Agatonovic-Jovin[13a], J.A. Aguilar-Saavedra[125a,125f],
M. Agustoni[17], S.P. Ahlen[22], F. Ahmadov[64,b], G. Aielli[134a,134b], H. Akerstedt[147a,147b], T.P.A. Åkesson[80], G. Akimoto[156],
A.V. Akimov[95], G.L. Alberghi[20a,20b], J. Albert[170], S. Albrand[55], M.J. Alconada Verzini[70], M. Aleksa[30], I.N. Aleksandrov[64],
C. Alexa[26a], G. Alexander[154], G. Alexandre[49], T. Alexopoulos[10], M. Alhroob[165a,165c], G. Alimonti[90a], L. Alio[84], J. Alison[31],
B.M.M. Allbrooke[18], L.J. Allison[71], P.P. Allport[73], J. Almond[83], A. Aloisio[103a,103b], A. Alonso[36], F. Alonso[70], C. Alpigiani[75],
A. Altheimer[35], B. Alvarez Gonzalez[89], M.G. Alviggi[103a,103b], K. Amako[65], Y. Amaral Coutinho[24a], C. Amelung[23],
D. Amidei[88], S.P. Amor Dos Santos[125a,125c], A. Amorim[125a,125b], S. Amoroso[48], N. Amram[154], G. Amundsen[23],
C. Anastopoulos[140], L.S. Ancu[49], N. Andari[30], T. Andeen[35], C.F. Anders[58b], G. Anders[30], K.J. Anderson[31],
A. Andreazza[90a,90b], V. Andrei[58a], X.S. Anduaga[70], S. Angelidakis[9], I. Angelozzi[106], P. Anger[44], A. Angerami[35],
F. Anghinolfi[30], A.V. Anisenkov[108], N. Anjos[125a], A. Annovi[47], A. Antonaki[9], M. Antonelli[47], A. Antonov[97], J. Antos[145b],
F. Anulli[133a], M. Aoki[65], L. Aperio Bella[18], R. Apolle[119,c], G. Arabidze[89], I. Aracena[144], Y. Arai[65], J.P. Araque[125a],
A.T.H. Arce[45], J-F. Arguin[94], S. Argyropoulos[42], M. Arik[19a], A.J. Armbruster[30], O. Arnaez[30], V. Arnal[81], H. Arnold[48],
M. Arratia[28], O. Arslan[21], A. Artamonov[96], G. Artoni[23], S. Asai[156], N. Asbah[42], A. Ashkenazi[154], B. Åsman[147a,147b],
L. Asquith[6], K. Assamagan[25], R. Astalos[145a], M. Atkinson[166], N.B. Atlay[142], B. Auerbach[6], K. Augsten[127],
M. Aurousseau[146b], G. Avolio[30], G. Azuelos[94,d], Y. Azuma[156], M.A. Baak[30], A. Baas[58a], C. Bacci[135a,135b], H. Bachacou[137],
K. Bachas[155], M. Backes[30], M. Backhaus[30], J. Backus Mayes[144], E. Badescu[26a], P. Bagiacchi[133a,133b], P. Bagnaia[133a,133b],
Y. Bai[33a], T. Bain[35], J.T. Baines[130], O.K. Baker[177], P. Balek[128], F. Balli[137], E. Banas[39], Sw. Banerjee[174], A.A.E. Bannoura[176],
V. Bansal[170], H.S. Bansil[18], L. Barak[173], S.P. Baranov[95], E.L. Barberio[87], D. Barberis[50a,50b], M. Barbero[84], T. Barillari[100],
M. Barisonzi[176], T. Barklow[144], N. Barlow[28], B.M. Barnett[130], R.M. Barnett[15], Z. Barnovska[5], A. Baroncelli[135a], G. Barone[49],
A.J. Barr[119], F. Barreiro[81], J. Barreiro Guimarães da Costa[57], R. Bartoldus[144], A.E. Barton[71], P. Bartos[145a], V. Bartsch[150],
A. Bassalat[116], A. Basye[166], R.L. Bates[53], J.R. Batley[28], M. Battaglia[138], M. Battistin[30], F. Bauer[137], H.S. Bawa[144,e],
M.D. Beattie[71], T. Beau[79], P.H. Beauchemin[162], R. Beccherle[123a,123b], P. Bechtle[21], H.P. Beck[17], K. Becker[176], S. Becker[99],
M. Beckingham[171], C. Becot[116], A.J. Beddall[19c], A. Beddall[19c], S. Bedikian[177], V.A. Bednyakov[64], C.P. Bee[149],
L.J. Beemster[106], T.A. Beermann[176], M. Begel[25], K. Behr[119], C. Belanger-Champagne[86], P.J. Bell[49], W.H. Bell[49], G. Bella[154],
L. Bellagamba[20a], A. Bellerive[29], M. Bellomo[85], K. Belotskiy[97], O. Beltramello[30], O. Benary[154], D. Benchekroun[136a],
K. Bendtz[147a,147b], N. Benekos[166], Y. Benhammou[154], E. Benhar Noccioli[49], J.A. Benitez Garcia[160b], D.P. Benjamin[45],
J.R. Bensinger[23], K. Benslama[131], S. Bentvelsen[106], D. Berge[106], E. Bergeaas Kuutmann[16], N. Berger[5], F. Berghaus[170],
J. Beringer[15], C. Bernard[22], P. Bernat[77], C. Bernius[78], F.U. Bernlochner[170], T. Berry[76], P. Berta[128], C. Bertella[84],
G. Bertoli[147a,147b], F. Bertolucci[123a,123b], C. Bertsche[112], D. Bertsche[112], M.I. Besana[90a], G.J. Besjes[105], O. Bessidskaia[147a,147b],
M.F. Bessner[42], N. Besson[137], C. Betancourt[48], S. Bethke[100], W. Bhimji[46], R.M. Bianchi[124], L. Bianchini[23], M. Bianco[30],
O. Biebel[99], S.P. Bieniek[77], K. Bierwagen[54], J. Biesiada[15], M. Biglietti[135a], J. Bilbao De Mendizabal[49], H. Bilokon[47],
M. Bindi[54], S. Binet[116], A. Bingul[19c], C. Bini[133a,133b], C.W. Black[151], J.E. Black[144], K.M. Black[22], D. Blackburn[139],
R.E. Blair[6], J.-B. Blanchard[137], T. Blazek[145a], I. Bloch[42], C. Blocker[23], W. Blum[82,*], U. Blumenschein[54], G.J. Bobbink[106],
V.S. Bobrovnikov[108], S.S. Bocchetta[80], A. Bocci[45], C. Bock[99], C.R. Boddy[119], M. Boehler[48], T.T. Boek[176], J.A. Bogaerts[30],
A.G. Bogdanchikov[108], A. Bogouch[91,*], C. Bohm[147a], J. Bohm[126], V. Boisvert[76], T. Bold[38a], V. Boldea[26a], A.S. Boldyrev[98],
M. Bomben[79], M. Bona[75], M. Boonekamp[137], A. Borisov[129], G. Borissov[71], M. Borri[83], S. Borroni[42], J. Bortfeldt[99],
V. Bortolotto[135a,135b], K. Bos[106], D. Boscherini[20a], M. Bosman[12], H. Boterenbrood[106], J. Boudreau[124], J. Bouffard[2],
E.V. Bouhova-Thacker[71], D. Boumediene[34], C. Bourdarios[116], N. Bousson[113], S. Boutouil[136d], A. Boveia[31], J. Boyd[30],
I.R. Boyko[64], J. Bracinik[18], A. Brandt[8], G. Brandt[15], O. Brandt[58a], U. Bratzler[157], B. Brau[85], J.E. Brau[115], H.M. Braun[176,*],
S.F. Brazzale[165a,165c], B. Brelier[159], K. Brendlinger[121], A.J. Brennan[87], R. Brenner[167], S. Bressler[173], K. Bristow[146c],
T.M. Bristow[46], D. Britton[53], F.M. Brochu[28], I. Brock[21], R. Brock[89], C. Bromberg[89], J. Bronner[100], G. Brooijmans[35],
T. Brooks[76], W.K. Brooks[32b], J. Brosamer[15], E. Brost[115], J. Brown[55], P.A. Bruckman de Renstrom[39], D. Bruncko[145b],
R. Bruneliere[48], S. Brunet[60], A. Bruni[20a], G. Bruni[20a], M. Bruschi[20a], L. Bryngemark[80], T. Buanes[14], Q. Buat[143], F. Bucci[49],
P. Buchholz[142], R.M. Buckingham[119], A.G. Buckley[53], S.I. Buda[26a], I.A. Budagov[64], F. Buehrer[48], L. Bugge[118],
M.K. Bugge[118], O. Bulekov[97], A.C. Bundock[73], H. Burckhart[30], S. Burdin[73], B. Burghgrave[107], S. Burke[130], I. Burmeister[43],
E. Busato[34], D. Büscher[48], V. Büscher[82], P. Bussey[53], C.P. Buszello[167], B. Butler[57], J.M. Butler[22], A.I. Butt[3], C.M. Buttar[53],
J.M. Butterworth[77], P. Butti[106], W. Buttinger[28], A. Buzatu[53], M. Byszewski[10], S. Cabrera Urbán[168], D. Caforio[20a,20b],
O. Cakir[4a], P. Calafiura[15], A. Calandri[137], G. Calderini[79], P. Calfayan[99], R. Calkins[107], L.P. Caloba[24a], D. Calvet[34], S. Calvet[34],
R. Camacho Toro[49], S. Camarda[42], D. Cameron[118], L.M. Caminada[15], R. Caminal Armadans[12], S. Campana[30],
M. Campanelli[77], A. Campoverde[149], V. Canale[103a,103b], A. Canepa[160a], M. Cano Bret[75], J. Cantero[81], R. Cantrill[125a], T. Cao[40],
M.D.M. Capeans Garrido[30], I. Caprini[26a], M. Caprini[26a], M. Capua[37a,37b], R. Caputo[82], R. Cardarelli[134a], T. Carli[30],
G. Carlino[103a], L. Carminati[90a,90b], S. Caron[105], E. Carquin[32a], G.D. Carrillo-Montoya[146c], J.R. Carter[28], J. Carvalho[125a,125c],
D. Casadei[77], M.P. Casado[12], M. Casolino[12], E. Castaneda-Miranda[146b], A. Castelli[106], V. Castillo Gimenez[168], N.F. Castro[125a],
P. Catastini[57], A. Catinaccio[30], J.R. Catmore[118], A. Cattai[30], G. Cattani[134a,134b], S. Caughron[89], V. Cavaliere[166], D. Cavalli[90a],

M. Cavalli-Sforza[12], V. Cavasinni[123a,123b], F. Ceradini[135a,135b], B. Cerio[45], K. Cerny[128], A.S. Cerqueira[24b], A. Cerri[150], L. Cerrito[75], F. Cerutti[15], M. Cerv[30], A. Cervelli[17], S.A. Cetin[19b], A. Chafaq[136a], D. Chakraborty[107], I. Chalupkova[128], P. Chang[166], B. Chapleau[86], J.D. Chapman[28], D. Charfeddine[116], D.G. Charlton[18], C.C. Chau[159], C.A. Chavez Barajas[150], S. Cheatham[86], A. Chegwidden[89], S. Chekanov[6], S.V. Chekulaev[160a], G.A. Chelkov[64,f], M.A. Chelstowska[88], C. Chen[63], H. Chen[25], K. Chen[149], L. Chen[33d,g], S. Chen[33c], X. Chen[146c], Y. Chen[66], Y. Chen[35], H.C. Cheng[88], Y. Cheng[31], A. Cheplakov[64], R. Cherkaoui El Moursli[136e], V. Chernyatin[25,*], E. Cheu[7], L. Chevalier[137], V. Chiarella[47], G. Chiefari[103a,103b], J.T. Childers[6], A. Chilingarov[71], G. Chiodini[72a], A.S. Chisholm[18], R.T. Chislett[77], A. Chitan[26a], M.V. Chizhov[64], S. Chouridou[9], B.K.B. Chow[99], D. Chromek-Burckhart[30], M.L. Chu[152], J. Chudoba[126], J.J. Chwastowski[39], L. Chytka[114], G. Ciapetti[133a,133b], A.K. Ciftci[4a], R. Ciftci[4a], D. Cinca[53], V. Cindro[74], A. Ciocio[15], P. Cirkovic[13b], Z.H. Citron[173], M. Citterio[90a], M. Ciubancan[26a], A. Clark[49], P.J. Clark[46], R.N. Clarke[15], W. Cleland[124], J.C. Clemens[84], C. Clement[147a,147b], Y. Coadou[84], M. Cobal[165a,165c], A. Coccaro[139], J. Cochran[63], L. Coffey[23], J.G. Cogan[144], J. Coggeshall[166], B. Cole[35], S. Cole[107], A.P. Colijn[106], J. Collot[55], T. Colombo[58c], G. Colon[85], G. Compostella[100], P. Conde Muiño[125a,125b], E. Coniavitis[48], M.C. Conidi[12], S.H. Connell[146b], I.A. Connelly[76], S.M. Consonni[90a,90b], V. Consorti[48], S. Constantinescu[26a], C. Conta[120a,120b], G. Conti[57], F. Conventi[103a,h], M. Cooke[15], B.D. Cooper[77], A.M. Cooper-Sarkar[119], N.J. Cooper-Smith[76], K. Copic[15], T. Cornelissen[176], M. Corradi[20a], F. Corriveau[86,i], A. Corso-Radu[164], A. Cortes-Gonzalez[12], G. Cortiana[100], G. Costa[90a], M.J. Costa[168], D. Costanzo[140], D. Côté[8], G. Cottin[28], G. Cowan[76], B.E. Cox[83], K. Cranmer[109], G. Cree[29], S. Crépé-Renaudin[55], F. Crescioli[79], W.A. Cribbs[147a,147b], M. Crispin Ortuzar[119], M. Cristinziani[21], V. Croft[105], G. Crosetti[37a,37b], C.-M. Cuciuc[26a], T. Cuhadar Donszelmann[140], J. Cummings[177], M. Curatolo[47], C. Cuthbert[151], H. Czirr[142], P. Czodrowski[3], Z. Czyczula[177], S. D'Auria[53], M. D'Onofrio[73], M.J. Da Cunha Sargedas De Sousa[125a,125b], C. Da Via[83], W. Dabrowski[38a], A. Dafinca[119], T. Dai[88], O. Dale[14], F. Dallaire[94], C. Dallapiccola[85], M. Dam[36], A.C. Daniells[18], M. Dano Hoffmann[137], V. Dao[48], G. Darbo[50a], S. Darmora[8], J.A. Dassoulas[42], A. Dattagupta[60], W. Davey[21], C. David[170], T. Davidek[128], E. Davies[119,c], M. Davies[154], O. Davignon[79], A.R. Davison[77], P. Davison[77], Y. Davygora[58a], E. Dawe[143], I. Dawson[140], R.K. Daya-Ishmukhametova[85], K. De[8], R. de Asmundis[103a], S. De Castro[20a,20b], S. De Cecco[79], N. De Groot[105], P. de Jong[106], H. De la Torre[81], F. De Lorenzi[63], L. De Nooij[106], D. De Pedis[133a], A. De Salvo[133a], U. De Sanctis[165a,165b], A. De Santo[150], J.B. De Vivie De Regie[116], W.J. Dearnaley[71], R. Debbe[25], C. Debenedetti[138], B. Dechenaux[55], D.V. Dedovich[64], I. Deigaard[106], J. Del Peso[81], T. Del Prete[123a,123b], F. Deliot[137], C.M. Delitzsch[49], M. Deliyergiyev[74], A. Dell'Acqua[30], L. Dell'Asta[22], M. Dell'Orso[123a,123b], M. Della Pietra[103a,h], D. della Volpe[49], M. Delmastro[5], P.A. Delsart[55], C. Deluca[106], S. Demers[177], M. Demichev[64], A. Demilly[79], S.P. Denisov[129], D. Derendarz[39], J.E. Derkaoui[136d], F. Derue[79], P. Dervan[73], K. Desch[21], C. Deterre[42], P.O. Deviveiros[106], A. Dewhurst[130], S. Dhaliwal[106], A. Di Ciaccio[134a,134b], L. Di Ciaccio[5], A. Di Domenico[133a,133b], C. Di Donato[103a,103b], A. Di Girolamo[30], B. Di Girolamo[30], A. Di Mattia[153], B. Di Micco[135a,135b], R. Di Nardo[47], A. Di Simone[48], R. Di Sipio[20a,20b], D. Di Valentino[29], F.A. Dias[46], M.A. Diaz[32a], E.B. Diehl[88], J. Dietrich[42], T.A. Dietzsch[58a], S. Diglio[84], A. Dimitrievska[13a], J. Dingfelder[21], C. Dionisi[133a,133b], P. Dita[26a], S. Dita[26a], F. Dittus[30], F. Djama[84], T. Djobava[51b], M.A.B. do Vale[24c], A. Do Valle Wemans[125a,125g], T.K.O. Doan[5], D. Dobos[30], C. Doglioni[49], T. Doherty[53], T. Dohmae[156], J. Dolejsi[128], Z. Dolezal[128], B.A. Dolgoshein[97,*], M. Donadelli[24d], S. Donati[123a,123b], P. Dondero[120a,120b], J. Donini[34], J. Dopke[130], A. Doria[103a], M.T. Dova[70], A.T. Doyle[53], M. Dris[10], J. Dubbert[88], S. Dube[15], E. Dubreuil[34], E. Duchovni[173], G. Duckeck[99], O.A. Ducu[26a], D. Duda[176], A. Dudarev[30], F. Dudziak[63], L. Duflot[116], L. Duguid[76], M. Dührssen[30], M. Dunford[58a], H. Duran Yildiz[4a], M. Düren[52], A. Durglishvili[51b], M. Dwuznik[38a], M. Dyndal[38a], J. Ebke[99], W. Edson[2], N.C. Edwards[46], W. Ehrenfeld[21], T. Eifert[144], G. Eigen[14], K. Einsweiler[15], T. Ekelof[167], M. El Kacimi[136c], M. Ellert[167], S. Elles[5], F. Ellinghaus[82], N. Ellis[30], J. Elmsheuser[99], M. Elsing[30], D. Emeliyanov[130], Y. Enari[156], O.C. Endner[82], M. Endo[117], R. Engelmann[149], J. Erdmann[177], A. Ereditato[17], D. Eriksson[147a], G. Ernis[176], J. Ernst[2], M. Ernst[25], J. Ernwein[137], D. Errede[166], S. Errede[166], E. Ertel[82], M. Escalier[116], H. Esch[43], C. Escobar[124], B. Esposito[47], A.I. Etienvre[137], E. Etzion[154], H. Evans[60], A. Ezhilov[122], L. Fabbri[20a,20b], G. Facini[31], R.M. Fakhrutdinov[129], S. Falciano[133a], R.J. Falla[77], J. Faltova[128], Y. Fang[33a], M. Fanti[90a,90b], A. Farbin[8], A. Farilla[135a], T. Farooque[12], S. Farrell[15], S.M. Farrington[171], P. Farthouat[30], F. Fassi[136e], P. Fassnacht[30], D. Fassouliotis[9], A. Favareto[50a,50b], L. Fayard[116], P. Federic[145a], O.L. Fedin[122,j], W. Fedorko[169], M. Fehling-Kaschek[48], S. Feigl[30], L. Feligioni[84], C. Feng[33d], E.J. Feng[6], H. Feng[88], A.B. Fenyuk[129], S. Fernandez Perez[30], S. Ferrag[53], J. Ferrando[53], A. Ferrari[167], P. Ferrari[106], R. Ferrari[120a], D.E. Ferreira de Lima[53], A. Ferrer[168], D. Ferrere[49], C. Ferretti[88], A. Ferretto Parodi[50a,50b], M. Fiascaris[31], F. Fiedler[82], A. Filipčič[74], M. Filipuzzi[42], F. Filthaut[105], M. Fincke-Keeler[170], K.D. Finelli[151], M.C.N. Fiolhais[125a,125c], L. Fiorini[168], A. Firan[40], A. Fischer[2], J. Fischer[176], W.C. Fisher[89], E.A. Fitzgerald[23], M. Flechl[48], I. Fleck[142], P. Fleischmann[88], S. Fleischmann[176], G.T. Fletcher[140], G. Fletcher[75], T. Flick[176], A. Floderus[80], L.R. Flores Castillo[174,k], A.C. Florez Bustos[160b], M.J. Flowerdew[100], A. Formica[137], A. Forti[83], D. Fortin[160a], D. Fournier[116], H. Fox[71], S. Fracchia[12], P. Francavilla[79], M. Franchini[20a,20b], S. Franchino[30], D. Francis[30], L. Franconi[118], M. Franklin[57], S. Franz[61], M. Fraternali[120a,120b], S.T. French[28], C. Friedrich[42], F. Friedrich[44], D. Froidevaux[30], J.A. Frost[28], C. Fukunaga[157], E. Fullana Torregrosa[82], B.G. Fulsom[144], J. Fuster[168], C. Gabaldon[55], O. Gabizon[173], A. Gabrielli[20a,20b], A. Gabrielli[133a,133b], S. Gadatsch[106], S. Gadomski[49], G. Gagliardi[50a,50b], P. Gagnon[60], C. Galea[105], B. Galhardo[125a,125c], E.J. Gallas[119], V. Gallo[17], B.J. Gallop[130], P. Gallus[127], G. Galster[36], K.K. Gan[110], R.P. Gandrajula[62], J. Gao[33b,g], Y.S. Gao[144,e], F.M. Garay Walls[46], F. Garberson[177], C. García[168], J.E. García Navarro[168], M. Garcia-Sciveres[15], R.W. Gardner[31], N. Garelli[144], V. Garonne[30], C. Gatti[47], G. Gaudio[120a], B. Gaur[142], L. Gauthier[94], P. Gauzzi[133a,133b], I.L. Gavrilenko[95], C. Gay[169], G. Gaycken[21], E.N. Gazis[10],

P. Ge[33d], Z. Gecse[169], C.N.P. Gee[130], D.A.A. Geerts[106], Ch. Geich-Gimbel[21], K. Gellerstedt[147a,147b], C. Gemme[50a], A. Gemmell[53], M.H. Genest[55], S. Gentile[133a,133b], M. George[54], S. George[76], D. Gerbaudo[164], A. Gershon[154], H. Ghazlane[136b], N. Ghodbane[34], B. Giacobbe[20a], S. Giagu[133a,133b], V. Giangiobbe[12], P. Giannetti[123a,123b], F. Gianotti[30], B. Gibbard[25], S.M. Gibson[76], M. Gilchriese[15], T.P.S. Gillam[28], D. Gillberg[30], G. Gilles[34], D.M. Gingrich[3,d], N. Giokaris[9], M.P. Giordani[165a,165c], R. Giordano[103a,103b], F.M. Giorgi[20a], F.M. Giorgi[16], P.F. Giraud[137], D. Giugni[90a], C. Giuliani[48], M. Giulini[58b], B.K. Gjelsten[118], S. Gkaitatzis[155], I. Gkialas[155,l], L.K. Gladilin[98], C. Glasman[81], J. Glatzer[30], P.C.F. Glaysher[46], A. Glazov[42], G.L. Glonti[64], M. Goblirsch-Kolb[100], J.R. Goddard[75], J. Godfrey[143], J. Godlewski[30], C. Goeringer[82], S. Goldfarb[88], T. Golling[177], D. Golubkov[129], A. Gomes[125a,125b,125d], L.S. Gomez Fajardo[42], R. Gonçalo[125a], J. Goncalves Pinto Firmino Da Costa[137], L. Gonella[21], S. González de la Hoz[168], G. Gonzalez Parra[12], S. Gonzalez-Sevilla[49], L. Goossens[30], P.A. Gorbounov[96], H.A. Gordon[25], I. Gorelov[104], B. Gorini[30], E. Gorini[72a,72b], A. Gorišek[74], E. Gornicki[39], A.T. Goshaw[6], C. Gössling[43], M.I. Gostkin[64], M. Gouighri[136a], D. Goujdami[136c], M.P. Goulette[49], A.G. Goussiou[139], C. Goy[5], S. Gozpinar[23], H.M.X. Grabas[137], L. Graber[54], I. Grabowska-Bold[38a], P. Grafström[20a,20b], K-J. Grahn[42], J. Gramling[49], E. Gramstad[118], S. Grancagnolo[16], V. Grassi[149], V. Gratchev[122], H.M. Gray[30], E. Graziani[135a], O.G. Grebenyuk[122], Z.D. Greenwood[78,m], K. Gregersen[77], I.M. Gregor[42], P. Grenier[144], J. Griffiths[8], A.A. Grillo[138], K. Grimm[71], S. Grinstein[12,n], Ph. Gris[34], Y.V. Grishkevich[98], J.-F. Grivaz[116], J.P. Grohs[44], A. Grohsjean[42], E. Gross[173], J. Grosse-Knetter[54], G.C. Grossi[134a,134b], J. Groth-Jensen[173], Z.J. Grout[150], L. Guan[33b], F. Guescini[49], D. Guest[177], O. Gueta[154], C. Guicheney[34], E. Guido[50a,50b], T. Guillemin[116], S. Guindon[2], U. Gul[53], C. Gumpert[44], J. Gunther[127], J. Guo[35], S. Gupta[119], P. Gutierrez[112], N.G. Gutierrez Ortiz[53], C. Gutschow[77], N. Guttman[154], C. Guyot[137], C. Gwenlan[119], C.B. Gwilliam[73], A. Haas[109], C. Haber[15], H.K. Hadavand[8], N. Haddad[136e], P. Haefner[21], S. Hageböck[21], Z. Hajduk[39], H. Hakobyan[178], M. Haleem[42], D. Hall[119], G. Halladjian[89], K. Hamacher[176], P. Hamal[114], K. Hamano[170], M. Hamer[54], A. Hamilton[146a], S. Hamilton[162], G.N. Hamity[146c], P.G. Hamnett[42], L. Han[33b], K. Hanagaki[117], K. Hanawa[156], M. Hance[15], P. Hanke[58a], R. Hanna[137], J.B. Hansen[36], J.D. Hansen[36], P.H. Hansen[36], K. Hara[161], A.S. Hard[174], T. Harenberg[176], F. Hariri[116], S. Harkusha[91], D. Harper[88], R.D. Harrington[46], O.M. Harris[139], P.F. Harrison[171], F. Hartjes[106], M. Hasegawa[66], S. Hasegawa[102], Y. Hasegawa[141], A. Hasib[112], S. Hassani[137], S. Haug[17], M. Hauschild[30], R. Hauser[89], M. Havranek[126], C.M. Hawkes[18], R.J. Hawkings[30], A.D. Hawkins[80], T. Hayashi[161], D. Hayden[89], C.P. Hays[119], H.S. Hayward[73], S.J. Haywood[130], S.J. Head[18], T. Heck[82], V. Hedberg[80], L. Heelan[8], S. Heim[121], T. Heim[176], B. Heinemann[15], L. Heinrich[109], J. Hejbal[126], L. Helary[22], C. Heller[99], M. Heller[30], S. Hellman[147a,147b], D. Hellmich[21], C. Helsens[30], J. Henderson[119], R.C.W. Henderson[71], Y. Heng[174], C. Hengler[42], A. Henrichs[177], A.M. Henriques Correia[30], S. Henrot-Versille[116], C. Hensel[54], G.H. Herbert[16], Y. Hernández Jiménez[168], R. Herrberg-Schubert[16], G. Herten[48], R. Hertenberger[99], L. Hervas[30], G.G. Hesketh[77], N.P. Hessey[106], R. Hickling[75], E. Higón-Rodriguez[168], E. Hill[170], J.C. Hill[28], K.H. Hiller[42], S. Hillert[21], S.J. Hillier[18], I. Hinchliffe[15], E. Hines[121], M. Hirose[158], D. Hirschbuehl[176], J. Hobbs[149], N. Hod[106], M.C. Hodgkinson[140], P. Hodgson[140], A. Hoecker[30], M.R. Hoeferkamp[104], F. Hoenig[99], J. Hoffman[40], D. Hoffmann[84], J.I. Hofmann[58a], M. Hohlfeld[82], T.R. Holmes[15], T.M. Hong[121], L. Hooft van Huysduynen[109], J-Y. Hostachy[55], S. Hou[152], A. Hoummada[136a], J. Howard[119], J. Howarth[42], M. Hrabovsky[114], I. Hristova[16], J. Hrivnac[116], T. Hryn'ova[5], C. Hsu[146c], P.J. Hsu[82], S.-C. Hsu[139], D. Hu[35], X. Hu[25], Y. Huang[42], Z. Hubacek[30], F. Hubaut[84], F. Huegging[21], T.B. Huffman[119], E.W. Hughes[35], G. Hughes[71], M. Huhtinen[30], T.A. Hülsing[82], M. Hurwitz[15], N. Huseynov[64,b], J. Huston[89], J. Huth[57], G. Iacobucci[49], G. Iakovidis[10], I. Ibragimov[142], L. Iconomidou-Fayard[116], E. Ideal[177], P. Iengo[103a], O. Igonkina[106], T. Iizawa[172], Y. Ikegami[65], K. Ikematsu[142], M. Ikeno[65], Y. Ilchenko[31], D. Iliadis[155], N. Ilic[159], Y. Inamaru[66], T. Ince[100], P. Ioannou[9], M. Iodice[135a], K. Iordanidou[9], V. Ippolito[57], A. Irles Quiles[168], C. Isaksson[167], M. Ishino[67], M. Ishitsuka[158], R. Ishmukhametov[110], C. Issever[119], S. Istin[19a], J.M. Iturbe Ponce[83], R. Iuppa[134a,134b], J. Ivarsson[80], W. Iwanski[39], H. Iwasaki[65], J.M. Izen[41], V. Izzo[103a], B. Jackson[121], M. Jackson[73], P. Jackson[1], M.R. Jaekel[30], V. Jain[2], K. Jakobs[48], S. Jakobsen[30], T. Jakoubek[126], J. Jakubek[127], D.O. Jamin[152], D.K. Jana[78], E. Jansen[77], H. Jansen[30], J. Janssen[21], M. Janus[171], G. Jarlskog[80], N. Javadov[64,b], T. Javůrek[48], L. Jeanty[15], J. Jejelava[51a,o], G.-Y. Jeng[151], D. Jennens[87], P. Jenni[48,p], J. Jentzsch[43], C. Jeske[171], S. Jézéquel[5], H. Ji[174], J. Jia[149], Y. Jiang[33b], M. Jimenez Belenguer[42], S. Jin[33a], A. Jinaru[26a], O. Jinnouchi[158], M.D. Joergensen[36], K.E. Johansson[147a,147b], P. Johansson[140], K.A. Johns[7], K. Jon-And[147a,147b], G. Jones[171], R.W.L. Jones[71], T.J. Jones[73], J. Jongmanns[58a], P.M. Jorge[125a,125b], K.D. Joshi[83], J. Jovicevic[148], X. Ju[174], C.A. Jung[43], R.M. Jungst[30], P. Jussel[61], A. Juste Rozas[12,n], M. Kaci[168], A. Kaczmarska[39], M. Kado[116], H. Kagan[110], M. Kagan[144], E. Kajomovitz[45], C.W. Kalderon[119], S. Kama[40], A. Kamenshchikov[129], N. Kanaya[156], M. Kaneda[30], S. Kaneti[28], V.A. Kantserov[97], J. Kanzaki[65], B. Kaplan[109], A. Kapliy[31], D. Kar[53], K. Karakostas[10], N. Karastathis[10], M. Karnevskiy[82], S.N. Karpov[64], Z.M. Karpova[64], K. Karthik[109], V. Kartvelishvili[71], A.N. Karyukhin[129], L. Kashif[174], G. Kasieczka[58b], R.D. Kass[110], A. Kastanas[14], Y. Kataoka[156], A. Katre[49], J. Katzy[42], V. Kaushik[7], K. Kawagoe[69], T. Kawamoto[156], G. Kawamura[54], S. Kazama[156], V.F. Kazanin[108], M.Y. Kazarinov[64], R. Keeler[170], R. Kehoe[40], M. Keil[54], J.S. Keller[42], J.J. Kempster[76], H. Keoshkerian[5], O. Kepka[126], B.P. Kerševan[74], S. Kersten[176], K. Kessoku[156], J. Keung[159], F. Khalil-zada[11], H. Khandanyan[147a,147b], A. Khanov[113], A. Khodinov[97], A. Khomich[58a], T.J. Khoo[28], G. Khoriauli[21], A. Khoroshilov[176], V. Khovanskiy[96], E. Khramov[64], J. Khubua[51b], H.Y. Kim[8], H. Kim[147a,147b], S.H. Kim[161], N. Kimura[172], O. Kind[16], B.T. King[73], M. King[168], R.S.B. King[119], S.B. King[169], J. Kirk[130], A.E. Kiryunin[100], T. Kishimoto[66], D. Kisielewska[38a], F. Kiss[48], T. Kittelmann[124], K. Kiuchi[161], E. Kladiva[145b], M. Klein[73], U. Klein[73], K. Kleinknecht[82], P. Klimek[147a,147b], A. Klimentov[25], R. Klingenberg[43], J.A. Klinger[83], T. Klioutchnikova[30], P.F. Klok[105], E.-E. Kluge[58a], P. Kluit[106], S. Kluth[100], E. Kneringer[61], E.B.F.G. Knoops[84], A. Knue[53], D. Kobayashi[158], T. Kobayashi[156], M. Kobel[44],

M. Kocian[144], P. Kodys[128], P. Koevesarki[21], T. Koffas[29], E. Koffeman[106], L.A. Kogan[119], S. Kohlmann[176], Z. Kohout[127], T. Kohriki[65], T. Koi[144], H. Kolanoski[16], I. Koletsou[5], J. Koll[89], A.A. Komar[95,∗], Y. Komori[156], T. Kondo[65], N. Kondrashova[42], K. Köneke[48], A.C. König[105], S. König[82], T. Kono[65,q], R. Konoplich[109,r], N. Konstantinidis[77], R. Kopeliansky[153], S. Koperny[38a], L. Köpke[82], A.K. Kopp[48], K. Korcyl[39], K. Kordas[155], A. Korn[77], A.A. Korol[108,s], I. Korolkov[12], E.V. Korolkova[140], V.A. Korotkov[129], O. Kortner[100], S. Kortner[100], V.V. Kostyukhin[21], V.M. Kotov[64], A. Kotwal[45], C. Kourkoumelis[9], V. Kouskoura[155], A. Koutsman[160a], R. Kowalewski[170], T.Z. Kowalski[38a], W. Kozanecki[137], A.S. Kozhin[129], V. Kral[127], V.A. Kramarenko[98], G. Kramberger[74], D. Krasnopevtsev[97], M.W. Krasny[79], A. Krasznahorkay[30], J.K. Kraus[21], A. Kravchenko[25], S. Kreiss[109], M. Kretz[58c], J. Kretzschmar[73], K. Kreutzfeldt[52], P. Krieger[159], K. Kroeninger[54], H. Kroha[100], J. Kroll[121], J. Kroseberg[21], J. Krstic[13a], U. Kruchonak[64], H. Krüger[21], T. Kruker[17], N. Krumnack[63], Z.V. Krumshteyn[64], A. Kruse[174], M.C. Kruse[45], M. Kruskal[22], T. Kubota[87], S. Kuday[4a], S. Kuehn[48], A. Kugel[58c], A. Kuhl[138], T. Kuhl[42], V. Kukhtin[64], Y. Kulchitsky[91], S. Kuleshov[32b], M. Kuna[133a,133b], J. Kunkle[121], A. Kupco[126], H. Kurashige[66], Y.A. Kurochkin[91], R. Kurumida[66], V. Kus[126], E.S. Kuwertz[148], M. Kuze[158], J. Kvita[114], A. La Rosa[49], L. La Rotonda[37a,37b], C. Lacasta[168], F. Lacava[133a,133b], J. Lacey[29], H. Lacker[16], D. Lacour[79], V.R. Lacuesta[168], E. Ladygin[64], R. Lafaye[5], B. Laforge[79], T. Lagouri[177], S. Lai[48], H. Laier[58a], L. Lambourne[77], S. Lammers[60], C.L. Lampen[7], W. Lampl[7], E. Lançon[137], U. Landgraf[48], M.P.J. Landon[75], V.S. Lang[58a], A.J. Lankford[164], F. Lanni[25], K. Lantzsch[30], S. Laplace[79], C. Lapoire[21], J.F. Laporte[137], T. Lari[90a], M. Lassnig[30], P. Laurelli[47], W. Lavrijsen[15], A.T. Law[138], P. Laycock[73], O. Le Dortz[79], E. Le Guirriec[84], E. Le Menedeu[12], T. LeCompte[6], F. Ledroit-Guillon[55], C.A. Lee[152], H. Lee[106], J.S.H. Lee[117], S.C. Lee[152], L. Lee[177], G. Lefebvre[79], M. Lefebvre[170], F. Legger[99], C. Leggett[15], A. Lehan[73], M. Lehmacher[21], G. Lehmann Miotto[30], X. Lei[7], W.A. Leight[29], A. Leisos[155], A.G. Leister[177], M.A.L. Leite[24d], R. Leitner[128], D. Lellouch[173], B. Lemmer[54], K.J.C. Leney[77], T. Lenz[21], G. Lenzen[176], B. Lenzi[30], R. Leone[7], S. Leone[123a,123b], K. Leonhardt[44], C. Leonidopoulos[46], S. Leontsinis[10], C. Leroy[94], C.G. Lester[28], C.M. Lester[121], M. Levchenko[122], J. Levêque[5], D. Levin[88], L.J. Levinson[173], M. Levy[18], A. Lewis[119], G.H. Lewis[109], A.M. Leyko[21], M. Leyton[41], B. Li[33b,t], B. Li[84], H. Li[149], H.L. Li[31], L. Li[45], L. Li[33e], S. Li[45], Y. Li[33c,u], Z. Liang[138], H. Liao[34], B. Liberti[134a], P. Lichard[30], K. Lie[166], J. Liebal[21], W. Liebig[14], C. Limbach[21], A. Limosani[87], S.C. Lin[152,v], T.H. Lin[82], F. Linde[106], B.E. Lindquist[149], J.T. Linnemann[89], E. Lipeles[121], A. Lipniacka[14], M. Lisovyi[42], T.M. Liss[166], D. Lissauer[25], A. Lister[169], A.M. Litke[138], B. Liu[152], D. Liu[152], J.B. Liu[33b], K. Liu[33b,w], L. Liu[88], M. Liu[45], M. Liu[33b], Y. Liu[33b], M. Livan[120a,120b], S.S.A. Livermore[119], A. Lleres[55], J. Llorente Merino[81], S.L. Lloyd[75], F. Lo Sterzo[152], E. Lobodzinska[42], P. Loch[7], W.S. Lockman[138], T. Loddenkoetter[21], F.K. Loebinger[83], A.E. Loevschall-Jensen[36], A. Loginov[177], T. Lohse[16], K. Lohwasser[42], M. Lokajicek[126], V.P. Lombardo[5], B.A. Long[22], J.D. Long[88], R.E. Long[71], L. Lopes[125a], D. Lopez Mateos[57], B. Lopez Paredes[140], I. Lopez Paz[12], J. Lorenz[99], N. Lorenzo Martinez[60], M. Losada[163], P. Loscutoff[15], X. Lou[41], A. Lounis[116], J. Love[6], P.A. Love[71], A.J. Lowe[144,e], F. Lu[33a], N. Lu[88], H.J. Lubatti[139], C. Luci[133a,133b], A. Lucotte[55], F. Luehring[60], W. Lukas[61], L. Luminari[133a], O. Lundberg[147a,147b], B. Lund-Jensen[148], M. Lungwitz[82], D. Lynn[25], R. Lysak[126], E. Lytken[80], H. Ma[25], L.L. Ma[33d], G. Maccarrone[47], A. Macchiolo[100], J. Machado Miguens[125a,125b], D. Macina[30], D. Madaffari[84], R. Madar[48], H.J. Maddocks[71], W.F. Mader[44], A. Madsen[167], M. Maeno[8], T. Maeno[25], E. Magradze[54], K. Mahboubi[48], J. Mahlstedt[106], S. Mahmoud[73], C. Maiani[137], C. Maidantchik[24a], A.A. Maier[100], A. Maio[125a,125b,125d], S. Majewski[115], Y. Makida[65], N. Makovec[116], P. Mal[137,x], B. Malaescu[79], Pa. Malecki[39], V.P. Maleev[122], F. Malek[55], U. Mallik[62], D. Malon[6], C. Malone[144], S. Maltezos[10], V.M. Malyshev[108], S. Malyukov[30], J. Mamuzic[13b], B. Mandelli[30], L. Mandelli[90a], I. Mandić[74], R. Mandrysch[62], J. Maneira[125a,125b], A. Manfredini[100], L. Manhaes de Andrade Filho[24b], J.A. Manjarres Ramos[160b], A. Mann[99], P.M. Manning[138], A. Manousakis-Katsikakis[9], B. Mansoulie[137], R. Mantifel[86], L. Mapelli[30], L. March[168], J.F. Marchand[29], G. Marchiori[79], M. Marcisovsky[126], C.P. Marino[170], M. Marjanovic[13a], C.N. Marques[125a], F. Marroquim[24a], S.P. Marsden[83], Z. Marshall[15], L.F. Marti[17], S. Marti-Garcia[168], B. Martin[30], B. Martin[89], T.A. Martin[171], V.J. Martin[46], B. Martin dit Latour[14], H. Martinez[137], M. Martinez[12,n], S. Martin-Haugh[130], A.C. Martyniuk[77], M. Marx[139], F. Marzano[133a], A. Marzin[30], L. Masetti[82], T. Mashimo[156], R. Mashinistov[95], J. Masik[83], A.L. Maslennikov[108], I. Massa[20a,20b], L. Massa[20a,20b], N. Massol[5], P. Mastrandrea[149], A. Mastroberardino[37a,37b], T. Masubuchi[156], P. Mättig[176], J. Mattmann[82], J. Maurer[26a], S.J. Maxfield[73], D.A. Maximov[108,s], R. Mazini[152], L. Mazzaferro[134a,134b], G. Mc Goldrick[159], S.P. Mc Kee[88], A. McCarn[88], R.L. McCarthy[149], T.G. McCarthy[29], N.A. McCubbin[130], K.W. McFarlane[56,∗], J.A. Mcfayden[77], G. Mchedlidze[54], S.J. McMahon[130], R.A. McPherson[170,i], A. Meade[85], J. Mechnich[106], M. Medinnis[42], S. Meehan[31], S. Mehlhase[99], A. Mehta[73], K. Meier[58a], C. Meineck[99], B. Meirose[80], C. Melachrinos[31], B.R. Mellado Garcia[146c], F. Meloni[17], A. Mengarelli[20a,20b], S. Menke[100], E. Meoni[162], K.M. Mercurio[57], S. Mergelmeyer[21], N. Meric[137], P. Mermod[49], L. Merola[103a,103b], C. Meroni[90a], F.S. Merritt[31], H. Merritt[110], A. Messina[30,y], J. Metcalfe[25], A.S. Mete[164], C. Meyer[82], C. Meyer[121], J-P. Meyer[137], J. Meyer[30], R.P. Middleton[130], S. Migas[73], L. Mijović[21], G. Mikenberg[173], M. Mikestikova[126], M. Mikuž[74], A. Milic[30], D.W. Miller[31], C. Mills[46], A. Milov[173], D.A. Milstead[147a,147b], D. Milstein[173], A.A. Minaenko[129], I.A. Minashvili[64], A.I. Mincer[109], B. Mindur[38a], M. Mineev[64], Y. Ming[174], L.M. Mir[12], G. Mirabelli[133a], T. Mitani[172], J. Mitrevski[99], V.A. Mitsou[168], S. Mitsui[65], A. Miucci[49], P.S. Miyagawa[140], J.U. Mjörnmark[80], T. Moa[147a,147b], K. Mochizuki[84], S. Mohapatra[35], W. Mohr[48], S. Molander[147a,147b], R. Moles-Valls[168], K. Mönig[42], C. Monini[55], J. Monk[36], E. Monnier[84], J. Montejo Berlingen[12], F. Monticelli[70], S. Monzani[133a,133b], R.W. Moore[3], A. Moraes[53], N. Morange[62], D. Moreno[82], M. Moreno Llácer[54], P. Morettini[50a], M. Morgenstern[44], M. Morii[57], S. Moritz[82], A.K. Morley[148], G. Mornacchi[30], J.D. Morris[75], L. Morvaj[102], H.G. Moser[100], M. Mosidze[51b], J. Moss[110], K. Motohashi[158], R. Mount[144], E. Mountricha[25], S.V. Mouraviev[95,∗],

E.J.W. Moyse[85], S. Muanza[84], R.D. Mudd[18], F. Mueller[58a], J. Mueller[124], K. Mueller[21], T. Mueller[28], T. Mueller[82], D. Muenstermann[49], Y. Munwes[154], J.A. Murillo Quijada[18], W.J. Murray[171,130], H. Musheghyan[54], E. Musto[153], A.G. Myagkov[129,z], M. Myska[127], O. Nackenhorst[54], J. Nadal[54], K. Nagai[61], R. Nagai[158], Y. Nagai[84], K. Nagano[65], A. Nagarkar[110], Y. Nagasaka[59], M. Nagel[100], A.M. Nairz[30], Y. Nakahama[30], K. Nakamura[65], T. Nakamura[156], I. Nakano[111], H. Namasivayam[41], G. Nanava[21], R. Narayan[58b], T. Nattermann[21], T. Naumann[42], G. Navarro[163], R. Nayyar[7], H.A. Neal[88], P.Yu. Nechaeva[95], T.J. Neep[83], P.D. Nef[144], A. Negri[120a,120b], G. Negri[30], M. Negrini[20a], S. Nektarijevic[49], A. Nelson[164], T.K. Nelson[144], S. Nemecek[126], P. Nemethy[109], A.A. Nepomuceno[24a], M. Nessi[30,aa], M.S. Neubauer[166], M. Neumann[176], R.M. Neves[109], P. Nevski[25], P.R. Newman[18], D.H. Nguyen[6], R.B. Nickerson[119], R. Nicolaidou[137], B. Nicquevert[30], J. Nielsen[138], N. Nikiforou[35], A. Nikiforov[16], V. Nikolaenko[129,z], I. Nikolic-Audit[79], K. Nikolics[49], K. Nikolopoulos[18], P. Nilsson[8], Y. Ninomiya[156], A. Nisati[133a], R. Nisius[100], T. Nobe[158], L. Nodulman[6], M. Nomachi[117], I. Nomidis[29], S. Norberg[112], M. Nordberg[30], O. Novgorodova[44], S. Nowak[100], M. Nozaki[65], L. Nozka[114], K. Ntekas[10], G. Nunes Hanninger[87], T. Nunnemann[99], E. Nurse[77], F. Nuti[87], B.J. O'Brien[46], F. O'grady[7], D.C. O'Neil[143], V. O'Shea[53], F.G. Oakham[29,d], H. Oberlack[100], T. Obermann[21], J. Ocariz[79], A. Ochi[66], M.I. Ochoa[77], S. Oda[69], S. Odaka[65], H. Ogren[60], A. Oh[83], S.H. Oh[45], C.C. Ohm[15], H. Ohman[167], W. Okamura[117], H. Okawa[25], Y. Okumura[31], T. Okuyama[156], A. Olariu[26a], A.G. Olchevski[64], S.A. Olivares Pino[46], D. Oliveira Damazio[25], E. Oliver Garcia[168], A. Olszewski[39], J. Olszowska[39], A. Onofre[125a,125e], P.U.E. Onyisi[31,ab], C.J. Oram[160a], M.J. Oreglia[31], Y. Oren[154], D. Orestano[135a,135b], N. Orlando[72a,72b], C. Oropeza Barrera[53], R.S. Orr[159], B. Osculati[50a,50b], R. Ospanov[121], G. Otero y Garzon[27], H. Otono[69], M. Ouchrif[136d], E.A. Ouellette[170], F. Ould-Saada[118], A. Ouraou[137], K.P. Oussoren[106], Q. Ouyang[33a], A. Ovcharova[15], M. Owen[83], V.E. Ozcan[19a], N. Ozturk[8], K. Pachal[119], A. Pacheco Pages[12], C. Padilla Aranda[12], M. Pagáčová[48], S. Pagan Griso[15], E. Paganis[140], C. Pahl[100], F. Paige[25], P. Pais[85], K. Pajchel[118], G. Palacino[160b], S. Palestini[30], M. Palka[38b], D. Pallin[34], A. Palma[125a,125b], J.D. Palmer[18], Y.B. Pan[174], E. Panagiotopoulou[10], J.G. Panduro Vazquez[76], P. Pani[106], N. Panikashvili[88], S. Panitkin[25], D. Pantea[26a], L. Paolozzi[134a,134b], Th.D. Papadopoulou[10], K. Papageorgiou[155,l], A. Paramonov[6], D. Paredes Hernandez[34], M.A. Parker[28], F. Parodi[50a,50b], J.A. Parsons[35], U. Parzefall[48], E. Pasqualucci[133a], S. Passaggio[50a], A. Passeri[135a], F. Pastore[135a,135b,*], Fr. Pastore[76], G. Pásztor[29], S. Pataraia[176], N.D. Patel[151], J.R. Pater[83], S. Patricelli[103a,103b], T. Pauly[30], J. Pearce[170], M. Pedersen[118], S. Pedraza Lopez[168], R. Pedro[125a,125b], S.V. Peleganchuk[108], D. Pelikan[167], H. Peng[33b], B. Penning[31], J. Penwell[60], D.V. Perepelitsa[25], E. Perez Codina[160a], M.T. Pérez García-Estañ[168], V. Perez Reale[35], L. Perini[90a,90b], H. Pernegger[30], R. Perrino[72a], R. Peschke[42], V.D. Peshekhonov[64], K. Peters[30], R.F.Y. Peters[83], B.A. Petersen[30], T.C. Petersen[36], E. Petit[42], A. Petridis[147a,147b], C. Petridou[155], E. Petrolo[133a], F. Petrucci[135a,135b], N.E. Pettersson[158], R. Pezoa[32b], P.W. Phillips[130], G. Piacquadio[144], E. Pianori[171], A. Picazio[49], E. Piccaro[75], M. Piccinini[20a,20b], R. Piegaia[27], D.T. Pignotti[110], J.E. Pilcher[31], A.D. Pilkington[77], J. Pina[125a,125b,125d], M. Pinamonti[165a,165c,ac], A. Pinder[119], J.L. Pinfold[3], A. Pingel[36], B. Pinto[125a], S. Pires[79], M. Pitt[173], C. Pizio[90a,90b], L. Plazak[145a], M.-A. Pleier[25], V. Pleskot[128], E. Plotnikova[64], P. Plucinski[147a,147b], S. Poddar[58a], F. Podlyski[34], R. Poettgen[82], L. Poggioli[116], D. Pohl[21], M. Pohl[49], G. Polesello[120a], A. Policicchio[37a,37b], R. Polifka[159], A. Polini[20a], C.S. Pollard[45], V. Polychronakos[25], K. Pommès[30], L. Pontecorvo[133a], B.G. Pope[89], G.A. Popeneciu[26b], D.S. Popovic[13a], A. Poppleton[30], X. Portell Bueso[12], S. Pospisil[127], K. Potamianos[15], I.N. Potrap[64], C.J. Potter[150], C.T. Potter[115], G. Poulard[30], J. Poveda[60], V. Pozdnyakov[64], P. Pralavorio[84], A. Pranko[15], S. Prasad[30], R. Pravahan[8], S. Prell[63], D. Price[83], J. Price[73], L.E. Price[6], D. Prieur[124], M. Primavera[72a], M. Proissl[46], K. Prokofiev[47], F. Prokoshin[32b], E. Protopapadaki[137], S. Protopopescu[25], J. Proudfoot[6], M. Przybycien[38a], H. Przysiezniak[5], E. Ptacek[115], D. Puddu[135a,135b], E. Pueschel[85], D. Puldon[149], M. Purohit[25,ad], P. Puzo[116], J. Qian[88], G. Qin[53], Y. Qin[83], A. Quadt[54], D.R. Quarrie[15], W.B. Quayle[165a,165b], M. Queitsch-Maitland[83], D. Quilty[53], A. Qureshi[160b], V. Radeka[25], V. Radescu[42], S.K. Radhakrishnan[149], P. Radloff[115], P. Rados[87], F. Ragusa[90a,90b], G. Rahal[179], S. Rajagopalan[25], M. Rammensee[30], A.S. Randle-Conde[40], C. Rangel-Smith[167], K. Rao[164], F. Rauscher[99], T.C. Rave[48], T. Ravenscroft[53], M. Raymond[30], A.L. Read[118], N.P. Readioff[73], D.M. Rebuzzi[120a,120b], A. Redelbach[175], G. Redlinger[25], R. Reece[138], K. Reeves[41], L. Rehnisch[16], H. Reisin[27], M. Relich[164], C. Rembser[30], H. Ren[33a], Z.L. Ren[152], A. Renaud[116], M. Rescigno[133a], S. Resconi[90a], O.L. Rezanova[108,s], P. Reznicek[128], R. Rezvani[94], R. Richter[100], M. Ridel[79], P. Rieck[16], J. Rieger[54], M. Rijssenbeek[149], A. Rimoldi[120a,120b], L. Rinaldi[20a], E. Ritsch[61], I. Riu[12], F. Rizatdinova[113], E. Rizvi[75], S.H. Robertson[86,i], A. Robichaud-Veronneau[86], D. Robinson[28], J.E.M. Robinson[83], A. Robson[53], C. Roda[123a,123b], L. Rodrigues[30], S. Roe[30], O. Røhne[118], S. Rolli[162], A. Romaniouk[97], M. Romano[20a,20b], E. Romero Adam[168], N. Rompotis[139], M. Ronzani[48], L. Roos[79], E. Ros[168], S. Rosati[133a], K. Rosbach[49], M. Rose[76], P. Rose[138], P.L. Rosendahl[14], O. Rosenthal[142], V. Rossetti[147a,147b], E. Rossi[103a,103b], L.P. Rossi[50a], R. Rosten[139], M. Rotaru[26a], I. Roth[173], J. Rothberg[139], D. Rousseau[116], C.R. Royon[137], A. Rozanov[84], Y. Rozen[153], X. Ruan[146c], F. Rubbo[12], I. Rubinskiy[42], V.I. Rud[98], C. Rudolph[44], M.S. Rudolph[159], F. Rühr[48], A. Ruiz-Martinez[30], Z. Rurikova[48], N.A. Rusakovich[64], A. Ruschke[99], J.P. Rutherfoord[7], N. Ruthmann[48], Y.F. Ryabov[122], M. Rybar[128], G. Rybkin[116], N.C. Ryder[119], A.F. Saavedra[151], S. Sacerdoti[27], A. Saddique[3], I. Sadeh[154], H.F-W. Sadrozinski[138], R. Sadykov[64], F. Safai Tehrani[133a], H. Sakamoto[156], Y. Sakurai[172], G. Salamanna[135a,135b], A. Salamon[134a], M. Saleem[112], D. Salek[106], P.H. Sales De Bruin[139], D. Salihagic[100], A. Salnikov[144], J. Salt[168], D. Salvatore[37a,37b], F. Salvatore[150], A. Salvucci[105], A. Salzburger[30], D. Sampsonidis[155], A. Sanchez[103a,103b], J. Sánchez[168], V. Sanchez Martinez[168], H. Sandaker[14], R.L. Sandbach[75], H.G. Sander[82], M.P. Sanders[99], M. Sandhoff[176], T. Sandoval[28], C. Sandoval[163], R. Sandstroem[100], D.P.C. Sankey[130], A. Sansoni[47], C. Santoni[34], R. Santonico[134a,134b], H. Santos[125a], I. Santoyo Castillo[150], K. Sapp[124], A. Sapronov[64], J.G. Saraiva[125a,125d], B. Sarrazin[21], G. Sartisohn[176], O. Sasaki[65], Y. Sasaki[156], G. Sauvage[5,*],

E. Sauvan[5], P. Savard[159,d], D.O. Savu[30], C. Sawyer[119], L. Sawyer[78,m], D.H. Saxon[53], J. Saxon[121], C. Sbarra[20a], A. Sbrizzi[3],
T. Scanlon[77], D.A. Scannicchio[164], M. Scarcella[151], V. Scarfone[37a,37b], J. Schaarschmidt[173], P. Schacht[100], D. Schaefer[30],
R. Schaefer[42], S. Schaepe[21], S. Schaetzel[58b], U. Schäfer[82], A.C. Schaffer[116], D. Schaile[99], R.D. Schamberger[149], V. Scharf[58a],
V.A. Schegelsky[122], D. Scheirich[128], M. Schernau[164], M.I. Scherzer[35], C. Schiavi[50a,50b], J. Schieck[99], C. Schillo[48],
M. Schioppa[37a,37b], S. Schlenker[30], E. Schmidt[48], K. Schmieden[30], C. Schmitt[82], S. Schmitt[58b], B. Schneider[17],
Y.J. Schnellbach[73], U. Schnoor[44], L. Schoeffel[137], A. Schoening[58b], B.D. Schoenrock[89], A.L.S. Schorlemmer[54], M. Schott[82],
D. Schouten[160a], J. Schovancova[25], S. Schramm[159], M. Schreyer[175], C. Schroeder[82], N. Schuh[82], M.J. Schultens[21],
H.-C. Schultz-Coulon[58a], H. Schulz[16], M. Schumacher[48], B.A. Schumm[138], Ph. Schune[137], C. Schwanenberger[83],
A. Schwartzman[144], Ph. Schwegler[100], Ph. Schwemling[137], R. Schwienhorst[89], J. Schwindling[137], T. Schwindt[21],
M. Schwoerer[5], F.G. Sciacca[17], E. Scifo[116], G. Sciolla[23], W.G. Scott[130], F. Scuri[123a,123b], F. Scutti[21], J. Searcy[88], G. Sedov[42],
E. Sedykh[122], S.C. Seidel[104], A. Seiden[138], F. Seifert[127], J.M. Seixas[24a], G. Sekhniaidze[103a], S.J. Sekula[40], K.E. Selbach[46],
D.M. Seliverstov[122,*], G. Sellers[73], N. Semprini-Cesari[20a,20b], C. Serfon[30], L. Serin[116], L. Serkin[54], T. Serre[84], R. Seuster[160a],
H. Severini[112], T. Sfiligoj[74], F. Sforza[100], A. Sfyrla[30], E. Shabalina[54], M. Shamim[115], L.Y. Shan[33a], R. Shang[166], J.T. Shank[22],
M. Shapiro[15], P.B. Shatalov[96], K. Shaw[165a,165b], C.Y. Shehu[150], P. Sherwood[77], L. Shi[152,ae], S. Shimizu[66], C.O. Shimmin[164],
M. Shimojima[101], M. Shiyakova[64], A. Shmeleva[95], M.J. Shochet[31], D. Short[119], S. Shrestha[63], E. Shulga[97], M.A. Shupe[7],
S. Shushkevich[42], P. Sicho[126], O. Sidiropoulou[155], D. Sidorov[113], A. Sidoti[133a], F. Siegert[44], Dj. Sijacki[13a], J. Silva[125a,125d],
Y. Silver[154], D. Silverstein[144], S.B. Silverstein[147a], V. Simak[127], O. Simard[5], Lj. Simic[13a], S. Simion[116], E. Simioni[82],
B. Simmons[77], R. Simoniello[90a,90b], M. Simonyan[36], P. Sinervo[159], N.B. Sinev[115], V. Sipica[142], G. Siragusa[175], A. Sircar[78],
A.N. Sisakyan[64,*], S.Yu. Sivoklokov[98], J. Sjölin[147a,147b], T.B. Sjursen[14], H.P. Skottowe[57], K.Yu. Skovpen[108], P. Skubic[112],
M. Slater[18], T. Slavicek[127], K. Sliwa[162], V. Smakhtin[173], B.H. Smart[46], L. Smestad[14], S.Yu. Smirnov[97], Y. Smirnov[97],
L.N. Smirnova[98,af], O. Smirnova[80], K.M. Smith[53], M. Smizanska[71], K. Smolek[127], A.A. Snesarev[95], G. Snidero[75],
S. Snyder[25], R. Sobie[170,i], F. Socher[44], A. Soffer[154], D.A. Soh[152,ae], C.A. Solans[30], M. Solar[127], J. Solc[127], E.Yu. Soldatov[97],
U. Soldevila[168], A.A. Solodkov[129], A. Soloshenko[64], O.V. Solovyanov[129], V. Solovyev[122], P. Sommer[48], H.Y. Song[33b],
N. Soni[1], A. Sood[15], A. Sopczak[127], B. Sopko[127], V. Sopko[127], V. Sorin[12], M. Sosebee[8], R. Soualah[165a,165c], P. Soueid[94],
A.M. Soukharev[108], D. South[42], S. Spagnolo[72a,72b], F. Spanò[76], W.R. Spearman[57], F. Spettel[100], R. Spighi[20a], G. Spigo[30],
L.A. Spiller[87], M. Spousta[128], T. Spreitzer[159], B. Spurlock[8], R.D. St. Denis[53,*], S. Staerz[44], J. Stahlman[121], R. Stamen[58a],
S. Stamm[16], E. Stanecka[39], R.W. Stanek[6], C. Stanescu[135a], M. Stanescu-Bellu[42], M.M. Stanitzki[42], S. Stapnes[118],
E.A. Starchenko[129], J. Stark[55], P. Staroba[126], P. Starovoitov[42], R. Staszewski[39], P. Stavina[145a,*], P. Steinberg[25], B. Stelzer[143],
H.J. Stelzer[30], O. Stelzer-Chilton[160a], H. Stenzel[52], S. Stern[100], G.A. Stewart[53], J.A. Stillings[21], M.C. Stockton[86], M. Stoebe[86],
G. Stoicea[26a], P. Stolte[54], S. Stonjek[100], A.R. Stradling[8], A. Straessner[44], M.E. Stramaglia[17], J. Strandberg[148],
S. Strandberg[147a,147b], A. Strandlie[118], E. Strauss[144], M. Strauss[112], P. Strizenec[145b], R. Ströhmer[175], D.M. Strom[115],
R. Stroynowski[40], S.A. Stucci[17], B. Stugu[14], N.A. Styles[42], D. Su[144], J. Su[124], R. Subramaniam[78], A. Succurro[12], Y. Sugaya[117],
C. Suhr[107], M. Suk[127], V.V. Sulin[95], S. Sultansoy[4c], T. Sumida[67], S. Sun[57], X. Sun[33a], J.E. Sundermann[48], K. Suruliz[140],
G. Susinno[37a,37b], M.R. Sutton[150], Y. Suzuki[65], M. Svatos[126], S. Swedish[169], M. Swiatlowski[144], I. Sykora[145a], T. Sykora[128],
D. Ta[89], C. Taccini[135a,135b], K. Tackmann[42], J. Taenzer[159], A. Taffard[164], R. Tafirout[160a], N. Taiblum[154], H. Takai[25],
R. Takashima[68], H. Takeda[66], T. Takeshita[141], Y. Takubo[65], M. Talby[84], A.A. Talyshev[108,s], J.Y.C. Tam[175], K.G. Tan[87],
J. Tanaka[156], R. Tanaka[116], S. Tanaka[132], S. Tanaka[65], A.J. Tanasijczuk[143], B.B. Tannenwald[110], N. Tannoury[21],
S. Tapprogge[82], S. Tarem[153], F. Tarrade[29], G.F. Tartarelli[90a], P. Tas[128], M. Tasevsky[126], T. Tashiro[67], E. Tassi[37a,37b],
A. Tavares Delgado[125a,125b], Y. Tayalati[136d], F.E. Taylor[93], G.N. Taylor[87], W. Taylor[160b], F.A. Teischinger[30],
M. Teixeira Dias Castanheira[75], P. Teixeira-Dias[76], K.K. Temming[48], H. Ten Kate[30], P.K. Teng[152], J.J. Teoh[117], S. Terada[65],
K. Terashi[156], J. Terron[81], S. Terzo[100], M. Testa[47], R.J. Teuscher[159,i], J. Therhaag[21], T. Theveneaux-Pelzer[34], J.P. Thomas[18],
J. Thomas-Wilsker[76], E.N. Thompson[35], P.D. Thompson[18], P.D. Thompson[159], A.S. Thompson[53], L.A. Thomsen[36],
E. Thomson[121], M. Thomson[28], W.M. Thong[87], R.P. Thun[88,*], F. Tian[35], M.J. Tibbetts[15], V.O. Tikhomirov[95,ag],
Yu.A. Tikhonov[108,s], S. Timoshenko[97], E. Tiouchichine[84], P. Tipton[177], S. Tisserant[84], T. Todorov[5], S. Todorova-Nova[128],
B. Toggerson[7], J. Tojo[69], S. Tokár[145a], K. Tokushuku[65], K. Tollefson[89], L. Tomlinson[83], M. Tomoto[102], L. Tompkins[31],
K. Toms[104], N.D. Topilin[64], E. Torrence[115], H. Torres[143], E. Torró Pastor[168], J. Toth[84,ah], F. Touchard[84], D.R. Tovey[140],
H.L. Tran[116], T. Trefzger[175], L. Tremblet[30], A. Tricoli[30], I.M. Trigger[160a], S. Trincaz-Duvoid[79], M.F. Tripiana[12],
W. Trischuk[159], B. Trocmé[55], C. Troncon[90a], M. Trottier-McDonald[143], M. Trovatelli[135a,135b], P. True[89], M. Trzebinski[39],
A. Trzupek[39], C. Tsarouchas[30], J.C-L. Tseng[119], P.V. Tsiareshka[91], D. Tsionou[137], G. Tsipolitis[10], N. Tsirintanis[9],
S. Tsiskaridze[12], V. Tsiskaridze[48], E.G. Tskhadadze[51a], I.I. Tsukerman[96], V. Tsulaia[15], S. Tsuno[65], D. Tsybychev[149],
A. Tudorache[26a], V. Tudorache[26a], A.N. Tuna[121], S.A. Tupputi[20a,20b], S. Turchikhin[98,af], D. Turecek[127], I. Turk Cakir[4d],
R. Turra[90a,90b], P.M. Tuts[35], A. Tykhonov[49], M. Tylmad[147a,147b], M. Tyndel[130], K. Uchida[21], I. Ueda[156], R. Ueno[29],
M. Ughetto[84], M. Ugland[14], M. Uhlenbrock[21], F. Ukegawa[161], G. Unal[30], A. Undrus[25], G. Unel[164], F.C. Ungaro[48], Y. Unno[65],
C. Unverdorben[99], D. Urbaniec[35], P. Urquijo[87], G. Usai[8], A. Usanova[61], L. Vacavant[84], V. Vacek[127], B. Vachon[86],
N. Valencic[106], S. Valentinetti[20a,20b], A. Valero[168], L. Valery[34], S. Valkar[128], E. Valladolid Gallego[168], S. Vallecorsa[49],
J.A. Valls Ferrer[168], W. Van Den Wollenberg[106], P.C. Van Der Deijl[106], R. van der Geer[106], H. van der Graaf[106],
R. Van Der Leeuw[106], D. van der Ster[30], N. van Eldik[30], P. van Gemmeren[6], J. Van Nieuwkoop[143], I. van Vulpen[106],
M.C. van Woerden[30], M. Vanadia[133a,133b], W. Vandelli[30], R. Vanguri[121], A. Vaniachine[6], P. Vankov[42], F. Vannucci[79],

G. Vardanyan[178], R. Vari[133a], E.W. Varnes[7], T. Varol[85], D. Varouchas[79], A. Vartapetian[8], K.E. Varvell[151], F. Vazeille[34], T. Vazquez Schroeder[54], J. Veatch[7], F. Veloso[125a,125c], S. Veneziano[133a], A. Ventura[72a,72b], D. Ventura[85], M. Venturi[170], N. Venturi[159], A. Venturini[23], V. Vercesi[120a], M. Verducci[133a,133b], W. Verkerke[106], J.C. Vermeulen[106], A. Vest[44], M.C. Vetterli[143,d], O. Viazlo[80], I. Vichou[166], T. Vickey[146c,ai], O.E. Vickey Boeriu[146c], G.H.A. Viehhauser[119], S. Viel[169], R. Vigne[30], M. Villa[20a,20b], M. Villaplana Perez[90a,90b], E. Vilucchi[47], M.G. Vincter[29], V.B. Vinogradov[64], J. Virzi[15], I. Vivarelli[150], F. Vives Vaque[3], S. Vlachos[10], D. Vladoiu[99], M. Vlasak[127], A. Vogel[21], M. Vogel[32a], P. Vokac[127], G. Volpi[123a,123b], M. Volpi[87], H. von der Schmitt[100], H. von Radziewski[48], E. von Toerne[21], V. Vorobel[128], K. Vorobev[97], M. Vos[168], R. Voss[30], J.H. Vossebeld[73], N. Vranjes[137], M. Vranjes Milosavljevic[106], V. Vrba[126], M. Vreeswijk[106], T. Vu Anh[48], R. Vuillermet[30], I. Vukotic[31], Z. Vykydal[127], P. Wagner[21], W. Wagner[176], H. Wahlberg[70], S. Wahrmund[44], J. Wakabayashi[102], J. Walder[71], R. Walker[99], W. Walkowiak[142], R. Wall[177], P. Waller[73], B. Walsh[177], C. Wang[152,aj], C. Wang[45], F. Wang[174], H. Wang[15], H. Wang[40], J. Wang[42], J. Wang[33a], K. Wang[86], R. Wang[104], S.M. Wang[152], T. Wang[21], X. Wang[177], C. Wanotayaroj[115], A. Warburton[86], C.P. Ward[28], D.R. Wardrope[77], M. Warsinsky[48], A. Washbrook[46], C. Wasicki[42], P.M. Watkins[18], A.T. Watson[18], I.J. Watson[151], M.F. Watson[18], G. Watts[139], S. Watts[83], B.M. Waugh[77], S. Webb[83], M.S. Weber[17], S.W. Weber[175], J.S. Webster[31], A.R. Weidberg[119], P. Weigell[100], B. Weinert[60], J. Weingarten[54], C. Weiser[48], H. Weits[106], P.S. Wells[30], T. Wenaus[25], D. Wendland[16], Z. Weng[152,ae], T. Wengler[30], S. Wenig[30], N. Wermes[21], M. Werner[48], P. Werner[30], M. Wessels[58a], J. Wetter[162], K. Whalen[29], A. White[8], M.J. White[1], R. White[32b], S. White[123a,123b], D. Whiteson[164], D. Wicke[176], F.J. Wickens[130], W. Wiedenmann[174], M. Wielers[130], P. Wienemann[21], C. Wiglesworth[36], L.A.M. Wiik-Fuchs[21], P.A. Wijeratne[77], A. Wildauer[100], M.A. Wildt[42,ak], H.G. Wilkens[30], J.Z. Will[99], H.H. Williams[121], S. Williams[28], C. Willis[89], S. Willocq[85], A. Wilson[88], J.A. Wilson[18], I. Wingerter-Seez[5], F. Winklmeier[115], B.T. Winter[21], M. Wittgen[144], T. Wittig[43], J. Wittkowski[99], S.J. Wollstadt[82], M.W. Wolter[39], H. Wolters[125a,125c], B.K. Wosiek[39], J. Wotschack[30], M.J. Woudstra[83], K.W. Wozniak[39], M. Wright[53], M. Wu[55], S.L. Wu[174], X. Wu[49], Y. Wu[88], E. Wulf[35], T.R. Wyatt[83], B.M. Wynne[46], S. Xella[36], M. Xiao[137], D. Xu[33a], L. Xu[33b,al], B. Yabsley[151], S. Yacoob[146b,am], R. Yakabe[66], M. Yamada[65], H. Yamaguchi[156], Y. Yamaguchi[117], A. Yamamoto[65], K. Yamamoto[63], S. Yamamoto[156], T. Yamamura[156], T. Yamanaka[156], K. Yamauchi[102], Y. Yamazaki[66], Z. Yan[22], H. Yang[33e], H. Yang[174], U.K. Yang[83], Y. Yang[110], S. Yanush[92], L. Yao[33a], W-M. Yao[15], Y. Yasu[65], E. Yatsenko[42], K.H. Yau Wong[21], J. Ye[40], S. Ye[25], A.L. Yen[57], E. Yildirim[42], M. Yilmaz[4b], R. Yoosoofmiya[124], K. Yorita[172], R. Yoshida[6], K. Yoshihara[156], C. Young[144], C.J.S. Young[30], S. Youssef[22], D.R. Yu[15], J. Yu[8], J.M. Yu[88], J. Yu[113], L. Yuan[66], A. Yurkewicz[107], I. Yusuff[28,an], B. Zabinski[39], R. Zaidan[62], A.M. Zaitsev[129,z], A. Zaman[149], S. Zambito[23], L. Zanello[133a,133b], D. Zanzi[100], C. Zeitnitz[176], M. Zeman[127], A. Zemla[38a], K. Zengel[23], O. Zenin[129], T. Ženiš[145a], D. Zerwas[116], G. Zevi della Porta[57], D. Zhang[88], F. Zhang[174], H. Zhang[89], J. Zhang[6], L. Zhang[152], X. Zhang[33d], Z. Zhang[116], Z. Zhao[33b], A. Zhemchugov[64], J. Zhong[119], B. Zhou[88], L. Zhou[35], N. Zhou[164], C.G. Zhu[33d], H. Zhu[33a], J. Zhu[88], Y. Zhu[33b], X. Zhuang[33a], K. Zhukov[95], A. Zibell[175], D. Zieminska[60], N.I. Zimine[64], C. Zimmermann[82], R. Zimmermann[21], S. Zimmermann[21], S. Zimmermann[48], Z. Zinonos[54], M. Ziolkowski[142], G. Zobernig[174], A. Zoccoli[20a,20b], M. zur Nedden[16], G. Zurzolo[103a,103b], V. Zutshi[107], L. Zwalinski[30].

[1] Department of Physics, University of Adelaide, Adelaide, Australia

[2] Physics Department, SUNY Albany, Albany NY, United States of America

[3] Department of Physics, University of Alberta, Edmonton AB, Canada

[4] [(a)] Department of Physics, Ankara University, Ankara; [(b)] Department of Physics, Gazi University, Ankara; [(c)] Division of Physics, TOBB University of Economics and Technology, Ankara; [(d)] Turkish Atomic Energy Authority, Ankara, Turkey

[5] LAPP, CNRS/IN2P3 and Université de Savoie, Annecy-le-Vieux, France

[6] High Energy Physics Division, Argonne National Laboratory, Argonne IL, United States of America

[7] Department of Physics, University of Arizona, Tucson AZ, United States of America

[8] Department of Physics, The University of Texas at Arlington, Arlington TX, United States of America

[9] Physics Department, University of Athens, Athens, Greece

[10] Physics Department, National Technical University of Athens, Zografou, Greece

[11] Institute of Physics, Azerbaijan Academy of Sciences, Baku, Azerbaijan

[12] Institut de Física d'Altes Energies and Departament de Física de la Universitat Autònoma de Barcelona, Barcelona, Spain

[13] [(a)] Institute of Physics, University of Belgrade, Belgrade; [(b)] Vinca Institute of Nuclear Sciences, University of Belgrade, Belgrade, Serbia

[14] Department for Physics and Technology, University of Bergen, Bergen, Norway

[15] Physics Division, Lawrence Berkeley National Laboratory and University of California, Berkeley CA, United States of America

[16] Department of Physics, Humboldt University, Berlin, Germany

[17] Albert Einstein Center for Fundamental Physics and Laboratory for High Energy Physics, University of Bern, Bern, Switzerland

[18] School of Physics and Astronomy, University of Birmingham, Birmingham, United Kingdom

[19] [(a)] Department of Physics, Bogazici University, Istanbul; [(b)] Department of Physics, Dogus University, Istanbul; [(c)] Department of Physics Engineering, Gaziantep University, Gaziantep, Turkey

20 [(a)] INFN Sezione di Bologna; [(b)] Dipartimento di Fisica e Astronomia, Università di Bologna, Bologna, Italy

21 Physikalisches Institut, University of Bonn, Bonn, Germany

22 Department of Physics, Boston University, Boston MA, United States of America

23 Department of Physics, Brandeis University, Waltham MA, United States of America

24 [(a)] Universidade Federal do Rio De Janeiro COPPE/EE/IF, Rio de Janeiro; [(b)] Federal University of Juiz de Fora (UFJF), Juiz de Fora; [(c)] Federal University of Sao Joao del Rei (UFSJ), Sao Joao del Rei; [(d)] Instituto de Fisica, Universidade de Sao Paulo, Sao Paulo, Brazil

25 Physics Department, Brookhaven National Laboratory, Upton NY, United States of America

26 [(a)] National Institute of Physics and Nuclear Engineering, Bucharest; [(b)] National Institute for Research and Development of Isotopic and Molecular Technologies, Physics Department, Cluj Napoca; [(c)] University Politehnica Bucharest, Bucharest; [(d)] West University in Timisoara, Timisoara, Romania

27 Departamento de Física, Universidad de Buenos Aires, Buenos Aires, Argentina

28 Cavendish Laboratory, University of Cambridge, Cambridge, United Kingdom

29 Department of Physics, Carleton University, Ottawa ON, Canada

30 CERN, Geneva, Switzerland

31 Enrico Fermi Institute, University of Chicago, Chicago IL, United States of America

32 [(a)] Departamento de Física, Pontificia Universidad Católica de Chile, Santiago; [(b)] Departamento de Física, Universidad Técnica Federico Santa María, Valparaíso, Chile

33 [(a)] Institute of High Energy Physics, Chinese Academy of Sciences, Beijing; [(b)] Department of Modern Physics, University of Science and Technology of China, Anhui; [(c)] Department of Physics, Nanjing University, Jiangsu; [(d)] School of Physics, Shandong University, Shandong; [(e)] Physics Department, Shanghai Jiao Tong University, Shanghai, China

34 Laboratoire de Physique Corpusculaire, Clermont Université and Université Blaise Pascal and CNRS/IN2P3, Clermont-Ferrand, France

35 Nevis Laboratory, Columbia University, Irvington NY, United States of America

36 Niels Bohr Institute, University of Copenhagen, Kobenhavn, Denmark

37 [(a)] INFN Gruppo Collegato di Cosenza, Laboratori Nazionali di Frascati; [(b)] Dipartimento di Fisica, Università della Calabria, Rende, Italy

38 [(a)] AGH University of Science and Technology, Faculty of Physics and Applied Computer Science, Krakow; [(b)] Marian Smoluchowski Institute of Physics, Jagiellonian University, Krakow, Poland

39 The Henryk Niewodniczanski Institute of Nuclear Physics, Polish Academy of Sciences, Krakow, Poland

40 Physics Department, Southern Methodist University, Dallas TX, United States of America

41 Physics Department, University of Texas at Dallas, Richardson TX, United States of America

42 DESY, Hamburg and Zeuthen, Germany

43 Institut für Experimentelle Physik IV, Technische Universität Dortmund, Dortmund, Germany

44 Institut für Kern- und Teilchenphysik, Technische Universität Dresden, Dresden, Germany

45 Department of Physics, Duke University, Durham NC, United States of America

46 SUPA - School of Physics and Astronomy, University of Edinburgh, Edinburgh, United Kingdom

47 INFN Laboratori Nazionali di Frascati, Frascati, Italy

48 Fakultät für Mathematik und Physik, Albert-Ludwigs-Universität, Freiburg, Germany

49 Section de Physique, Université de Genève, Geneva, Switzerland

50 [(a)] INFN Sezione di Genova; [(b)] Dipartimento di Fisica, Università di Genova, Genova, Italy

51 [(a)] E. Andronikashvili Institute of Physics, Iv. Javakhishvili Tbilisi State University, Tbilisi; [(b)] High Energy Physics Institute, Tbilisi State University, Tbilisi, Georgia

52 II Physikalisches Institut, Justus-Liebig-Universität Giessen, Giessen, Germany

53 SUPA - School of Physics and Astronomy, University of Glasgow, Glasgow, United Kingdom

54 II Physikalisches Institut, Georg-August-Universität, Göttingen, Germany

55 Laboratoire de Physique Subatomique et de Cosmologie, Université Grenoble-Alpes, CNRS/IN2P3, Grenoble, France

56 Department of Physics, Hampton University, Hampton VA, United States of America

57 Laboratory for Particle Physics and Cosmology, Harvard University, Cambridge MA, United States of America

58 [(a)] Kirchhoff-Institut für Physik, Ruprecht-Karls-Universität Heidelberg, Heidelberg; [(b)] Physikalisches Institut, Ruprecht-Karls-Universität Heidelberg, Heidelberg; [(c)] ZITI Institut für technische Informatik, Ruprecht-Karls-Universität Heidelberg, Mannheim, Germany

59 Faculty of Applied Information Science, Hiroshima Institute of Technology, Hiroshima, Japan

60 Department of Physics, Indiana University, Bloomington IN, United States of America

61 Institut für Astro- und Teilchenphysik, Leopold-Franzens-Universität, Innsbruck, Austria

62 University of Iowa, Iowa City IA, United States of America

63 Department of Physics and Astronomy, Iowa State University, Ames IA, United States of America

64 Joint Institute for Nuclear Research, JINR Dubna, Dubna, Russia

[65] KEK, High Energy Accelerator Research Organization, Tsukuba, Japan

[66] Graduate School of Science, Kobe University, Kobe, Japan

[67] Faculty of Science, Kyoto University, Kyoto, Japan

[68] Kyoto University of Education, Kyoto, Japan

[69] Department of Physics, Kyushu University, Fukuoka, Japan

[70] Instituto de Física La Plata, Universidad Nacional de La Plata and CONICET, La Plata, Argentina

[71] Physics Department, Lancaster University, Lancaster, United Kingdom

[72] [a] INFN Sezione di Lecce; [b] Dipartimento di Matematica e Fisica, Università del Salento, Lecce, Italy

[73] Oliver Lodge Laboratory, University of Liverpool, Liverpool, United Kingdom

[74] Department of Physics, Jožef Stefan Institute and University of Ljubljana, Ljubljana, Slovenia

[75] School of Physics and Astronomy, Queen Mary University of London, London, United Kingdom

[76] Department of Physics, Royal Holloway University of London, Surrey, United Kingdom

[77] Department of Physics and Astronomy, University College London, London, United Kingdom

[78] Louisiana Tech University, Ruston LA, United States of America

[79] Laboratoire de Physique Nucléaire et de Hautes Energies, UPMC and Université Paris-Diderot and CNRS/IN2P3, Paris, France

[80] Fysiska institutionen, Lunds universitet, Lund, Sweden

[81] Departamento de Fisica Teorica C-15, Universidad Autonoma de Madrid, Madrid, Spain

[82] Institut für Physik, Universität Mainz, Mainz, Germany

[83] School of Physics and Astronomy, University of Manchester, Manchester, United Kingdom

[84] CPPM, Aix-Marseille Université and CNRS/IN2P3, Marseille, France

[85] Department of Physics, University of Massachusetts, Amherst MA, United States of America

[86] Department of Physics, McGill University, Montreal QC, Canada

[87] School of Physics, University of Melbourne, Victoria, Australia

[88] Department of Physics, The University of Michigan, Ann Arbor MI, United States of America

[89] Department of Physics and Astronomy, Michigan State University, East Lansing MI, United States of America

[90] [a] INFN Sezione di Milano; [b] Dipartimento di Fisica, Università di Milano, Milano, Italy

[91] B.I. Stepanov Institute of Physics, National Academy of Sciences of Belarus, Minsk, Republic of Belarus

[92] National Scientific and Educational Centre for Particle and High Energy Physics, Minsk, Republic of Belarus

[93] Department of Physics, Massachusetts Institute of Technology, Cambridge MA, United States of America

[94] Group of Particle Physics, University of Montreal, Montreal QC, Canada

[95] P.N. Lebedev Institute of Physics, Academy of Sciences, Moscow, Russia

[96] Institute for Theoretical and Experimental Physics (ITEP), Moscow, Russia

[97] Moscow Engineering and Physics Institute (MEPhI), Moscow, Russia

[98] D.V.Skobeltsyn Institute of Nuclear Physics, M.V.Lomonosov Moscow State University, Moscow, Russia

[99] Fakultät für Physik, Ludwig-Maximilians-Universität München, München, Germany

[100] Max-Planck-Institut für Physik (Werner-Heisenberg-Institut), München, Germany

[101] Nagasaki Institute of Applied Science, Nagasaki, Japan

[102] Graduate School of Science and Kobayashi-Maskawa Institute, Nagoya University, Nagoya, Japan

[103] [a] INFN Sezione di Napoli; [b] Dipartimento di Fisica, Università di Napoli, Napoli, Italy

[104] Department of Physics and Astronomy, University of New Mexico, Albuquerque NM, United States of America

[105] Institute for Mathematics, Astrophysics and Particle Physics, Radboud University Nijmegen/Nikhef, Nijmegen, Netherlands

[106] Nikhef National Institute for Subatomic Physics and University of Amsterdam, Amsterdam, Netherlands

[107] Department of Physics, Northern Illinois University, DeKalb IL, United States of America

[108] Budker Institute of Nuclear Physics, SB RAS, Novosibirsk, Russia

[109] Department of Physics, New York University, New York NY, United States of America

[110] Ohio State University, Columbus OH, United States of America

[111] Faculty of Science, Okayama University, Okayama, Japan

[112] Homer L. Dodge Department of Physics and Astronomy, University of Oklahoma, Norman OK, United States of America

[113] Department of Physics, Oklahoma State University, Stillwater OK, United States of America

[114] Palacký University, RCPTM, Olomouc, Czech Republic

[115] Center for High Energy Physics, University of Oregon, Eugene OR, United States of America

[116] LAL, Université Paris-Sud and CNRS/IN2P3, Orsay, France

[117] Graduate School of Science, Osaka University, Osaka, Japan

[118] Department of Physics, University of Oslo, Oslo, Norway

[119] Department of Physics, Oxford University, Oxford, United Kingdom

[120] [a] INFN Sezione di Pavia; [b] Dipartimento di Fisica, Università di Pavia, Pavia, Italy

[121] Department of Physics, University of Pennsylvania, Philadelphia PA, United States of America

[122] Petersburg Nuclear Physics Institute, Gatchina, Russia

[123] [a] INFN Sezione di Pisa; [b] Dipartimento di Fisica E. Fermi, Università di Pisa, Pisa, Italy

[124] Department of Physics and Astronomy, University of Pittsburgh, Pittsburgh PA, United States of America

[125] [a] Laboratorio de Instrumentacao e Fisica Experimental de Particulas - LIP, Lisboa; [b] Faculdade de Ciências, Universidade de Lisboa, Lisboa; [c] Department of Physics, University of Coimbra, Coimbra; [d] Centro de Física Nuclear da Universidade de Lisboa, Lisboa; [e] Departamento de Fisica, Universidade do Minho, Braga; [f] Departamento de Fisica Teorica y del Cosmos and CAFPE, Universidad de Granada, Granada (Spain); [g] Dep Fisica and CEFITEC of Faculdade de Ciencias e Tecnologia, Universidade Nova de Lisboa, Caparica, Portugal

[126] Institute of Physics, Academy of Sciences of the Czech Republic, Praha, Czech Republic

[127] Czech Technical University in Prague, Praha, Czech Republic

[128] Faculty of Mathematics and Physics, Charles University in Prague, Praha, Czech Republic

[129] State Research Center Institute for High Energy Physics, Protvino, Russia

[130] Particle Physics Department, Rutherford Appleton Laboratory, Didcot, United Kingdom

[131] Physics Department, University of Regina, Regina SK, Canada

[132] Ritsumeikan University, Kusatsu, Shiga, Japan

[133] [a] INFN Sezione di Roma; [b] Dipartimento di Fisica, Sapienza Università di Roma, Roma, Italy

[134] [a] INFN Sezione di Roma Tor Vergata; [b] Dipartimento di Fisica, Università di Roma Tor Vergata, Roma, Italy

[135] [a] INFN Sezione di Roma Tre; [b] Dipartimento di Matematica e Fisica, Università Roma Tre, Roma, Italy

[136] [a] Faculté des Sciences Ain Chock, Réseau Universitaire de Physique des Hautes Energies - Université Hassan II, Casablanca; [b] Centre National de l'Energie des Sciences Techniques Nucleaires, Rabat; [c] Faculté des Sciences Semlalia, Université Cadi Ayyad, LPHEA-Marrakech; [d] Faculté des Sciences, Université Mohamed Premier and LPTPM, Oujda; [e] Faculté des sciences, Université Mohammed V-Agdal, Rabat, Morocco

[137] DSM/IRFU (Institut de Recherches sur les Lois Fondamentales de l'Univers), CEA Saclay (Commissariat à l'Energie Atomique et aux Energies Alternatives), Gif-sur-Yvette, France

[138] Santa Cruz Institute for Particle Physics, University of California Santa Cruz, Santa Cruz CA, United States of America

[139] Department of Physics, University of Washington, Seattle WA, United States of America

[140] Department of Physics and Astronomy, University of Sheffield, Sheffield, United Kingdom

[141] Department of Physics, Shinshu University, Nagano, Japan

[142] Fachbereich Physik, Universität Siegen, Siegen, Germany

[143] Department of Physics, Simon Fraser University, Burnaby BC, Canada

[144] SLAC National Accelerator Laboratory, Stanford CA, United States of America

[145] [a] Faculty of Mathematics, Physics & Informatics, Comenius University, Bratislava; [b] Department of Subnuclear Physics, Institute of Experimental Physics of the Slovak Academy of Sciences, Kosice, Slovak Republic

[146] [a] Department of Physics, University of Cape Town, Cape Town; [b] Department of Physics, University of Johannesburg, Johannesburg; [c] School of Physics, University of the Witwatersrand, Johannesburg, South Africa

[147] [a] Department of Physics, Stockholm University; [b] The Oskar Klein Centre, Stockholm, Sweden

[148] Physics Department, Royal Institute of Technology, Stockholm, Sweden

[149] Departments of Physics & Astronomy and Chemistry, Stony Brook University, Stony Brook NY, United States of America

[150] Department of Physics and Astronomy, University of Sussex, Brighton, United Kingdom

[151] School of Physics, University of Sydney, Sydney, Australia

[152] Institute of Physics, Academia Sinica, Taipei, Taiwan

[153] Department of Physics, Technion: Israel Institute of Technology, Haifa, Israel

[154] Raymond and Beverly Sackler School of Physics and Astronomy, Tel Aviv University, Tel Aviv, Israel

[155] Department of Physics, Aristotle University of Thessaloniki, Thessaloniki, Greece

[156] International Center for Elementary Particle Physics and Department of Physics, The University of Tokyo, Tokyo, Japan

[157] Graduate School of Science and Technology, Tokyo Metropolitan University, Tokyo, Japan

[158] Department of Physics, Tokyo Institute of Technology, Tokyo, Japan

[159] Department of Physics, University of Toronto, Toronto ON, Canada

[160] [a] TRIUMF, Vancouver BC; [b] Department of Physics and Astronomy, York University, Toronto ON, Canada

[161] Faculty of Pure and Applied Sciences, University of Tsukuba, Tsukuba, Japan

[162] Department of Physics and Astronomy, Tufts University, Medford MA, United States of America

[163] Centro de Investigaciones, Universidad Antonio Narino, Bogota, Colombia

[164] Department of Physics and Astronomy, University of California Irvine, Irvine CA, United States of America

[165] [a] INFN Gruppo Collegato di Udine, Sezione di Trieste, Udine; [b] ICTP, Trieste; [c] Dipartimento di Chimica, Fisica e Ambiente, Università di Udine, Udine, Italy

[166] Department of Physics, University of Illinois, Urbana IL, United States of America

[167] Department of Physics and Astronomy, University of Uppsala, Uppsala, Sweden

[168] Instituto de Física Corpuscular (IFIC) and Departamento de Física Atómica, Molecular y Nuclear and Departamento de

Ingeniería Electrónica and Instituto de Microelectrónica de Barcelona (IMB-CNM), University of Valencia and CSIC, Valencia, Spain

[169] Department of Physics, University of British Columbia, Vancouver BC, Canada

[170] Department of Physics and Astronomy, University of Victoria, Victoria BC, Canada

[171] Department of Physics, University of Warwick, Coventry, United Kingdom

[172] Waseda University, Tokyo, Japan

[173] Department of Particle Physics, The Weizmann Institute of Science, Rehovot, Israel

[174] Department of Physics, University of Wisconsin, Madison WI, United States of America

[175] Fakultät für Physik und Astronomie, Julius-Maximilians-Universität, Würzburg, Germany

[176] Fachbereich C Physik, Bergische Universität Wuppertal, Wuppertal, Germany

[177] Department of Physics, Yale University, New Haven CT, United States of America

[178] Yerevan Physics Institute, Yerevan, Armenia

[179] Centre de Calcul de l'Institut National de Physique Nucléaire et de Physique des Particules (IN2P3), Villeurbanne, France

[a] Also at Department of Physics, King's College London, London, United Kingdom

[b] Also at Institute of Physics, Azerbaijan Academy of Sciences, Baku, Azerbaijan

[c] Also at Particle Physics Department, Rutherford Appleton Laboratory, Didcot, United Kingdom

[d] Also at TRIUMF, Vancouver BC, Canada

[e] Also at Department of Physics, California State University, Fresno CA, United States of America

[f] Also at Tomsk State University, Tomsk, Russia

[g] Also at CPPM, Aix-Marseille Université and CNRS/IN2P3, Marseille, France

[h] Also at Università di Napoli Parthenope, Napoli, Italy

[i] Also at Institute of Particle Physics (IPP), Canada

[j] Also at Department of Physics, St. Petersburg State Polytechnical University, St. Petersburg, Russia

[k] Also at Chinese University of Hong Kong, China

[l] Also at Department of Financial and Management Engineering, University of the Aegean, Chios, Greece

[m] Also at Louisiana Tech University, Ruston LA, United States of America

[n] Also at Institucio Catalana de Recerca i Estudis Avancats, ICREA, Barcelona, Spain

[o] Also at Institute of Theoretical Physics, Ilia State University, Tbilisi, Georgia

[p] Also at CERN, Geneva, Switzerland

[q] Also at Ochadai Academic Production, Ochanomizu University, Tokyo, Japan

[r] Also at Manhattan College, New York NY, United States of America

[s] Also at Novosibirsk State University, Novosibirsk, Russia

[t] Also at Institute of Physics, Academia Sinica, Taipei, Taiwan

[u] Also at LAL, Université Paris-Sud and CNRS/IN2P3, Orsay, France

[v] Also at Academia Sinica Grid Computing, Institute of Physics, Academia Sinica, Taipei, Taiwan

[w] Also at Laboratoire de Physique Nucléaire et de Hautes Energies, UPMC and Université Paris-Diderot and CNRS/IN2P3, Paris, France

[x] Also at School of Physical Sciences, National Institute of Science Education and Research, Bhubaneswar, India

[y] Also at Dipartimento di Fisica, Sapienza Università di Roma, Roma, Italy

[z] Also at Moscow Institute of Physics and Technology State University, Dolgoprudny, Russia

[aa] Also at Section de Physique, Université de Genève, Geneva, Switzerland

[ab] Also at Department of Physics, The University of Texas at Austin, Austin TX, United States of America

[ac] Also at International School for Advanced Studies (SISSA), Trieste, Italy

[ad] Also at Department of Physics and Astronomy, University of South Carolina, Columbia SC, United States of America

[ae] Also at School of Physics and Engineering, Sun Yat-sen University, Guangzhou, China

[af] Also at Faculty of Physics, M.V.Lomonosov Moscow State University, Moscow, Russia

[ag] Also at Moscow Engineering and Physics Institute (MEPhI), Moscow, Russia

[ah] Also at Institute for Particle and Nuclear Physics, Wigner Research Centre for Physics, Budapest, Hungary

[ai] Also at Department of Physics, Oxford University, Oxford, United Kingdom

[aj] Also at Department of Physics, Nanjing University, Jiangsu, China

[ak] Also at Institut für Experimentalphysik, Universität Hamburg, Hamburg, Germany

[al] Also at Department of Physics, The University of Michigan, Ann Arbor MI, United States of America

[am] Also at Discipline of Physics, University of KwaZulu-Natal, Durban, South Africa

[an] Also at University of Malaya, Department of Physics, Kuala Lumpur, Malaysia

[*] Deceased